THE DEVELOPMENT OF CONSTITUTIVE EQUATIONS OF POLYCARBONATE AND MODELING THE IMPACT BEHAVIOR

A Thesis Submitted to
The Graduate School of Engineering and Sciences of
İzmir Institute of Technology
in Partial Fulfilment of the Requirements for the Degree of

DOCTOR OF PHILOSOPHY

in Mechanical Engineering

by
Mustafa Kemal SARIKAYA

July 2023
IZMIR

We approve the thesis of **Mustafa Kemal SARIKAYA**

Examining Committee Members:

_____

Prof. Dr. Mustafa GÜDEN
Department of Mechanical Engineering, İzmir Institute of Technology

_____

Prof. Dr. Yeliz PEKBEY
Department of Mechanical Engineering, Ege University

_____

Assoc. Prof. Dr. Sinan KANDEMİR
Department of Mechanical Engineering, İzmir Institute of Technology

_____

Prof. Dr. Mehmet ORHAN
Department of Mechanical Engineering, Pamukkale University

_____

Assoc. Prof. Dr. İzzet ÖZDEMİR
Department of Civil Engineering, İzmir Institute of Technology

6 July 2023

_____

Prof. Dr. Mustafa GÜDEN
Supervisor, Department of
Mechanical Engineering
İzmir Institute of Technology

_____

Prof. Dr. Alper TAŞDEMİRCİ
Co-Supervisor, Department of
Mechanical Engineering
İzmir Institute of Technology

_____

Prof. Dr. M. İ. Can DEDE
Head of the Department of
Mechanical Engineering

_____

Prof. Dr. Mehtap EANES
Dean of the Graduate School of
Engineering and Sciences

ACKNOWLEDGEMENTS

I would like to thank to my supervisor Prof. Dr. Mustafa GÜDEN for accepting me to his research team, instructive comments, trust, encouragement and support during the entire thesis study. Secondly, thank to my co-supervisor Prof. Dr. Alper TAŞDEMİRCİ for his supports.

I would like to thank The Scientific and Technological Research Council of Turkey (TUBITAK) and 2244- Industrial PhD Fellowship Program for financial support of the study and the project manager, Dr. Sinan YILMAZ.

I would like to thank Çağdaş KAMBUR and the Turkish Aerospace Industry for for their guidance.

Thanks to all members of Dynamic Testing and Modelling Laboratory; Samed ENSER, Murat YILDIZTEKİN, Hacer İrem ERTEN KAPLAN, Gülden ÇİMEN, Mesut BAYHAN, Burak AĞIRDICI, Çetin BAKICI, Seven Burçin ÇELLEK, Mehmet Yalçın SIRMALILAR, Arslan BIN RIAZ and Mian IMRAN for their endless supports and associations.

Last but not least, I would like to express my deepest and sincere gratitude to my family, my father Tayyip SARIKAYA, my mother Ayten SARIKAYA, my older brother Dr. Şakir SARIKAYA, my aunt Prof. Dr. Fatma Süreyya CEYLAN and my uncle Kubilay SARIKAYA and our neighbours Abdurrahman ÇAMLI (deceased) and Gülten ÇAMLI.

ABSTRACT

THE DEVELOPMENT OF CONSTITUTIVE EQUATIONS OF POLYCARBONATE AND MODELING THE IMPACT BEHAVIOR

The Johnson and Cook (JC) flow stress and damage parameters of a polycarbonate were determined by the mechanical tests and numerical simulations. The experimental tests included quasi-static and high strain rate tension and compression, quasi-static notched-specimen tension, quasi-static indentation (QSI), low velocity impact (LVI) and projectile impact (PI). The flow stress equation determined from the experimental average true stress-true strain curve well agreed with the effective stress-strain obtained from the quasi-static numerical tension test. The numerical QSI force-displacement curve based on the experimental average true stress-true strain equation was further shown to be very similar to that of the experiment. The LVI and PI test simulations were then continued with the experimental average true stress-true strain equation using five different flow stress-strain rate relations: JC, Huh and Kang, Allen-Rule and Jones, Cowper-Symonds and the nonlinear rate approach. No strain rate sensitivity in the LVI tests was ascribed to low strain rate dependency of the flow stress at intermediate strain rates and large strains. On the other side, all the stress-strain rate relations investigated nearly predicted the experimental damage types in the PI tests, except the Cowper-Symonds relation which predicted the fracture of the polycarbonate plate at 140 m s^{-1}. The absorbed energy at 160 m s^{-1} test was determined 1.6 times that of the QSI test, proving an increased energy absorption of the tested polycarbonate at the investigated impact velocities. The verified parameters were finally used to model the damages formed on a canopy against bird strike.

ÖZET

POLİKARBONATIN YAPISAL DENKLEMLERİNİN GELİŞTİRİLMESİ VE DARBE DAVRANIŞININ MODELLENMESİ

Polikarbonatın Johnson ve Cook (JC) akış gerilimi ve hasar parametreleri, mekanik testler ve nümerik simülasyonlarla belirlendi. Deneysel testler, yarı statik ve yüksek deformasyon hızında çekme ve basma, yarı statik çentikli numuneli çekme, yarı statik girinti (YSG), düşük hızda darbe (DHD) ve projektil darbesini (PD) içermiştir. Deneysel ortalama gerçek gerilim-gerçek gerinim eğrisinden belirlenen akış gerilim denklemi, yarı statik nümerik çekme testinden elde edilen etkin gerilim-gerinim ile iyi bir uyum içindedir. Deneysel ortalama gerçek gerilim-gerçek gerinim denklemine dayanan nümerik YSG kuvvet-yer değiştirme eğrisinin, deneyinkine çok benzer olduğu da gösterildi. DHD ve PD testi simülasyonları daha sonra beş farklı akış gerilimi-gerinim oranı ilişkisi kullanılarak deneysel ortalama gerçek gerilim-gerçek gerinim denklemi ile devam ettirildi: JC, Huh ve Kang, Allen-Rule ve Jones, Cowper-Symonds ve nonlineer deformasyon hızı yaklaşımı. DHD testlerinde neredeyse hiç deformasyon hızı hassasiyeti saptanmaması, orta deformasyon hızlarındaki büyük deformasyon içeren akış geriliminin düşük deformasyon hızı bağlılığına atfedilmiştir. Öte yandan, araştırılan tüm gerilme-deformasyon hızı ilişkileri deneysel hasar tiplerini, plakanın 140 m s^{-1}'de kırılmasını öngören Cowper-Symonds ilişkisi dışında, neredeyse tahmin ediyordu. 160 m s^{-1} testinde emilen enerji, YSG testinin 1.6 katı olarak belirlendi ve bu, test edilen polikarbonatın araştırılan darbe hızlarında artan bir enerji emilimi olduğunu kanıtladı. Doğrulanan parametreler, oluşan hasarları ve bir kanopi yapısının kuş çarpmasına karşı sınırlarını modellemek için kullanılmıştır.

TABLE OF CONTENTS

LIST OF FIGURES

Figure **Page**

Figure **Page**

Figure **Page**

Figure **Page**

Figure **Page**

Figure **Page**

LIST OF TABLES

Table **Page**

LIST OF ABBREVIATIONS

ARJ	**:**	Allen-Rule and Jones
BPA	**:**	Bisphenol A
CS	**:**	Cowper-Symonds
DIC	**:**	Digital Image Correlation
DOP	**:**	Depth of penetration
DSGZ	**:**	Duan-Saigal-Greif-Zimmermann
EASA	**:**	European Aviation Safety Agency
EOS	**:**	Equation of state
FAA	**:**	Federal Aviation Administaration
FE	**:**	Finite element
FOD	**:**	Foreign object damage
h/d	**:**	Thickness-to-projectile diameter ratio
HK	**:**	Huh and Kang
HSR	**:**	High strain rate
JC	**:**	Johnson-Cook
L/D	**:**	Length to diameter ratio
LVI	**:**	Low velocity impact
NLA	**:**	Nonlinear rate approach
PC	**:**	Polycarbonate
PI	**:**	Projectile impact
PMMA	**:**	Polymethylmethacrylate
POP	**:**	Penetration path
PVB	**:**	Polyvinylbutyral
QSI	**:**	Quasi-static indentation
SHPB	**:**	Split Hopkinson pressure bar
SHTB	**:**	Split Hopkinson tension bar
SPH	**:**	Smoothed Particle Hydrodynamics
UMAT	**:**	User-defined material subroutine
ZWT	**:**	ZHU-WANG-TANG

CHAPTER 1

INTRODUCTION

Polycarbonate (PC) is one of the most common thermoplastic polymers. Its products are manufactured either by extrusion, e. g. long pipes and sheets or injection molding, e.g. complex geometries. Polycarbonate is also named by its trademarks. The PC material manufactured using the Bayer's and the General Electric's granules are called Makrolon and Lexan, respectively. Later, Lexan bought Makrolon. The PC products are used in electronics such as cell phone and LCD sections, in automotive such as headlamp lenses and windows of automobiles, in protection such as helmet visors and riot shields and in aeronautical and aerospace such as the visor of the astronaut helmet, windshields, and canopies.

The PC components used in the windshields and canopies of aircrafts have the potentials of being exposed to the foreign object damage (FOD). The FOD may be due to the impacts from wildlife, hail, and ice, from the aircraft engine fasteners such as nuts, bolts, and washers, and from the aircraft parts such as fuel cap and tire fragments. Among them, the wildlife strikes are the most common, especially bird strikes. Bird strikes can easily form cracks or causes perforation type damages on the windshields and canopies. The Federal Aviation Administration[1] has reported more than 156,114 wildlife strikes (151,267 birds, 3,360 terrestrial mammals, 1,264 bats and 223 reptiles) to civil aircrafts between 1990 and 2014. The aircraft component that is the most exposed to bird strikes is the windshield, with 16%. The European Aviation Safety Agency[2] has declared the percentage of bird strikes to windshields 13% between 1999 and 2008 all over the world.

Both the Federal Aviation Administration and the European Aviation Safety Agency have listed the orders for the aircraft certification to ensure that all the aircraft components can withstand bird strikes at the critical flight speeds. Based on these authorities, the bird strike tests on the aircraft components should be performed using a 1.8 kg-bird. The bird velocity in these bird strike tests should be equal to the cruise velocity of the aircraft at the sea level or 85% of the cruise velocity at 2,438 m height. In many cases, the bird strike tests are accompanied by the explicit nonlinear finite element (FE) models. Because, the FE models can significantly reduce the excessive cost of these

tests. The explicit FE models predict the nonlinear behavior of materials/structures at high strain rates and large deformations such as the projectile and foreign object impact. LS-Dyna is an example to such explicit nonlinear codes and offers both the Lagrangian and meshless Smoothed Particle Hydrodynamics (SPH) approach.

The aim of this thesis is to develop the Johnson-Cook (JC) flow stress equation and to determine the JC damage model parameters of a Lexan PC in order to predict its impact behavior against bird strike. As will be elaborated later, it has been noted there have been few and no systematic studies on the damage model parameters of PC in the current literature. The damage in the previous modelling studies was commonly defined by a constant erosion strain in the dynamic simulations. However, the failure strain varies with strain rate and stress triaxiality. Throughout the experimental and numerical studies of the thesis, the numerical iterations were performed between the experimental and model results in order to fine tune up both the flow stress equation and damage model parameters of PC. It is believed that this study will contribute to the current literature in that it provides more precise and fine-tuned flow stress equations and damage model parameters that can be applicable for extreme loading conditions such as large strain deformations at high strain rates (HSR).

In the thesis, six different types of experimental tests were performed, and the experimental tests results were compared with the model results. The quasi-static tension and compression tests were performed at the strain rates of 10^{-3}, 10^{-2}, 10^{-1} and 1 s^{-1}. The high strain rate compression Split Hopkinson Pressure Bar (SHPB) tests were performed between 450 and 4500 s^{-1}. The high strain rate tension Split Hopkinson Tension Bar (SHTB) tests were performed at the strain rate of 1200 s^{-1}. The quasi-static indentation (QSI) tests were performed at the velocity of 6 mm s^{-1} and the low velocity impact (LVI) tests were performed at the velocity of 4.75 m s^{-1}. Finally, the projectile impact (PI) tests were performed at the velocities of 100, 140 and 160 m s^{-1}. The bird strike simulations were implemented at the velocities of 116, 140, and 230 m s^{-1}. The test results were verified by the simulations in the explicit FE code of LS-Dyna.

In the thesis, the deformation behavior of PC is given in Chapter 2. Chapter 3 provides the details of test procedures and set-ups. Chapter 4 explains the implemented numerical test models. The results and discussions of the tests and the numerical models are given in Chapter 5. Finally, the conclusions are made in Chapter 6.

CHAPTER 2

DEFORMATION BEHAVIOR OF POLYCARBONATE

The deformation behavior of PC is given in this chapter with literature survey. Literature survey includes molecular structure and constitutive equations.

2.1. Molecular structure of polycarbonate and transition

Polycarbonate is a glassy thermoplastic polymer in which the molecular chains are randomly oriented. It is made of two groups of molecules: Bisphenol A (BPA) and carbonate (Figure 2.1(a)). The BPA group is made of two phenyls (6-carbon grey dots and 5-hydrogen blue dots) and one methyl (3-carbon and 6-hydrogen). The carbonate group consists of 1-carbon (grey dot) and 3-oxygen (3 red dots). The molecular chains of these groups align in a zig-zag form in the molecular structure (Figure 2.1(a)). These molecular chains interact with one another through weak van der Waals forces. These forces determine the mechanical behavior of PC that strongly depends on both temperature and strain rate.

The transitions corresponding to the restrictions of the molecular chain translations and rotations as function of temperature are usually denoted by the Greek alphabetical letters, α, β, γ and etc. The α-transition is associated with the restricted rotations and translations of the main chains, phenyls and carbonate groups. The α-transition, also known as the glass transition, covers the temperatures from -95^{o}C to ~150^{o}C and is centered at around 150^{o}C [3] (Figure 2.1(b)). All other transitions are considered as the secondary transitions. When the temperature drops to -95^{o}C, the molecular mobility of main-chain phenyl groups is restricted which is associated with the β-transition[3] (Figure 2.1(b). These transitions affect the elastic modulus (Figure 2.1(c)) and yield strength of PC. For example, the modulus of PC is about 3 GPa at 150 K (-123^{o}C) and the modulus decreases to about 2 GPa at 225 K (-48 ^{o}C) and to about 1.7 GPa at 273 K (0^{o}C) as seen in Figure 2.1(c)). The modulus drops to 1.3 GPa at about the glass transition temperature (150^{o}C). Increasing strain rate has an opposite effect of increasing temperature. The increase of strain rate increases both the β-transition temperature (-

95°C) and the α-transition temperature (150°C); hence the elastic modulus and yield strength increase with increasing strain rate (Figure 2.1(d)). Note that a lesser amount of thermal energy is provided at increasing strain rates since less time is available for material deformation, making the deformation more difficult. In the literature, the tension, compression and the projectile impact tests have been commonly used to determine the mechanical behavior of PC at different loading conditions.

2.2. Tensile and compression behavior

Buisson and Ravi Chandar[4] studied the quasi-static uniaxial tensile behavior of a PC plate test specimen. The load-deflection curve and the deformation pictures of a tensile tested specimen is shown in Figure 2.2. As is seen, the deformation is linear up to a yield point at low displacements and the yield point corresponds to the peak load. Thereafter, a nonlinear behavior starts. As similar with metals, Lüder's bands initiate at the yield force, which is followed by a strain softening behavior. Different from metals, the shear band instability in PC does not however cause failure of the test specimen, instead the shear band instability turns into a stabilized necking. This leads to a large ductility and toughness. The necking is maintained and proceeds along the specimen length until about a locking strain.

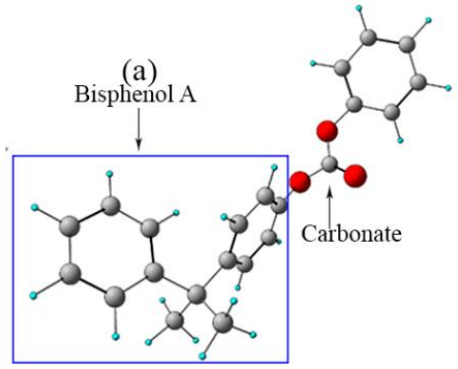

(cont. on next page)

Figure 2.1. (a) Molecular chain orientation[5], PC (b) storage modulus and loss modulus and (c) decomposed elastic modulus curves as a function of temperature at 3.2×10^{-3} s^{-1} (1 Hz)[3] and (d) model prediction of the PC elastic modulus curve at different strain rates[3]

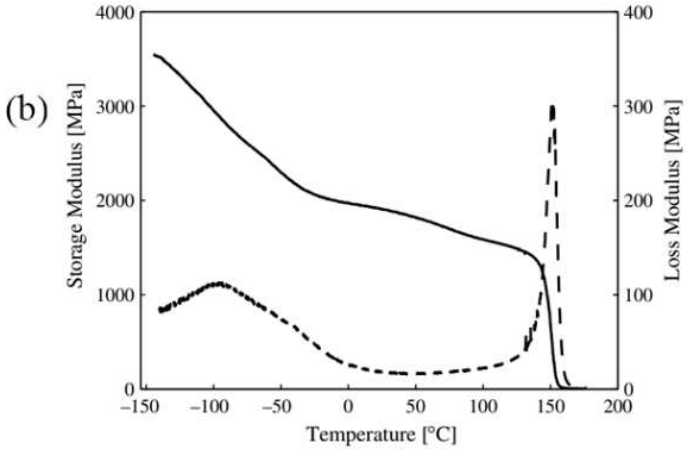

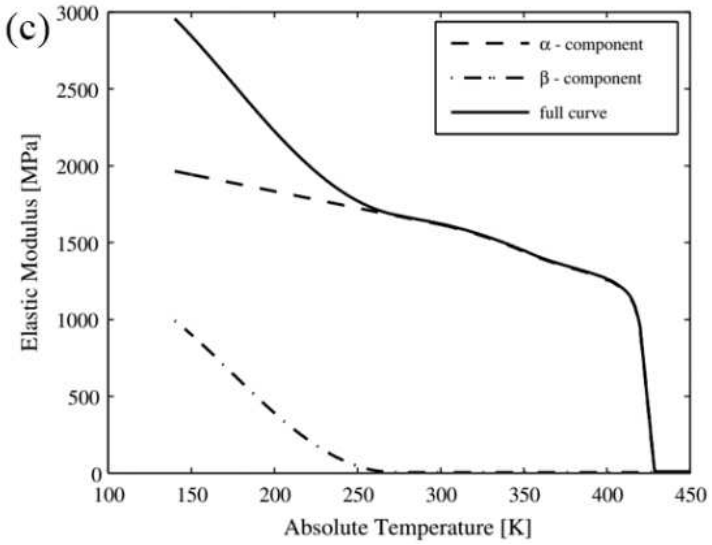

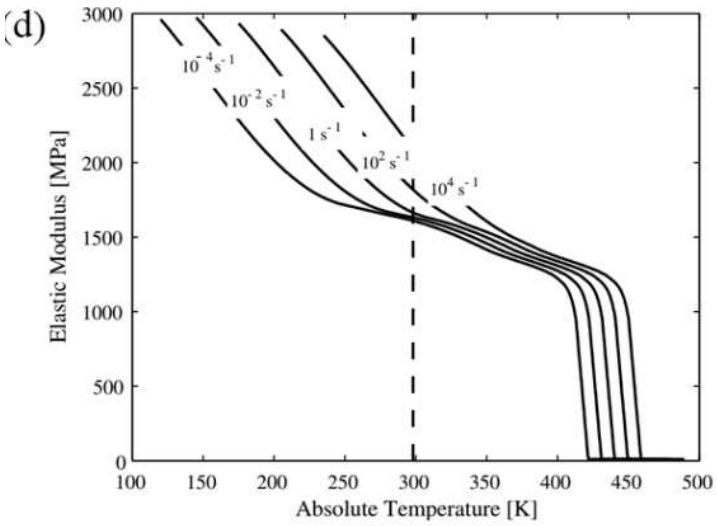

Figure 2.1. (cont.)

The shear band instability at the peak load in square and rectangular cross-section specimens occurs due to a reduction in the triaxiality. The shear band instability in round specimens, on the other hand, begins with either an axisymmetric profile or Lüder's band formation. Nevertheless, the necking propagates at an almost constant load for both the square and round cross-section specimens. Above explained deformation mode of PC under uniaxial quasi-static tensile loads is called cold drawing [4, 6-8]. As stated, the test specimen necks down locally with a sudden reduction in its diameter (round specimen) after an initial peak load. During the progression of the necking, the molecular chains in the necked region are aligned along the tensile loading axis. After the complete progression of shear bands in the specimen, the extension of the aligned molecular chains increases the load values, which is known as a locking. Since the state of stress in the necked region is three dimensional, the conversation of the engineering stress-strain curve after necking into a true stress-true strain curve using the conventional equations based on the homogenous deformation along the length of the specimen cannot give the actual deformation stress[9].

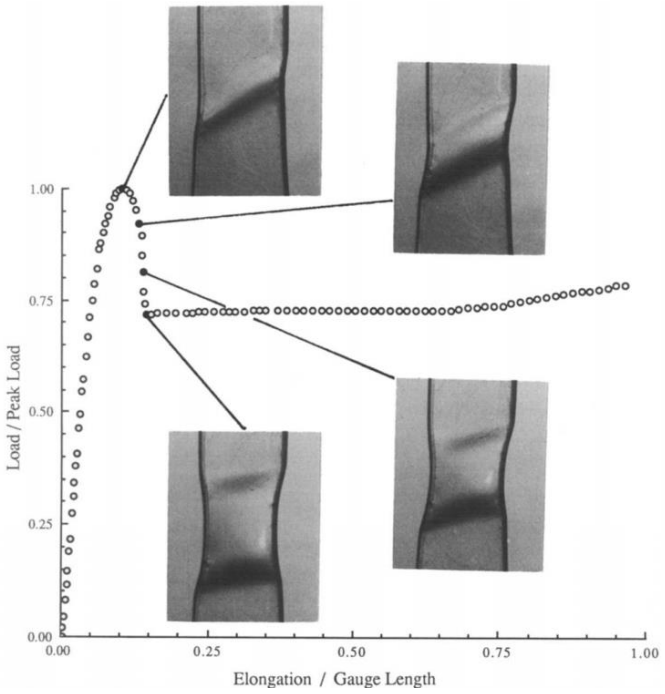

Figure 2.2. Load-elongation curve of a rectangular cross-section PC specimen under tensile loads[4]

Boyce and Arruda[8] compared the true stress-strain curves of a PC specimen under tension and compression (Figure 2.3). As with the tensile test, the quasi-static compression of PC exhibits a nonlinear viscoelasticity, yielding, strain softening and strain hardening. The maximum point in the true stress-true strain curve after the elastic region is defined as the yield or upper yield point (Figure 2.3). Following the upper yield point, plastic strain produces local structural changes which decreases the intermolecular barriers of chain segment rotation. Eventually, the stress needed for further deformation decreases and strain softening occurs. Afterwards, all the chain segments align in a plane normal to the compression axis. This then causes a strain hardening. The locking occurs due to planar orientation process in the strain hardened region. The compression however results in a lower yield strength and strain hardening rate than the tension (Figure 2.3). The locking occurs at about 70 percent tensile strain and 125 percent compressive strain. The higher strain hardening of tension than compression is due to the formation of higher local strain rates during necking and alignment of molecular chains in tension test (Figure 2.3). On the other side, lower strain hardening leads to a higher ductility in compression.

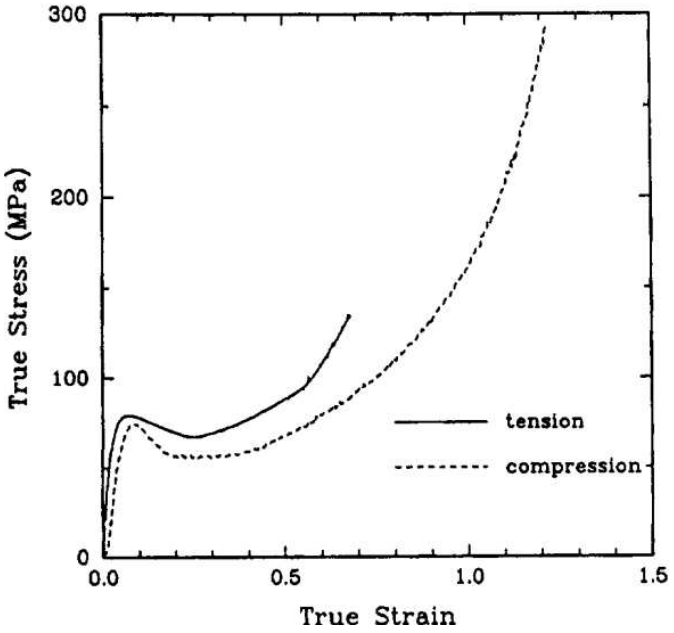

Figure 2.3. True stress-true strain curve of a PC specimen under tension and compression[8]

2.3. High strain rate and elevated temperature tests

The results of the experimental studies on the effect of strain rate and temperature were usually fitted with the available constitutive equations for polymers. The detailed formulations of the constitutive equations developed for PC will be given in the next section and brief information on these questions are given in this section when needed.

One of the earliest theory on the yielding of polymers is the Eyring's[10] theory. It is a transition state theory that explains how a molecule transits from one state to another by overcoming an activation energy. Once the activation energy which is driven by the shear stress, is exceeded, the shear stress induces yielding. Eyring[10] argued that the yielding is a single thermally activated process. Later, Ree-Eyring[11] extended the Eyring's[10] theory using two activated processes, temperature and strain rate. Bauwens-Crowet et al.[12] tailored the Eyring's[10] theory to fit to the tensile yield strength of a PC from ~10^{-5} to ~1 s^{-1} and from 20 to 140°C. The results of this fitting are shown in Figure 2.4 as the variation of the yield strength with the strain rate at different temperatures. A significant effect of temperature and strain rate on the yield strength is seen in the same figure between ~10^{-5} and ~1 s^{-1}. G'sell and Gopez[13] shear tested a PC specimen between -100 and 150°C and $3x10^{-5}$ and $3x10^{-2}$ s^{-1}. As with the tension tests performed by Bauwens-Crowet et al.[12], the shear stress increased as the strain rate increased and decreased as the temperature increased as seen in Figure 2.5.

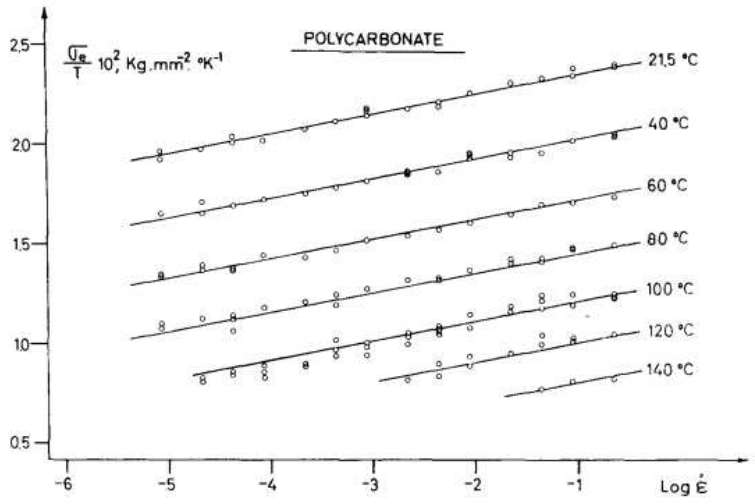

Figure 2.4. Measured ratio of the yield stress to temperature as a function of logarithm of strain rate[12]

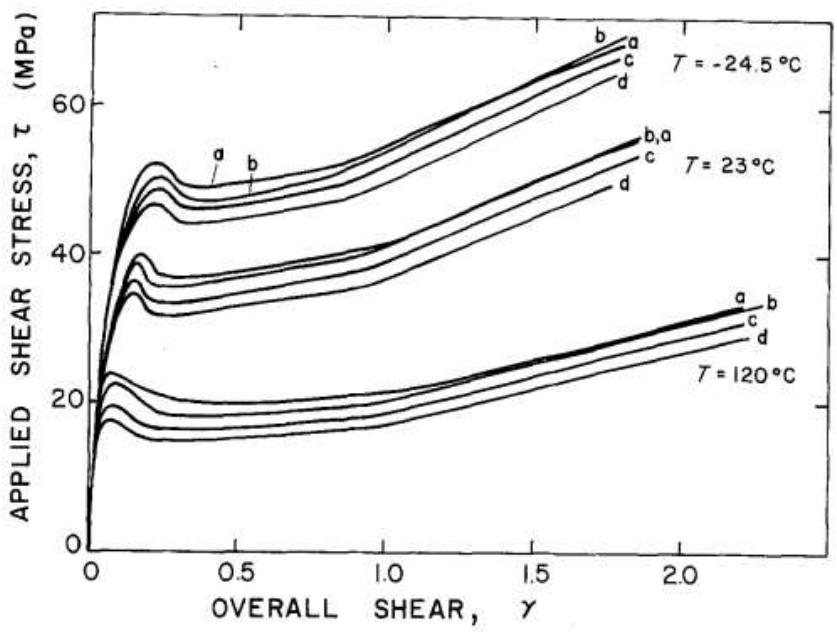

Figure 2.5. Influence of strain rate on the stress-strain behavior of the PC in simple shear at the various strain rates: $3x10^{-2}$ (a), $3x10^{-3}$ (b), $3x10^{-4}$ (c) and $3x10^{-5}$ s^{-1}(d)[13]

Bauwens et al.[14] studied the effect temperature and strain rate on the yield strength of a PC between ~10^{-8} and ~10^{2} s^{-1} and 22.8 and 80ºC. At these low strain rates, the yield strength increased with increasing strain rate. A linear dependence of yield stress on the logarithm of strain rate as described by an Eyring-type equation[14] was shown (Figure 2.6).

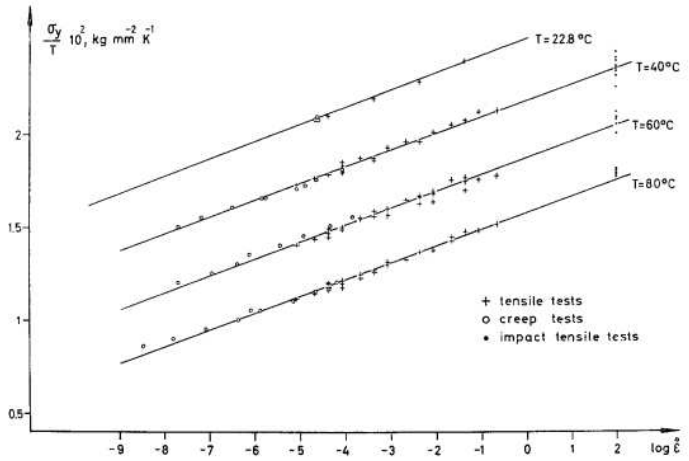

Figure 2.6. The plot of the ratio of the engineering yield stress to temperature, against the logarithm of the strain-rate at yield[14]

Boyce et al.[7] compared the deformation behavior of a PC with the Arruda and Boyce[15] constitutive model using the stress-strain curves. The Arruda and Boyce[15] constitutive model accurately predicted the large strain behavior of these various states of deformation. Bjerke et al.[16] performed the SHPB experiments and opening mode dynamic fracture experiments (three point bending test) to measure the thermomechanical response of a PC at 400-3000 s^{-1}. F. Rietsch and B. Bouette[17] determined the strain rate dependent compressive yield strength between 10^{-4} and 4500 s^{-1} and between -40 and 60ºC. Within the temperature range studied (below the glass transition temperature), two different strain rate sensitivities were found: a lower strain rate sensitivity at low strain rates and a higher strain rate sensitivity above a critical strain rate. In both regions, the compressive yield strength showed nearly a linear dependence on the logarithm of the strain rate, except at the transition region (Figure 2.7).

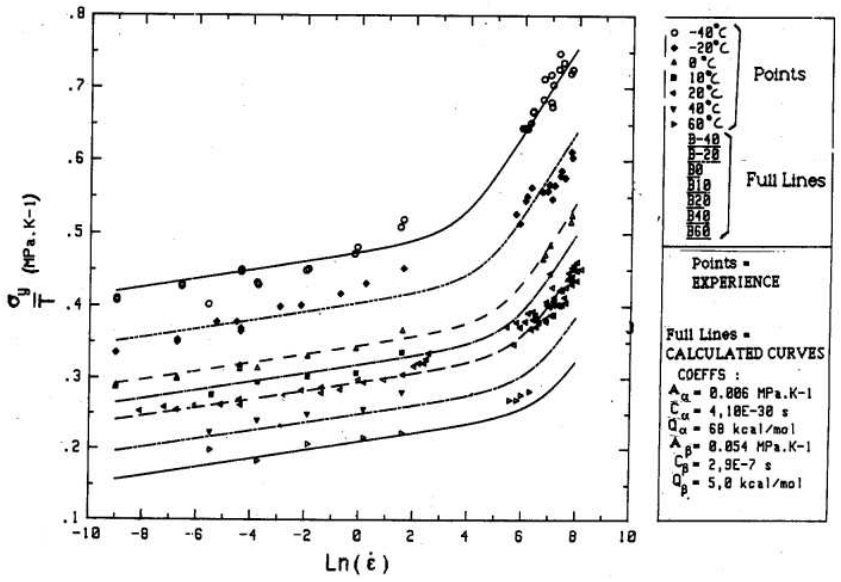

Figure 2.7. Measured ratio of yield stress to temperature as a function of logarithm of strain rate[17]

Siviour et al.[18] investigated the compressive stress–strain behavior of a PC at the strain rates between 10^{-4} and 10^{4} s^{-1} and at the temperatures between -50 and 150ºC. The observed glass transition temperature at 5500 s^{-1} was shown to be consistent with that was extrapolated from the dynamic mechanical analysis data, and the upper temperature of the β-transition region at this strain rate was calculated approximately 40ºC (the β-transition temperature increased with increasing strain rate). This temperature was also

consistent with that at which the dependence of yield strain on temperature and strain rate changed. Therefore, it was concluded that the increase of the strength of PC at HSRs was due to the β-transition temperature being above the room temperature at these strain rates. The strain rate sensitivity is mainly determined by the α-transition at low strain rates; however, it is determined by both the α-transition and β-transition at high strain rates. Dar et al.[19] performed SHPB compression tests from 10^{-3} to 10^{3} s^{-1} and from 213 to 393 K. Furthermore, the Duan-Saigal-Greif-Zimmerman (DSGZ) constitutive model was used in the same study to capture the mechanical behavior at various temperatures and strain rates. Dar et al.[20] implemented the constitutive model by generating a user-defined material subroutine (UMAT) in explicit finite element solver LS-Dyna. The model successfully captured the high velocity projectile impact behavior of polymethylmethacrylate (PMMA) aircraft windshield and PC astronaut helmet visor. Hu et al.[21] experimentally determined the dynamic responses of a PC. A pulse-shaping technique was applied to control the incident pulse in the SHPB experiments to provide dynamic stress equilibrium and homogeneous deformation in the specimens. Zhang et al.[22] studied the dynamic compressive and tensile mechanical properties using a SHPB and 2D Digital Image Correlation (DIC) method. The experimental data showed nonlinear elastic characteristics. These experimental data were verified with a 2D-DIC technique. Thereafter, the constitutive behavior of PC was accurately described at different strain rates using the ZHU-WANG-TANG[23] (ZWT) model.

Millett and Bourne[24] determined the equation of state (EOS) parameters of a PC by performing plate impact tests using manganin, polyvinylidene fluoride and electromagnetic particle velocity gages in order to determine the shock and particle velocity. The Hugoniot curve in high pressure was fitted with the least square method. Sarva et al.[25] performed Taylor impact tests to examine the mechanical behavior of a PC, under a HSR (~10^{5} s^{-1}). High-speed photography was used to monitor the deformation. A recently developed three-dimensional large strain rate-dependent elastic–viscoplastic constitutive model was used together with ABAQUS/Explicit FE code to simulate the Taylor impact tests. The simulation results were directly compared with the experimental test images of the initial rod dimensions and velocities. The long rods were deformed by the formation of a mushroom head at the impact end with a subsequent radial barreling and distinctive lip formation. The precise shape depended upon the initial velocity of the rod. The shorter rods exhibited a residual geometry with a mushroom head but no radial barreling. Trautmann et al.[26] investigated the dynamic friction behavior of a PC at ambient

(20°C) and low (-60°C) temperatures using an SHPB. At ambient temperature, polytetrafluoroethylene (PTFE) and molybdenum disulphide (MoS_2) were found to be good lubricants, but not as good as petroleum jelly, which reduced the friction to zero within the experimental error. In low-temperature regime, polytetrafluoroethylene was not a good lubricant. MoS_2 was not a good lubricant as the ice at low temperature. The petroleum jelly provided perfect lubrication within experimental error.

Sarva and Boyce[27] conducted the SHTB tests at 500 and 1500 s^{-1}. The deformation modes ranging from single necking to double necking and to drawing were observed depending on the aspect ratio and the cross-sectional area. Cao et al.[28] investigated uniaxial tension stress–strain behavior of a PC at three temperatures between -60°C and 20°C and four strain rates between 0.001 and 1700 s^{-1}. The yield strength and the strain at yielding increased with increasing strain rate and decreased with increasing temperature. Cao et al.[29] investigated the rate and temperature dependent tension responses of a PC within a wide range of strain rates up to 1700 s^{-1} and temperatures up to 120°C. The yield stress and the strain at yielding presented a dramatic increase at higher strain rates and decreased with the increase of temperature. Xu et al.[30] conducted the HSR tension tests up to 4500 s^{-1}. Tzibula et al.[31] investigated the dynamic tensile response of the PC using SHPB and DIC technique. The tensile yield strength of PC was ~70% higher at the strain rate of ~1000 s^{-1} than that of the quasi-static one.

2.4. Projectile impact and indentation tests

Fleck et al.[32] performed PI tests on a PC using cylindrical projectiles. It was shown in the same study that PC behaved almost similar to metals in the projectile impact tests. At low specimen thicknesses and low impact velocities, PC was deformed by forming a conical hole and a dome-cap formation. At increasing thicknesses, the deformation switched into plugging at high velocities and to denting at low velocities as shown in Figure 2.8. Petalling was also seen, resulting from the used projectile geometry. In another study, normal impact tests were performed using spherical projectiles to understand the deformation modes and fracture of a PC over a wide range of impact velocities[33]. When the PC plate was subjected to ballistic impacts by a spherical projectile, the deformation mode changed from dishing to denting. Finally, deep penetration was observed when petalling as the plate thickness-to-projectile diameter ratio (h/d) increased (Figure 2.9). Petalling was shown to be the ultimate failure mode for all the cases (Figure 2.9).

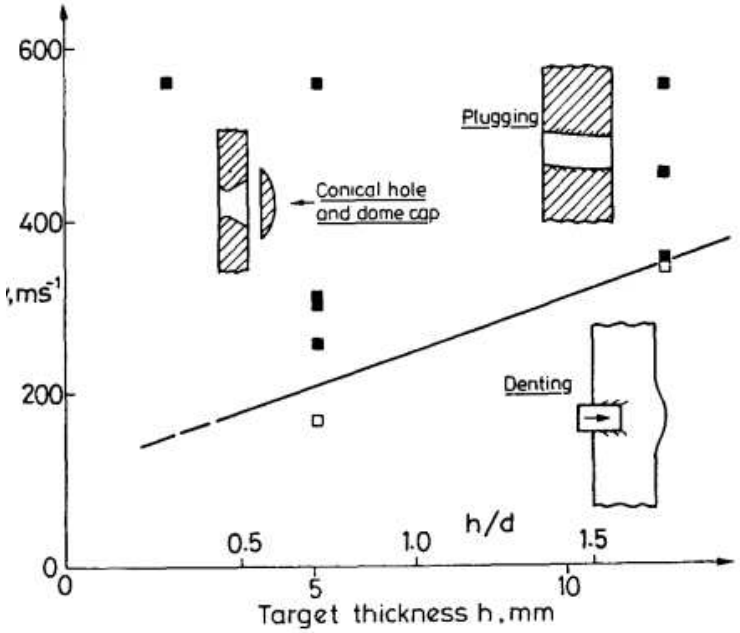

Figure 2.8. The critical velocities for perforation of PC plate subjected to cylindrical projectile[32]

Rosenberg and Kositski[34] performed deep indentation tests using a conical nose indenter to assess the resistance of PC targets against quasi-static indentation and ballistic impacts. Three stages of the deformation on the force-depth curve of PC in the deep indentation tests are shown in Figure 2.10. The beginning stage is the contact stage between the indenter and PC specimen. Thereafter, the force linearly increases at the intermediate stages. The slope of the force-depth curve is noted to be different in the final stage due to the difference in the diameters of the tip and shank. Therefore, the frictional forces were effective in the quasi-static strain rates. After performing ballistic impact tests, eventually, they found that friction forces became less effective at HSRs due to crater wall deformation in the PC targets. Esfahlani[35] modelled the normal (90^o) and inclined angle (30^o) impact of PC and PMMA specimens at the impact velocities between 300 and 720 m s^{-1}. The results were mainly analyzed by the depth of penetration (DOP) and penetration path (POP). The POP exhibited J shape and S shape for normal and inclined impact, respectively (Figure 2.11). Wang et al.[36] performed ballistic impact tests using hemispherical ended bullets to PC plates having thicknesses of 1, 1.5 and 2 mm. The damage modes were crater or dishing and perforation or petalling as shown in Figure 2.12. The critical velocities for perforation were determinied for different thicknesses.

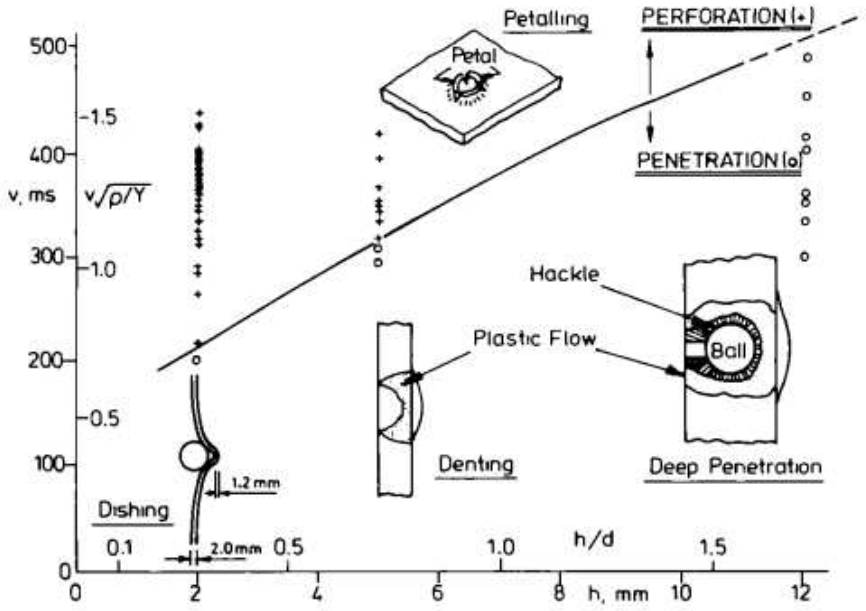

Figure 2.9. Failure mechanisms for ballistic impact of the PC by spherical impactor (hollow points and crosses display penetration and perforation, respectively)[33]

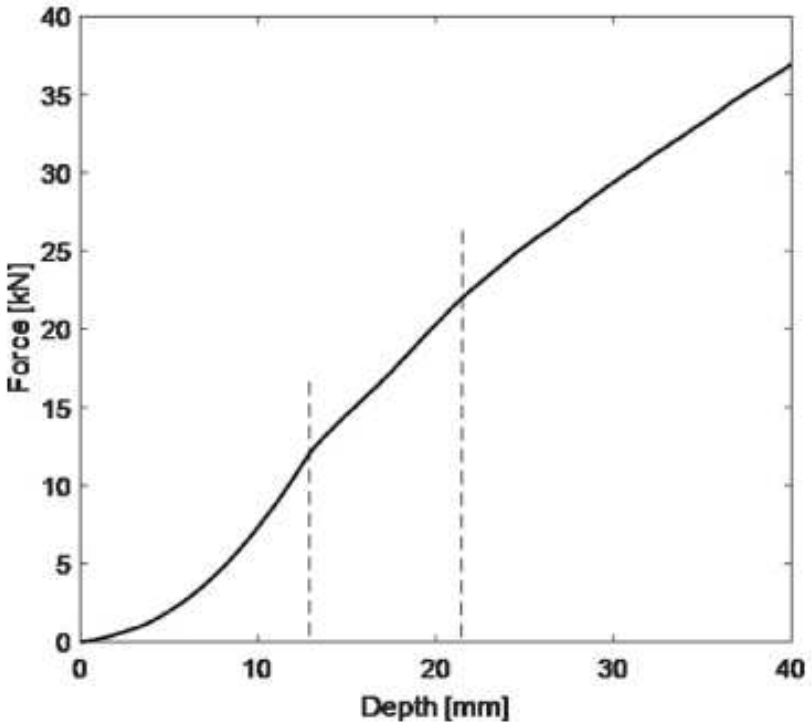

Figure 2.10. The quasi-static indentation curve of PC using conical nose shaped tip[34].

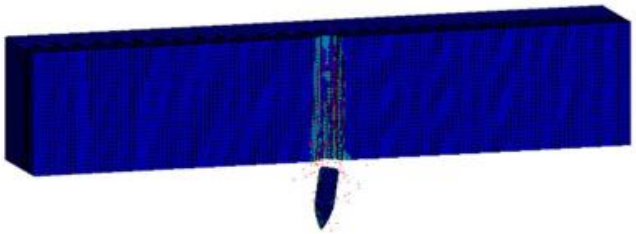

(a)

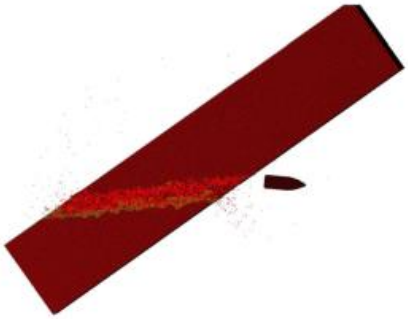

(b)

Figure 2.11. The penetration path types (a) J shape and (b) S shape[35]

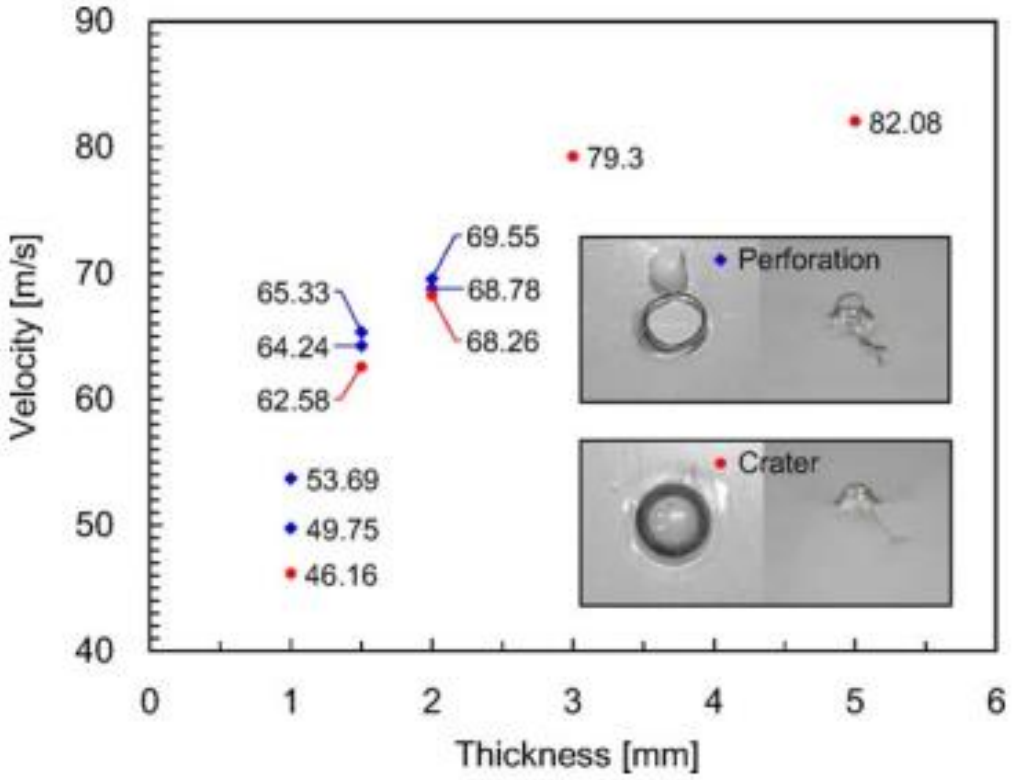

Figure 2.12. Velocity-thickness curve of PC plates exposed to the ballistic tests using hemispherical ended bullets[36]

Husain et al.[37] performed ballistics tests on a PC plate using truncated cone and blunt nosed projectiles. The thickness of the plate was 2.66 mm and the tests were performed between 76 and 106 m s^{-1}. The ballistic limits of the plate for the blunt and truncated projectiles were found to be 81.32 and 70.83 m s^{-1}, respectively.

The deformation modes were shown the same for the impact velocities greater than 100 m s^{-1} while greater bulging was observed in the truncated cone projectile tests for the impact velocity less than 100 m s^{-1} (Figure 2.13).

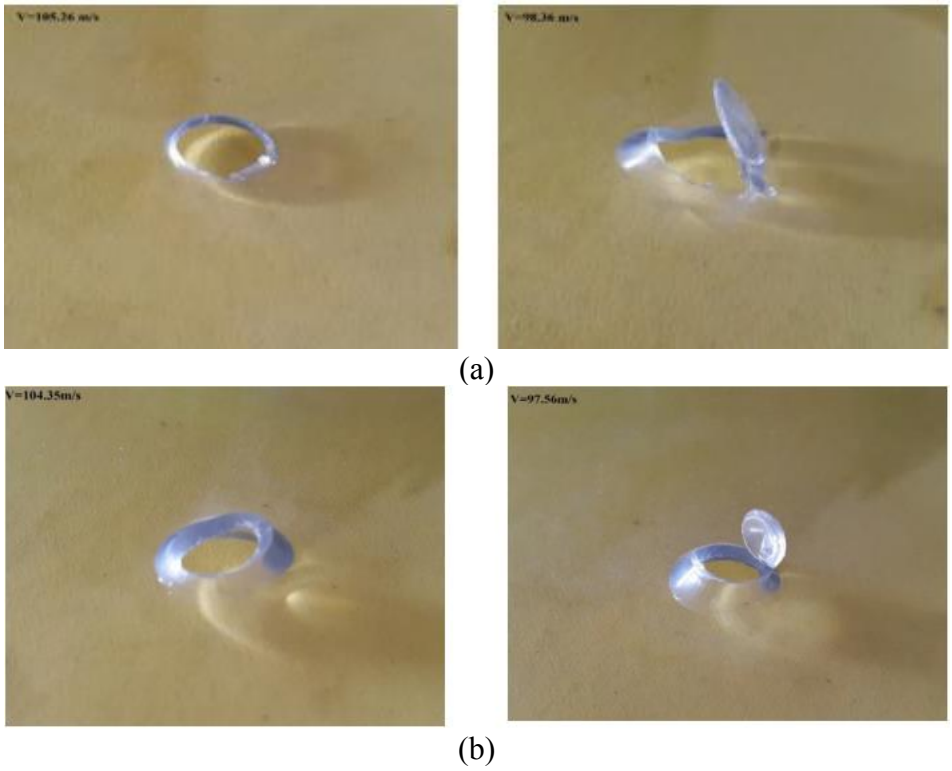

Figure 2.13. The perforation of PC plates using (a) blunt and (b) truncated cone nosed projectiles[37]

2.5. Constitutive equations and models

The constitutive equations are classified as physical and phenomenological. The physical based constitutive equations are formulated using the physical mechanisms while the phenomenological constitutive equations are developed using the experimental data. As the deformation of thermoplastics is complex, the development of a single representative constitutive equation which is valid at quasi-static and high strain rates and low and high temperatures is very difficult.

Eyring[10] developed one of the first models to describe the rate-dependent plastic flow in glassy, amorphous polymers. It is based on a thermally activated yield strength. The theory also explains the viscosity of liquids and gases. It assumes that an amorphous polymer exhibits a viscous flow at the yield. This viscous flow is measured by the strain rate ($\dot{\varepsilon}$). The Eyring's formulation is given in Equation (2.1)

$$\sigma_E = A_\alpha T\left(\ln(2C_\alpha\dot{\varepsilon}) + \frac{Q_\alpha}{RT}\right) \tag{2.1}$$

where σ_E, R, T, and Q_α are the yield stress, universal gas constant, absolute temperature, and activation energy of the α-relaxation, respectively and A_α and C_α are the material constants. Ree-Eyring[11] extended the Eyring's model by including two rate-activated processes in Equation (2.2)

$$\sigma_{RE} = A_\alpha T\left(\ln(2C_\alpha\dot{\varepsilon}) + \frac{Q_\alpha}{RT}\right) + A_\beta T sinh^{-1}\left(C_\beta\dot{\varepsilon}\exp\left(\frac{Q_\beta}{RT}\right)\right) \tag{2.2}$$

where Q_β is the activation energy of the β-relaxation and A_β and C_β, are the material constants.

Robertson's[38] theory explains how a shear stress can cause a flow in an amorphous polymer by altering its structure. The shear stress induces a structural transition from a low energy preferred state (trans) to a higher energy flexed state (cis) (see Figure 2.14). As the shear stress increases, the fraction of the bonds in cis position increases. The increase in the number of cis states induces a decrease in the stiffness. The Robertson's model for shear strain rate ($\dot{\gamma}$) is given in Equation (2.3)

$$\dot{\gamma} = \frac{\tau}{\eta_g}\exp - \left[2.303\left(\frac{c_1^g + c_2^g}{\theta_1 - T_g + c_2^g}\left(\frac{\theta_1}{T}\right) - c_1^g\right)\right] \tag{2.3}$$

where η_g is the viscosity at T_g under the shear stress τ and empirical constants, c_1^g and c_2^g. θ_1 is expressed as the temperature of the motion, at which two other variables, ϑ and ΔE, are associated with a single bond in the chain. ϑ represents the volume associated with the bond, while ΔE represents the energy required to convert the bond from a trans to a cis state.

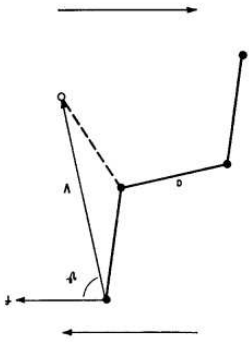

Figure 2.14. Robertson model of a molecular chain under stress, the dashed line indicates the new location of the bond between molecule A and molecule B after a shear force has induced a flexing of the bond from the trans to the cis state[38]

Haward and Trackey[39] divided the deformation of polymers into initial stiffness, viscous flow and rubber elasticity. This constitutive equation generalizes the nonlinear axial stress-axial strain behavior of glassy polymers by incorporating the effects of strain rate, pressure-dependent yielding, strain softening, and temperature. In rheological representation, Hookean spring, Eyring dashpot and Langevin spring were used to refer initial stiffness, viscous flow and rubber elasticity, respectively (Figure 2.15). The expression of Haward and Trackey's model is given in Equation (2.4)

$$\frac{dln(1+\varepsilon_A)}{dt} = K\left[\exp\left(\frac{V(\sigma_m-\sigma_R)(1+\varepsilon_A)}{4kT}\right) - \exp\left(\frac{-V(\sigma_m-\sigma_R)(1+\varepsilon_A)}{4kT}\right)\right] \quad (2.4)$$

where σ_R is the high elastic machine stress and it is shown in Equation (2.5)

$$\sigma_R = \frac{1}{2}NkTn^{\frac{1}{2}}\left[\mathcal{L}^{-1}\left(\frac{1+\varepsilon_A}{n^{\frac{1}{2}}}\right) - (1+\varepsilon_A)^{-\frac{3}{2}}\mathcal{L}^{-1}\left(\frac{1}{(1+\varepsilon_A)^{\frac{1}{2}}n^{\frac{1}{2}}}\right)\right] \quad (2.5)$$

where ε_A and σ_m are the viscous deformation and the machine stress, K and V are the constants from the Eyring's equation and k is the Boltzmann's constant. In Equation 2.5 $\mathcal{L}^{-1}$ is the inverse Langevin function, ($n^{\frac{1}{2}}$-1), which corresponds to the limiting network strain and N is the number of chains per cubic centimeter between the points of cross linking (or in this case between points of entanglement).

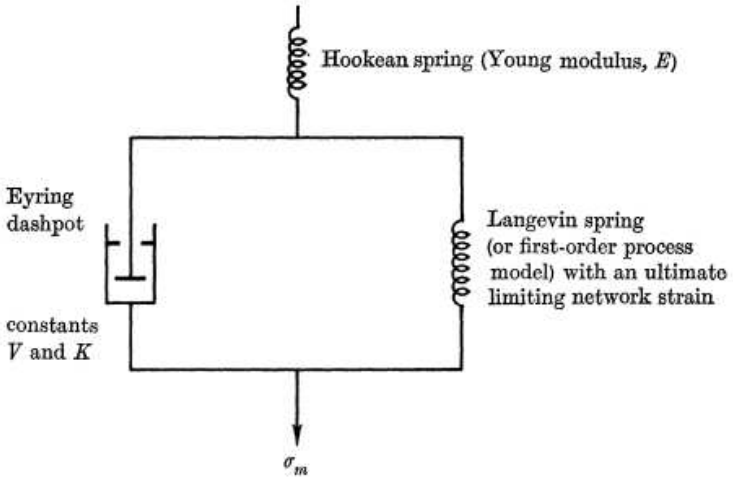

Figure 2.15. The rheological interpretation of Haward and Trackey[39]

Argon[40] presented a model based on the molecular mechanism of plastic flow. The model considers the intermolecular resistance and entropic resistance due to shear yielding and strain hardening, respectively. When the stress is applied, strain increases with the molecular alignment and the kinked chains in polymer align through direction of stresses (see Figure 2.16(a)). The molecular alignment was ascribed to entropic resistance, and it was represented with Langevin spring based rubber elasticity in the model. The shear stress-dependent activation free enthalpy (ΔG) of the Argon's model is given in Equation (2.6)

$$\Delta G = \frac{3\pi\omega^2 a^3}{16(1-v)}\left[1 - 8.5(1-v)^{\frac{5}{6}}\left(\frac{\tau}{\mu}\right)^{\frac{5}{6}}\right] + 0.15\mu a^3(\omega-\omega_c)^2\left(\frac{p}{\mu}\right) \qquad (2.6)$$

where ω and a are defined in Figure 2.16(b). μ is the shear modulus, v is the Poisson's ratio and p is the pressure. Argon considered the stability of the kinked configuration and how likely the chain was to return to its original ground state after kinking. The theory assumes that each chain only interacts with its two closest neighbors, in the plane of kinking. To return to the ground state, the kinked chain would need to either kink in the opposite direction, or cause one of its neighboring chains to kink, thus relieving its stored elastic energy. The theory weighs heavily upon the influence of intermolecular forces. The final expression of Argon's model shear strain rate is given in Equation (2.7)

$$\dot{\gamma} = \gamma_0 v_a N_a \exp\left[-\frac{\Delta G}{2k\theta}\right] \tag{2.7}$$

where γ_0 is the unit increment of shear strain that results from the production of a pair of kinks, N_a is the volume density of activated states, v_a is a frequency term capturing the rate at which the kinking process occurs, ω_c is the critical angle size such that the kinking process produces cavitation (increases free volume) and θ is the absolute temperature.

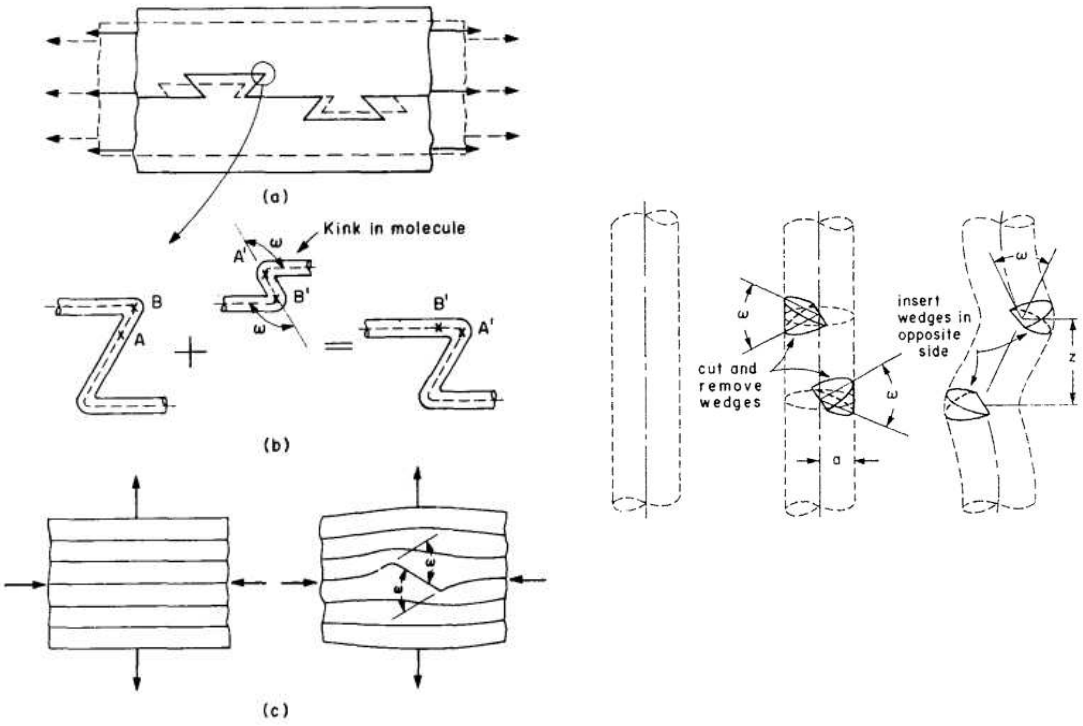

(a) (b)

Figure 2.16. Argon interpretation of molecular deformation as a result of stress: (a) previously kinked chains become aligned in the direction of straining and (b) geometrical parameters[40].

Boyce, Parks and Argon[41] proposed a phsical based constitutive model, called BPA model, for glassy polymers. The BPA model uses two parallel resistances: the intermolecular resistance for strain softening and the entropic resistance for strain hardening, sequentially given as follows in Equation (2.8) and (2.9)

$$\sigma_{A_\alpha} = \frac{1}{J_\alpha} + \mathcal{L}_\alpha^e\left[lnV_{A_\alpha}^e\right] \tag{2.8}$$

$$\sigma_{A_\beta} = \frac{1}{J_\beta} + \mathcal{L}_\beta^e \left[lnV_{A_\beta}^e \right] \tag{2.9}$$

where σ_{A_i} $(i = \alpha, \beta)$ is the Cauchy stress induced by the intermolecular resistance to the rotations of main-chain segments and the main chain phenyl group, J_i is the corresponding elastic volume change, $\mathcal{L}_i^e$ is the fourth order modulus tensor, and $lnV_{A_i}^e$ is the Hencky strain. It is assumed that the material is initially isotropic, and that the elastic behavior of the material may be decomposed into a and b components. The modulus tensors may be derived from any two component-specific elastic constants, such as the shear modulus μ and bulk modulus κ, as

$$\mathcal{L}_\alpha^e = 2\mu_\alpha \mathcal{J} + \left(\kappa_\alpha - \frac{2}{3}\mu_\alpha \right) I \otimes I \tag{2.10}$$

$$\mathcal{L}_\beta^e = 2\mu_\beta \mathcal{J} + \left(\kappa_\beta - \frac{2}{3}\mu_\beta \right) I \otimes I \tag{2.11}$$

where $\mathcal{J}$ and I are the fourth order and second-order identity tensors, respectively. The elastic constants, in this case, $\mu_i$and κ_i $(i = \alpha, \beta)$ are assumed to be functions of both temperature and strain rate. The stress in the non-linear hardening component, the network ‘‘back stress’’ due to the entropic resistance to molecular alignment, is taken to be deviatoric and is defined as in the earlier models using the Arruda-Boyce 8-chain interpretation of molecular alignment. The stress is given as in Equation (2.12)

$$\sigma_B = \frac{C_R}{3} \frac{\sqrt{N}}{\lambda_{chain}^P} \mathcal{L}^{-1} \left(\frac{\lambda_{chain}^P}{\sqrt{N}} \right) \overline{B}_B{}' \tag{2.12}$$

where $\lambda_{chain}^P$is the stretch on a chain in the eight-chain network C_R is the rubbery modulus; N is he number of rigid chain links between entanglements; $\mathcal{L}$ is the Langevin function and $\overline{B}_B{}'$is the deviatoric part of the left Cauchy-Green tensor. The total stress is given by the sum of the stresses induced by the intermolecular resistance to chain segment rotation and entropic resistance to chain alignment as shown in Equation (2.13)

$$\sigma = \sigma_{A_\alpha} + \sigma_{A_\beta} + \sigma_B \tag{2.13}$$

Richeton et al.[42] formulated high strain rate and glass transition regions of a PC for a wide range of strain rates and temperatures. The theory combined the internal stresses and cooperative motions in the polymer chain segments with the Eyring's model. Therefore, the model is also known as the Eyring's cooperative model. The cooperative model consisted of three parts. The effective stress, σ^*, is given in terms of internal stress, σ_i, and yield stress, σ_y, as

$$\sigma^* = \sigma_y - \sigma_i \tag{2.14}$$

Based on the model of Fotheringham and Cherry[43], the strain rate of the cooperative movement of chain segments with n elementary transitions is

$$\dot{\varepsilon} = \dot{\varepsilon}^* sinh^n \left(\frac{(\sigma_y - \sigma_i)V}{2kT} \right) \tag{2.15}$$

where V is an arbitrary activation volume and $\dot{\varepsilon}^*$ is the characteristic strain rate. Rearranging Equations 2.14 and 2.15 gives Equation 2.16 for the yield stress

$$\frac{\sigma_y}{T} = \frac{\sigma_i}{T} + \frac{2k}{V} sinh^{-1} \left(\frac{\dot{\varepsilon}}{\dot{\varepsilon}^*} \right)^{1/n} \tag{2.16}$$

Mulliken and Boyce[3] developed an elastic-viscoplastic rheological constitutive model and described the β viscoelastic transition at HSRs. The rate-dependent three-dimensional constitutive model, developed by Mulliken and Boyce[41], was extended for the predictive capabilities at high strain rates and low temperatures. Figure 2.17 shows an one-dimensional rheological interpretation of the Mulliken and Boyce[41] constitutive model for the rate-dependent thermoplastic behavior. The molecular network resistance of the stretching and alignment in this figure is represented by segment B, a nonlinear Langevin spring. Segment A is made of two sub-segments (α and β) and each of them has an elastic spring and viscoplastic dashpot connected in series. Segment A represents the intermolecular resistance of the chain-segment rotation. The two sub-segments (α and β) indicate the two different thermally activated processes. The α process relates to the rotation of the polymer main chain and the β-process to the local rotations of the main-

chain phenyl group. The contribution of $\beta - transition$ is significantly lower regarding intermolecular resistance than that of α-transition at high temperatures and low strain rates. $\beta - transition$ will be restricted and the intermolecular resistance will divide in two-part at low temperatures and HSRs.

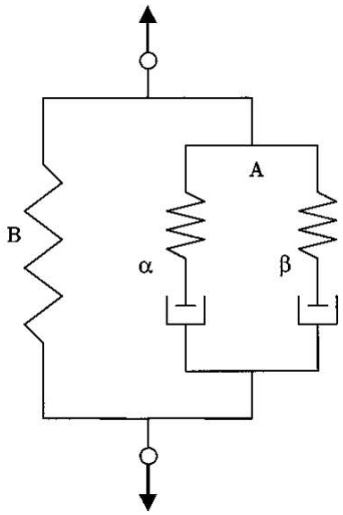

Figure 2.17. A one-dimensional rheological interpretation of the proposed constitutive model for rate-dependent thermoplastic behavior[3]

The phsical based model of Mulliken and Boyce[41] was also extended to include a wide range of temperatures by Richeton et al.[44] and to include the thermal softening due to adiabatic heating at HSRs by Varghese and Betra[45]. Safari et al.[46] proposed the model with one primary transition (α) and two secondary transitions (β and γ) (Figure 2.18). γ-transition is restricted, and the intermolecular resistance is divided in three-part at very low temperatures (-192°C) and high strain rates (~6000 s^{-1}). The yield stress equation is equal to the Equation (2.17)

$$\sigma_y = A_\alpha T\left(\ln(2C_\alpha\dot{\varepsilon}) + \frac{Q_\alpha}{RT}\right) + A_\beta T sinh^{-1}\left(C_\beta\dot{\varepsilon}\exp\left(\frac{Q_\beta}{RT}\right)\right) + A_\gamma T sinh^{-1}\left(C_\gamma\dot{\varepsilon}\exp\left(\frac{Q_\gamma}{RT}\right)\right) \quad (2.17)$$

where A_i and $C_i (i = \alpha, \beta$ and $\gamma)$ are material parameters and Q_i is the activation energy required for one transition. Al-Juaid and Othman[47] determined the tensile and

compressive yield strength of a PC at both quasi-static and high strain rates and modelled the strain rate dependent yield strength using four rheological constitutive equations.

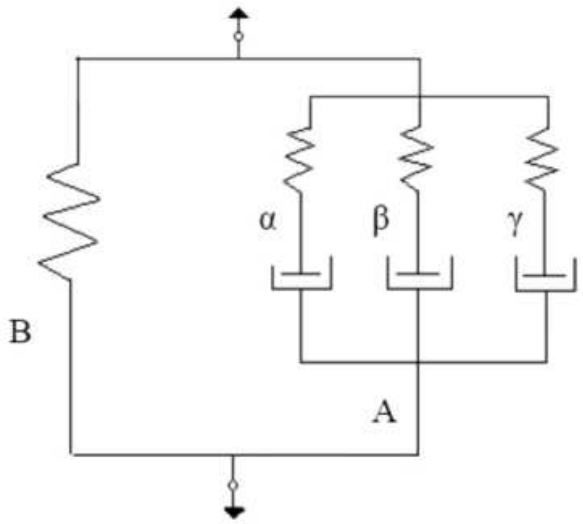

Figure 2.18. The rheological interpretation of the proposed constitutive model for rate-dependent thermoplastic behavior[46]

A linear dependence of the tensile and compressive yield strength on the logarithm of the strain rate was reported in the same study (Figures 2.19(a) and (b)). The first equation used was shown in Equation (2.18)

$$\sigma_{\pi} = q\left(\frac{\dot{\varepsilon}}{\varepsilon_0}\right)^{m} \tag{2.18}$$

where σ_{π} is the yield stress predicted by the power-law equation, $\dot{\varepsilon_0}$ = 1 s^{-1} is a normalizing constant, and q and m are two material constants. The second equation was shown Equation (2.19)

$$\sigma_{2\pi} = q_1\left(\frac{\dot{\varepsilon}}{\varepsilon_0}\right)^{m_1} + q_2\left(\frac{\dot{\varepsilon}}{\varepsilon_0}\right)^{m_2} \tag{2.19}$$

where $\sigma_{2\pi}$ is the yield stress predicted by the two-term power-law equation and q_1, q_2, m_1, and m_2 are four material constants. The third equation was Equation (2.20)

$$\sigma_c = \sigma_i + \frac{2kT}{V}\sinh^{-1}\left(\frac{\dot{\varepsilon}}{\dot{\varepsilon}^*}\right)^{1/n} \tag{2.20}$$

where σ_c, σ_i, V, $\dot{\varepsilon}^*$, and n are the yield stress as predicted by the cooperative model, the internal stress, the activation volume, a characteristic strain rate, and a material parameter, respectively. The fourth equation was shown in Equation (2.21)

$$\sigma_{ME} = \sigma_0 + \frac{2kT}{V_0}\exp\left(\sqrt{\frac{\dot{\varepsilon}}{\dot{\varepsilon}_c}}\right)\ln\left(\frac{\dot{\varepsilon}}{\dot{\varepsilon}_0}\right) \tag{2.21}$$

where V_0 and $\dot{\varepsilon}_c$ are two material constants. σ_{ME} is the yield stress predicted by the modified-Eyring equation. The two-term power-law equation was shown to well predict the yield stress as function of strain rate in both tension and compression (Figures 2.19(a) and (b)).

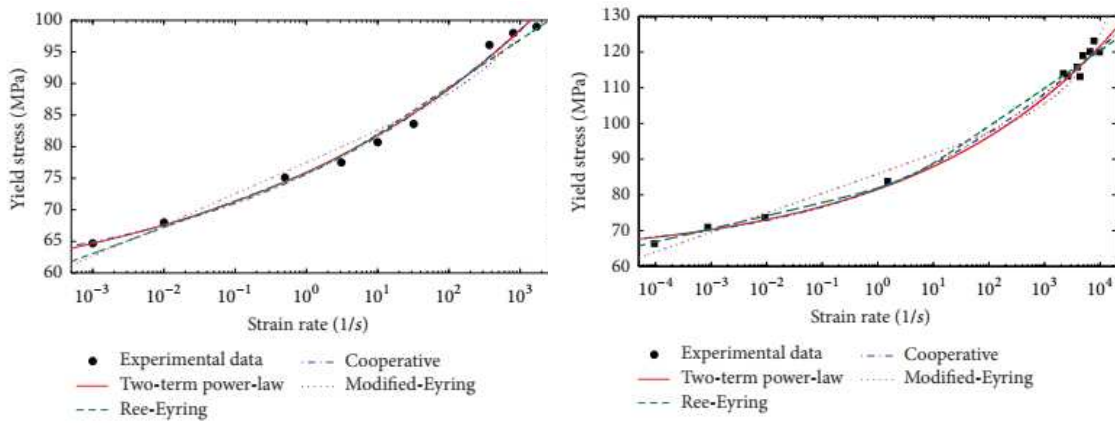

(a) (b)

Figure 2.19. The comparison of the four equations: (a) tension and (b) compression[47]

There have been numerous material model parameters that are needed to be determined for the flow stress equations in phsical based constitutive models. Furthermore, the damage equations are not included in these models. In other words, the incorporation of damage equations into physical based constitutive models has been still missing in the current literature. Although, the damage is not explicitly included in these models, numerical simulations can compensate for the lack of damage equations by incorporating macro-mechanical failure criteria.

Wang et al.[48] and Wang and Yue[49] developed a numerical model of PMMA aircraft windshield using UMAT in LS-Dyna. A damage-based elastic-viscoplastic and a

damage-modified nonlinear viscoelastic constitutive model were used in the simulations. Furthermore, the MAT_ADD_EROSION material model card was employed in LS-Dyna in order to capture the damage. Siddens et al.[50] used a micromechanical damage analysis code called GENOA. The code was combined with LS-Dyna in order to analyze the damage on a F-16 canopy exposed to bird strike. The failure in an element occurred, when the maximum principal stress on the element exceeded the ultimate strength. Yu et al.[51] investigated, both experimentally and numerically, the response and failure of PC plates against the soft body impact. The PC plate, in the same study, was modelled using the MAT_089_PLASTICITY_POLYMER material model card in LS-Dyna. In another study, Ramakrishnan[52] used the MAT_124_TENSION_COMPRESSION_PLASTICITY material model to analyze the low velocity impact behavior of a PC plate. The damage was defined, in the same study, by taking 0.5 strain as the critical effective plastic strain for the failure. Shah and Abakr[53] and Shah[54] used the MAT_003_PLASTIC_KINEMATIC material model to simulate the deformation of PC plates against the single and multiple impacts by the spherical projectiles. In both studies, the damage was defined by taking 1.5 strain as the critical effective plastic strain for the failure. In above studies, the critical strain was determined by the numerical iterations of the critical failure strain until the damages in the model approximated the experimental ones. In another numerical study in PAM-CRASHR, Meng et al.[55] used 0.2 strain as the critical strain for the failure. The studies outlined above used different critical strains for the failure.

Antoine and Barta[56, 57] studied the impact and penetration resistance of curved PC panels against hemispherical-nosed rigid cylinders using Mulliken and Boyce[3] constitutive relation that was modified by Varghese and Batra[45]. The model was represented by a nonlinear Langevin spring and two parallel nonlinear spring-dashpots, simulating the restoring force and the viscoplastic response, respectively. Wang et al.[48] presented a new damage-based elastic-viscoplastic constitutive model of PC within the framework of irreversible thermodynamics and continuum damage mechanics. This model was characterized by the mechanical responses and damage evolution of the material over a wide range of strain rates and temperatures. The elasticity behavior was modeled by a linear Hooke's spring, while four mechanical elements: a dashpot, a friction device, a spring and a damage device jointly described the post-yield inelastic behavior (Figure 2.20). The dashpot and the friction device presented the time dependent visco-plasticity, the damage device and the spring the damage-based strain softening and the

friction device and the spring the nonlinear strain hardening. Yield function included the damage parameters as follows in Equation (2.22)

$$\Phi(\sigma, \mathrm{D}, \dot{\varepsilon_0}, T, \bar{\varepsilon}^p) = \frac{\sqrt{3J_2(s)}}{1-D} - K\left(1 + C_r \dot{\varepsilon_{eq}}^m\right)(1 + C_t T_h) - C_h \gamma (\bar{\varepsilon}^p)^{\gamma-1} \qquad (2.22)$$

where $\frac{\sqrt{3J_2(s)}}{1-D}$ is a damage-based Von-Mises yield function, $\kappa = C_h \gamma (\bar{\varepsilon}^p)^{\gamma-1}$ is the thermodynamic force associated with hardening and $K\left(1 + C_r \dot{\varepsilon_{eq}}^m\right)(1 + C_t T_h)$ is the strain rate and temperature dependent initial yield function.

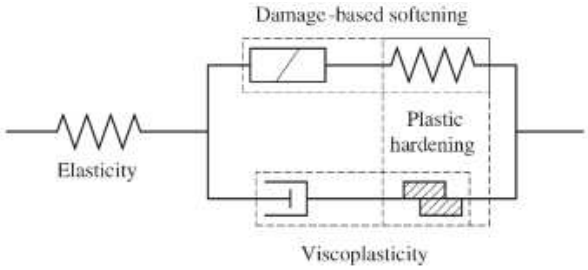

Figure 2.20. The rheological representation of the Wang's model[48]

There have also been the phenomenological constitutive models to predict the mechanical behavior of PC such as the G'Sell Jonas[6], DSGZ[58], and ZWT[23]. The G'Sell-Jonas[6] model captures the initial elasticity and the yield and strain hardening of polymeric materials, while it cannot capture the strain softening behavior. The DSGZ model is based on four models: the JC [59], the G'sell-Jonas, the Matsouka[60] and the Brooks[61]. The JC model is mostly used for metals. The flow stress part of the JC model captures plastic strain, strain rate and temperature dependencies of mechanical behavior. The G'sell-Jonas integrates the viscoelasticity and viscoplasticity in one equation. Three functions are used to consider the initial non-linear elastic behavior, plastic strain-hardening and strain rate-dependence of viscous behavior. The Matsouka model describes the non-linear viscoelasticity, yielding and subsequent strain-softening behavior of glassy polymer. The Brooks model employed two Eyring processes acting in parallel for the description of the yield stress at a wide range of temperatures and strain rates. The DSGZ model overcomes this limitation of the G'Sell-Jonas[6] model, and it can accurately predict the large deformation of PC, PMMA and ABS at low strain rates for various temperatures, while it cannot accurately simulate the deformation of polymeric materials at HSRs. The G'sell Jonas formula is given as[6] follows in Equation (2.23).

$$\sigma(\varepsilon, \dot{\varepsilon}, T) = K \exp(\mathrm{h}\varepsilon^2)\,[1 - \exp(-W\varepsilon)(\frac{\dot{\varepsilon}}{\dot{\varepsilon}_0})]^{m} \exp\left(\frac{a}{T}\right) \tag{2.23}$$

where K, a, W, h and m are the material coefficients. The function $1 - \exp(-W\varepsilon)$ takes into account the initial non-linear elastic behavior, the function $\exp(\mathrm{h}\varepsilon^2)$ describes the plastic strain hardening, and the function $\dot{\varepsilon}^m$ describes the viscous behavior. This equation predicts well the behavior of semi crystalline polymers, but it is unable to reproduce the intrinsic strain-softening behavior of glassy polymers. The Matsouka formula is given as[60] follows in Equation (2.24)

$$\sigma = E_0 e^{-C\varepsilon} \varepsilon e^{-\left(\frac{\varepsilon}{\dot{\varepsilon}\tau}\right)^{\beta}} \tag{2.24}$$

where τ is effective relaxation time associated with temperature, and E_0, C, and β material coefficients. This model depicts the non-linear viscoelasticity, yielding and subsequent strain softening behavior of glassy polymers. The Brooks formula is given as[61] follows

$$\sigma = K\lambda_{zz}^{m}\{\lambda_0\lambda_{zz}^{q} + [1 - \lambda_0\lambda_{zz}^{q}]e^{-\alpha\varepsilon}\}(1 - e^{-\beta\varepsilon}) \tag{2.25}$$

where

$$\lambda_{zz} = \dot{\varepsilon} e^{\frac{Q}{RT}} \tag{2.26}$$

where K, m, λ_0, q, α and β are the material coefficients. The Brooks model cannot predict the strain-hardening behavior, but part of this model is useful for the proposed constitutive model. Consider the term $\lambda_0\lambda_{zz}^{q} + [1 - \lambda_0\lambda_{zz}^{q}]$ with increased strain ε, the term approaches exponentially from an initial value of 1 (when ε = 0) to a steady state value. If the initial value of 1 is replaced by some expression describing the initial deformation, and the steady state value $\lambda_0\lambda_{zz}^{q}$ is replaced by some expression describing the large deformation of polymers, a constitutive model capable of describing both the viscoelasticity and viscoplasticity behavior of polymers probably can be developed in Equation (2.27).

$$\sigma(\varepsilon, \dot{\varepsilon}, T) = K\left\{f(\varepsilon) + \left[\frac{\varepsilon e^{\left(1 - \frac{\varepsilon}{C_3 . h(\dot{\varepsilon}, T)}\right)}}{C_3 . h(\dot{\varepsilon}, T)} - f(\varepsilon)\right] . e^{[\ln(g(\dot{\varepsilon}, T)) - C_4] . \varepsilon}\right\} . h(\dot{\varepsilon}, T) \tag{2.27}$$

where

$$f(\varepsilon) = (e^{-C_1.\varepsilon} + \varepsilon^{C_2}).(1 - e^{-a\varepsilon}) \quad (2.28)$$

$$h(\dot{\varepsilon}, T) = (\dot{\varepsilon})^m e^{\frac{a}{T}} \quad (2.29)$$

$g(\dot{\varepsilon}, T)$ is defined be the dimensionless form of $h(\dot{\varepsilon}, T)$. The eight material coefficients in this model are K(Pa.s^m), C_1, C_2, C_3(s^m), C_4 a(K), m and a. Furthermore, $\frac{\varepsilon e^{\left(1-\frac{\varepsilon}{C_3.h(\dot{\varepsilon},T)}\right)}}{C_3.h(\dot{\varepsilon},T)}$ describes the shift behavior of the yield point with strain rate and temperature for glassy polymers. $(\dot{\varepsilon})^m e^{\frac{a}{T}}$ represents the stress dependence on strain rate and temperature. The model uniformly describes initial nonlinear viscoelasticity, yielding, strain softening and subsequent strain hardening deformation under uniaxial compression loading.

The ZWT[23] model uses a nonlinear spring and two Maxwell elements in parallel (Figure 2.21(a)), and it can capture the deformation feature of PMMA both at low and HSRs, while the strain hardening feature of PMMA cannot be predicted by the ZWT[23] model[62]. Furthermore, the ZWT[23] was employed for the modelling the PC windshield. Zhu et al.[23] studied full-scale aircraft windshield model. The windshield was damaged when the bird impact velocity was larger than 365 km h^{-1} and tensile failure occurred in the windshield (Figure 2.21(b)). The model is given in Equation (2.30).

$$\sigma = E_0\varepsilon + \alpha\varepsilon^2 + \beta\varepsilon^3 + E_1\int_0^t \dot{\varepsilon}\exp\left(-\frac{t-\tau}{\theta_1}\right)d\tau + E_2\int_0^t \dot{\varepsilon}\exp\left(-\frac{t-\tau}{\theta_2}\right)d\tau \quad (2.30)$$

where E_0, α and β are the nonlinear elastic parameters. The first integration term in Equation (2.28) describes the viscoelastic response for low strain rates, in which E_1, θ_1 are the elastic modulus and relaxation time of the corresponding Maxwell element I respectively. The second integration term describes the viscoelastic response for HSRs, in which E_2, θ_2 are the elastic constant and relaxation time of the corresponding Maxwell element II respectively. Similar to the physical based constitutive models, these phenomenological models cannot thoroughly explain the deformation mechanism of the PC and they cannot predict the large deformation of polymers from low to HSRs. Dorogoy and Rittel[63] stated that the numerical results highly depended on the failure properties.

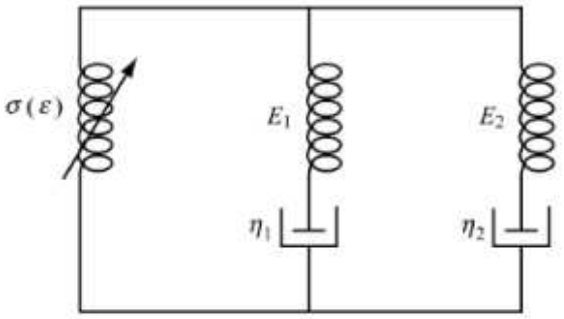

(a)

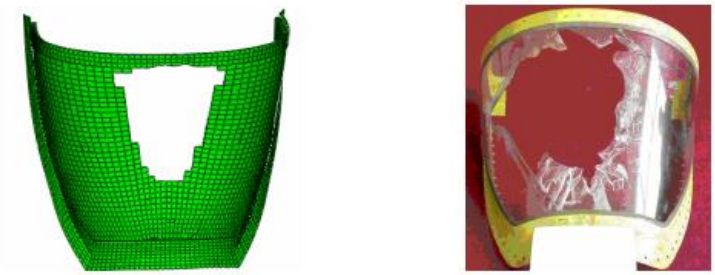

(b)

Figure 2.21. (a) The ZWT model and (b) comparison of numerical model (left) and test (right)[23]

Therefore, the failure strains of PC corresponding to strain rate, temperature and triaxiality need to be determined. Wang et al.[64] experimentally investigated the effect of stress triaxiality on the deformation behavior of PC. The tested PC exhibited a sharp strain softening following the yielding at the intermediate triaxialities and thoroughly brittle behavior at the higher level triaxialities (Figure 2.22). Castagnet and Deburk et al.[65]and Manaia et al.[66] tested the polymer specimens with stress triaxialities in order to understand the cavitation damage and mechanical response of semi-crystalline polymers (Bridgman[67] approach). The JC[59] constitutive equation, originally developed for metals, has also been used to model the deformation of PC. Furthermore, the damage equation part of the JC constitutive equation captures strain, stress triaxiality and temperature. Dwivedi et al.[68] determined the parameters of the JC flow stress model of a PC. Xu et al.[69] modelled the Izod impact test of a PC using a JC flow stress model with the modifications to the thermal history. This study shows that fracture energy increases since the temperature increases. When the temperature increased, the plastically fractured and deformed PC specimen absorbed a greater amount of impact energy.

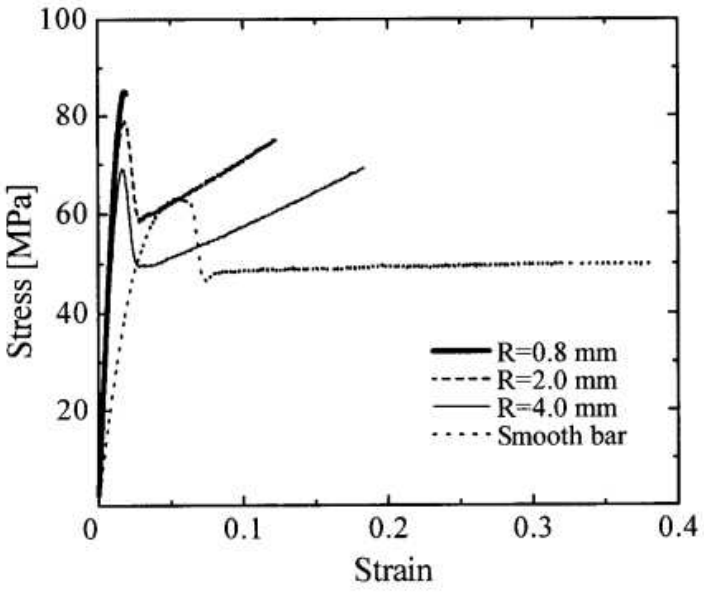

Figure 2.22. The stress-strain curve for PC in different triaxial stress[64]

In these studies, the damage was defined by the effective plastic strain criterion[53, 54].

2.6. Bird strike

The PC components in aircrafts are subjected to foreign object impact such as the bird strike[70] and space debris [20] and hail impacts[71] at the impact velocity above 150 m s^{-1}. These impact accidents are serious threats to the operation safety of civil aircraft and may cause catastrophic damages. Particularly, the bird strike and its model are crucial to analyze the damage formation on the windshield of aircrafts (usually made of PC) during flight. Abrate[72] summarized the bird strike design criteria for the aircraft components including windshields which are tabulated in Table 2.1. In the criteria, a 1.8-kg bird is impacted to the aircraft components at a velocity of 152.4 m s^{-1} and at a kinetic energy of 21.1 kJ. The applied pressure should be 10.45 MPa and it should be applied to an area of 12,903 mm^2. The Wilbeck's experiments[73] were previously used for the validation of numerical bird model. These experiments investigated the deformation behavior of a substitute bird under impact. Substitute birds include such as gelatin, beef, RTV rubber, and neoprene. The experiments showed that the most suitable material for the substation of bird was gelatin having a porosity of 10% and a density of 950 kg m^{-3}. Thereafter, Lavoie et al.[74] developed a recipe for the gelatin birds.

Table 2.1. The bird strike design criteria[72]

Property	
Impact velocity	152.4 m s^{-1}
Bird mass	1.814 kg
Kinetic energy of a bird	21.1 kJ
Applied pressure	10.45 MPa
The area that pressure applied on	12,903 mm^2

The recipe consisted 1000 g of cold water, 100 g of ballistic gelatin powder, 25 g of sodium carboxymethylcellulose, 6 g of aluminum acetate basic and 4 drops of cinnamomum zeylanioum. Thereafter, Shupikov et al.[75] developed a new substitute for the bird and tabulated commonly used substitute bird materials. In the Wilbeck's experiment, the birds and substitutes were impacted on an 1x1 m rigid steel plate at the velocities ranging from 100-300 m s^{-1}. The peak and steady flow pressures at the center of the impact were then determined. Cwiklak et al.[76] determined the values of normalized Hugoniot's and steady-flow pressure at a speed of 116 m s^{-1}, as obtained by other researchers. The differences in the normalized flow pressure range from 3.6 to 14.1 for the Hugoniot pressure and from 0.5 to 1.58 for a stagnation one. The values should be multiplied with ~6.39 to determine the Hugoniot peak and steady flow pressure values. In the experiment performed by Welsh and Centonze[77], the bird was impacted on a 6.35 mm thick T6061-T6 aluminum plate with a velocity of 146 m s^{-1} and the corresponding plastic deformation of the plate was measured. The numerical simulations FE simulations were then performed in accordance with the experimental parameters and the residual plastic deformation of the plate after impact was determined. The experimentally determined plastic deformation value was 41.275 mm.

The bird impact tests on both rigid steel plates (the Wilbeck's[73] experiment) and deformable aluminum plates (the Welsh and Centonze's[77] experiment) are necessary to accurately predict the bird impact in the numerical models. The obtained data from these experiments can be used to verify the results of the numerical model. The material model, EOS, and computational methods (Lagrangian and SPH) are other parameters that need to be determined for developing bird impact numerical simulation.

The commonly used material models for bird are mainly MAT_009_NULL and MAT_010_ELASTIC_PLASTIC_HYDRO. The MAT_009_NULL material model card

possesses no yield strength and provides a fluid-like behavior. It includes density, tension and compression erosions, viscosity coefficient and pressure cut off parameters. TEROD denotes the relative volume for erosion in tension and is set greater than unity while the parameter CEROD represents the relative volume for erosion in compression and is set less than unity. When the pressure inside the material drops below the pressure cut off limit then the cavitation occurs within the material.

The MAT_010_ELASTIC_PLASTIC_HYDRO material model card employs yield stress and tangent modulus. The plastic behavior of bird is combined with the EOS parameters. There have been mainly two types of the EOS employed in the numerical simulations: the polynomial EOS and the Mie-Gruneisen EOS. The polynomial EOS for the bird model describes an isotropic and non-viscous constitutive law. The pressure-density relationship of the bird model is mostly represented by a third-degree polynomial. The Mie-Gruneisen EOS, on the other side, describes a linear relationship between the shock and particle velocities. The shock velocity of the Gruneisen EOS varies with the loading types, particularly with compression and tension. The computational methods[78] are mainly the Lagrangian and SPH approach. The nodes are fixed to the material and deform accordingly with the material in the Lagrangian[78] approach. The vast problem in the Lagrangian approach is severe mesh distortions at large deformations. These mesh distortions induce inaccurate results and error termination due to the negative volume elements. The SPH[78] approach is a meshless Lagrangian approach. In this case, the fluid is denoted as a set of discrete interacting particles which are independent from each other. These discrete interacting particles enable to yield large deformations without the problem of mesh distortion. The Lagrangian and SPH bird impactors were documented by Airoldi et al.[79] and Liu et al.[80] for deformable PC plate and aviation organic glass, respectively.

Grimaldi et al.[81] used the SPH method to simulate the bird strike on an aircraft windshield. The effect of the curvature and the thickness ratio of a glass-polyvinylbutyral (PVB) on the impact energy in this study are shown in Figure 2.23. It is shown that as the curvature increases the energy required for the deformation drops depending on the amount of PVB in the plates. Particularly, a higher amount of PVB results in greater energy drops (Figure 2.23). Siddens et al.[50] developed a numerical approach in LS-Dyna for identifying specific damage mechanisms in F-16 canopy subjected to soft impacts at low impact velocity (180 m s^{-1}) and the high impact velocity (230 m s^{-1}) of bird (Figure 2.24).

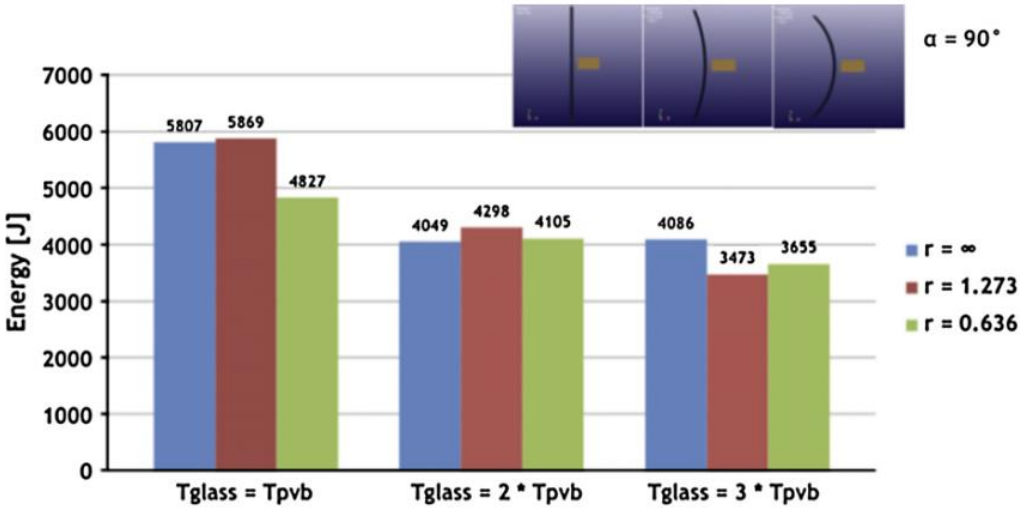

Figure 2.23. The maximum energy as curvature [81] for $\alpha = 90°$

The developed numerical approach was well-predicted the large deformation responses of both low and high impact velocities. Plassard et al.[82] studied the inclined bird strike impact with a dead chicken to a PC plate having a thickness of 8 mm at a velocity of 125 m s^{-1}. The deformation type of the PC was shown elastic due to low h/d ratio, below 0.25. Dar et al.[70] compared the effects of the substitute bird and realistic bird on the crashworthiness of aircraft windshield and canopy structure. The numerical model was implemented in LS-Dyna. The realistic and substitute birds were modeled elasto-plastic hydrodynamic material model by using the SPH approach (Figure 2.25(a)). The analysis revealed that the impact of bird from bottom direction required relatively less velocity to initiate failure in the windshield followed by head, tail and wing side (Figure 2.25(b)). This study highlighted the effect of real bird model and its impact direction in design optimization of aircraft structure against bird impact threats. The earlier numerical studies on canopy structures have been implemented using UMAT in LS-Dyna. However, the strain rate sensitivity and damage model of PC are still ambiguous. In the present study, the JC flow[59] stress and damage[83] model parameters of a PC plate were determined by the experimental mechanical tests and the numerical simulations of these tests. There have been four approaches to identify the relationship between yield stress and strain rates in the JC flow stress model. HK[84], ARJ[85], CS[86] and NLA[87] can modify yield stress-logarithmic strain rate with different strain rate sensitivity approaches. The validities of these equations and damage model parameters were calibrated by the experimental and numerical QSI, LVI and PI tests.

(a) (b)

Figure 2.24. The PC canopy damage types[50] (a) 180 and (b) 230 m s^{-1}

The calibrations of the models were performed by simply iterating the flow stress and damage parameters numerically. The strain rate sensitivity parameters of the used flow stress relations were extracted from the experimental compression peak strengths obtained both from the quasi-static and HSR tests. Thereafter, a 1.8 kg straight ended cylindrical SPH bird model with a diameter of 120 and the length of 140 mm was calibrated first by the numerical model of Wilbeck's experiment and second by the Welsh and Centonze's experiment in LS-Dyna. Eventually, the canopy structures with a thickness of 6 and 10 mm were subjected to a bird impact at the velocity of 116, 140 and 230 m s^{-1} and the damages of the canopy structures were monitored and analyzed numerically.

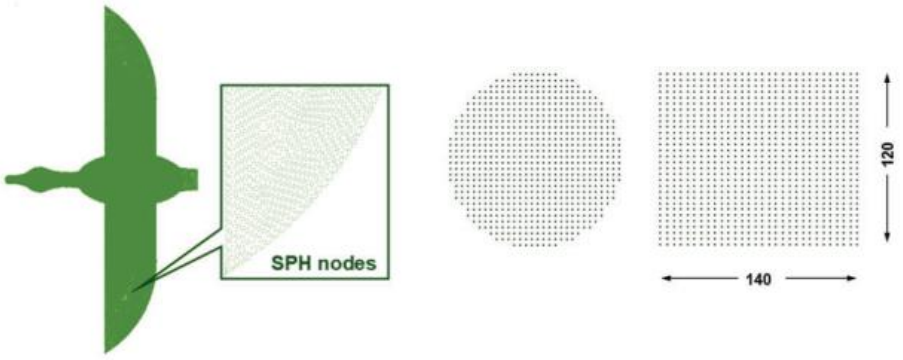

(a)

(cont. on next page)

Figure 2.25. The numerical model of (a) realistic (left) and substitute bird (right) and (b) deformation pictures of aircraft cockpit subjected to tail side, bottom side, wing side and substitute bird (from top to bottom)[70]

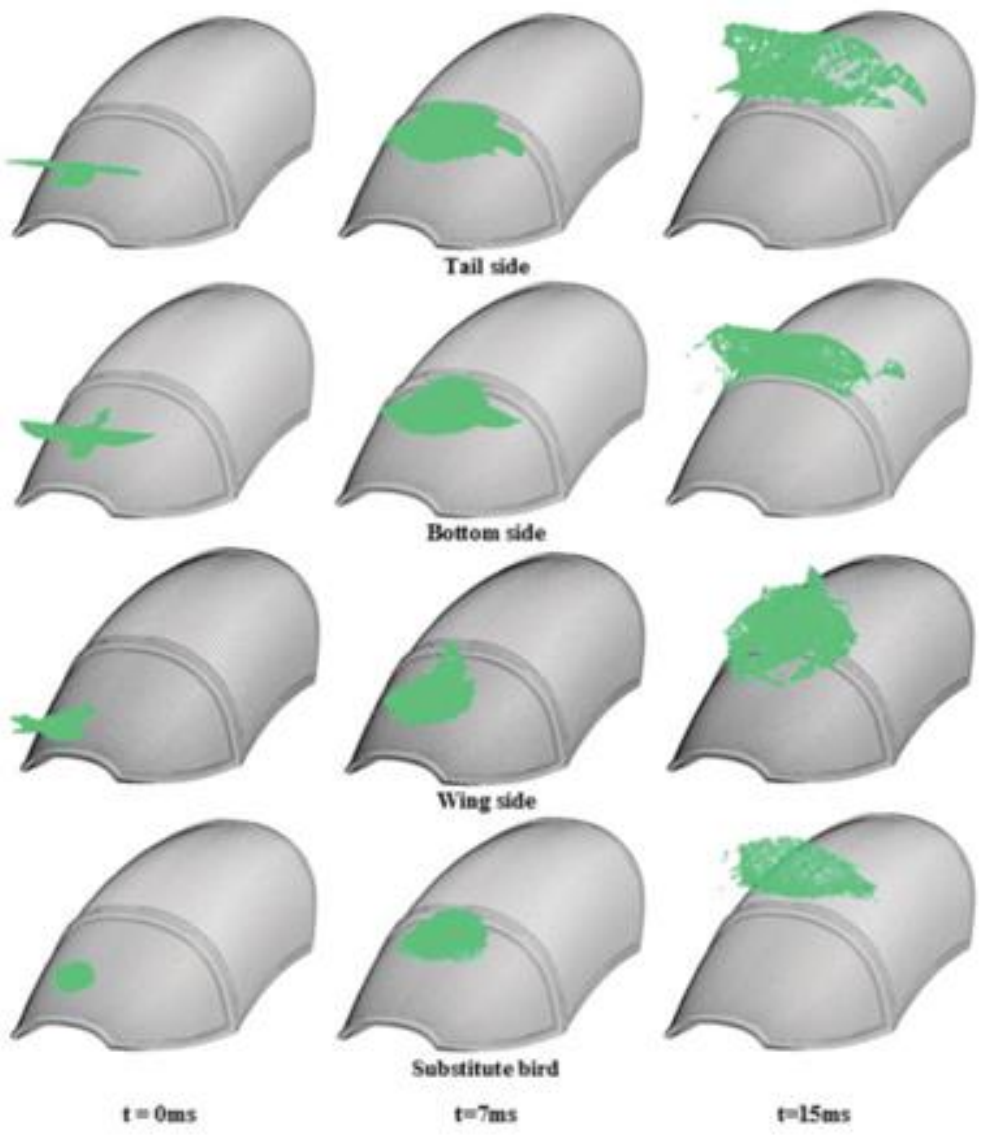

(b)

Figure 2.25. (cont.)

CHAPTER 3

MATERIALS AND TESTING

Chapter 3 includes test specimens and experimental methodologies used in this thesis.

3.1. Materials and test specimens

In order to determine the numerical flow stress and damage model parameters of PC, tension, compression, low velocity impact and projectile impact tests were performed. The tensile and compression tests were performed at different strain rates, and tensile tests were also performed at different temperatures. The test specimens were machined using an extruded Lexan 141R PC plate, received from a local supplier with a thickness of 10 mm, a length of 3000 mm (along the extrusion direction) and a width of 2000 mm. The tension and compression test specimens were prepared by slicing the as-received plate in the extrusion direction using a CNC router as depicted in Figure 3.1. From these slices, rectangular and circular tensile test specimens and circular compression test specimens were machined using a CNC lathe. The specimen geometries, pictures and strain rate/velocity of the tests performed in the context of present thesis are shown in Figure 3.2.

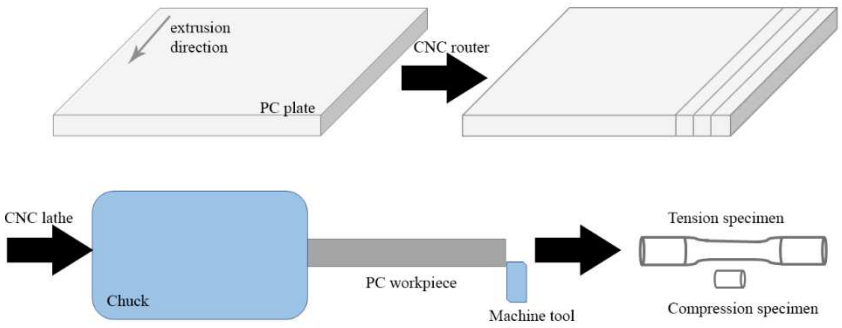

Figure 3.1. The schematic of PC plate and the specimen preparation directions.

The ASTM standard D638 [88] rectangular cross-section tensile test specimens were used to determine the Poisson's ratio of PC and performed at a crosshead speed of 5 mm min^{-1}. In these samples, 350 Ω foil strain gages (Vishay, C2A-06-125LT-350, 5 mm in width) were glued on the specimens in both longitudinal and transverse directions. The strain readings were recorded in an oscilloscope (Tektronix Mixed Domain Oscilloscope (MDO) 3024 200 MHz 2.5 GS/s) and amplifier (Vishay 2310B Signal conditioning system, 115/230V 50-60 Hz 40W Max) with a gain of 200 and 10 V excitation voltage. The strain was calculated using the single bridge equation as

$$\varepsilon = \frac{V_o}{4V_e KG} \tag{3.1}$$

where V_o is the bridge voltage, K is the gage factor and G is the gain. The Poisson's (v) ratio was calculated as,

$$v = -\frac{\varepsilon_t}{\varepsilon_a} \tag{3.2}$$

where ε_t and ε_a were the measured transverse and axial strains, respectively. The circular quasi-static strain rate tensile test specimens with and without notches were prepared in accordance with the ASTM standard E8[89]. The quasi-static compression tests were performed using cylindrical test specimens having a length to diameter ratio (L/D) of 1 and a diameter of 4 mm as shown in Figure 3.2. The SHTB test specimens had the same diameter as the quasi-static strain rate test specimens, but the gage length was reduced to 5 mm in order to attain the stress equilibrium in the HSR tests. The SHPB test specimens had the same diameter with the quasi-static strain rate compression test specimens, 4 mm in length and 4 mm in diameter. The quasi-static tension tests were performed at three different strain rates, 10^{-3}, 10^{-2} and 10^{-1} s^{-1} and the compression tests at four different strain rates, 10^{-3}, 10^{-2}, 10^{-1} and 1 s^{-1} while HSR tests were performed between 1200-4500 s^{-1}.

The notched tensile test specimens with circular cross-section (axisymmetric) seen in Figure 3.2 were used to determine the effect of stress-triaxiality (σ^*) on the failure strain. Three notched specimens having the stress triaxialities of 0.49, 0.56 and 0.74 were tested at the crosshead speeds of 9 x 10^{-3}, 7 x 10^{-3} and 4 x 10^{-3} mm s^{-1}, respectively.

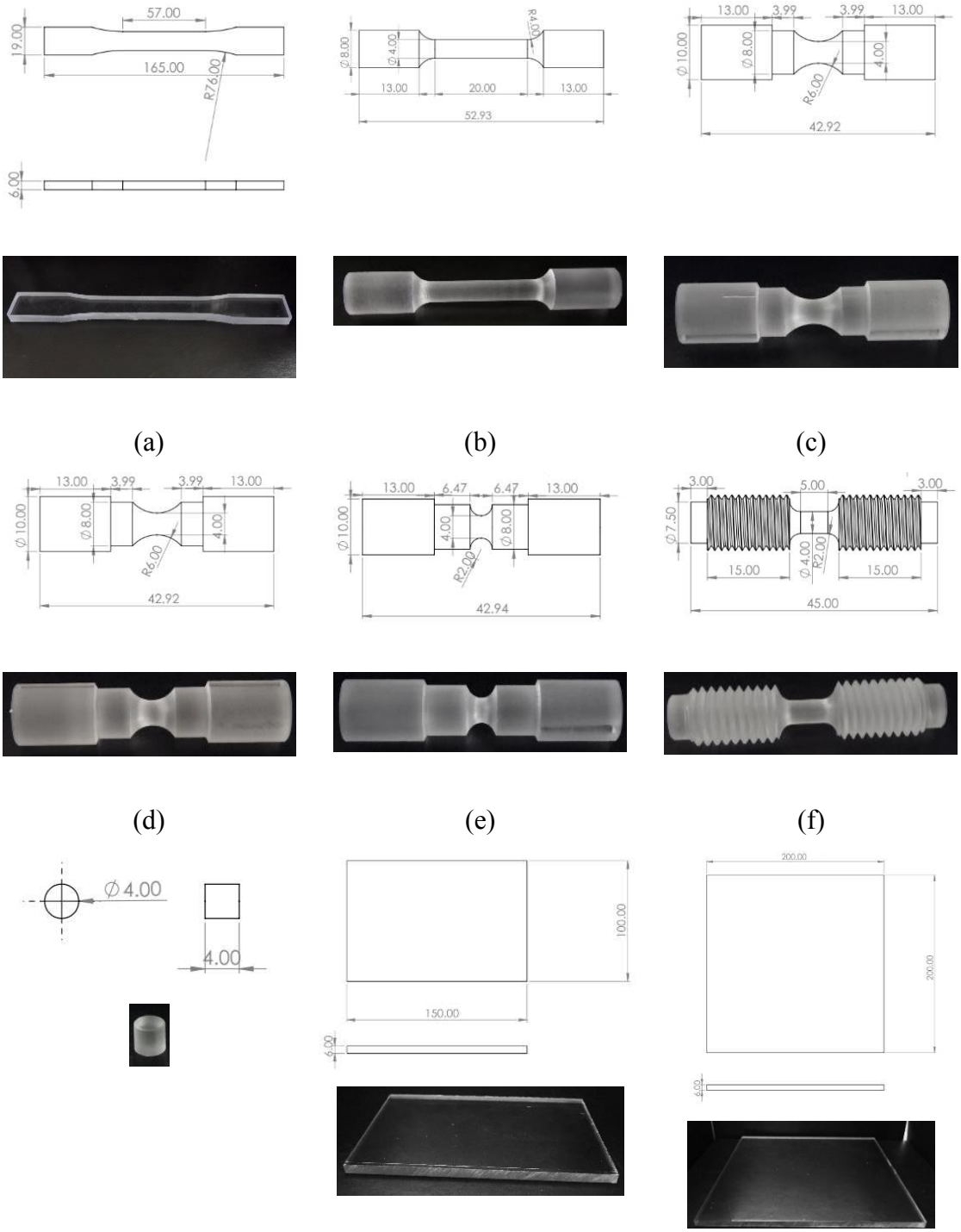

Figure 3.2. (a) the quasi static tension dogbone, (b) the quasi static tension ($\sigma^* = 0$, (c) the quasi-static tension triaxiality R6 , (d) the quasi static tension triaxiality R4 , (e) the quasi-static tension triaxiality R2, (f) the HSR tension, (g) the quasi static compression and the HSR compression , (h) the quasi static indentation and low velocity impact and (i) the projectile impact test specimens

The stress triaxiality is

$$\sigma^* = \frac{\sigma_h}{\bar{\sigma}} = \frac{1}{3} + ln\left(1 + \frac{a}{2R}\right) \tag{3.3}$$

In above equation, σ_h is the hydrostatic stress, and $\bar{\sigma}$ is the equivalent stress. R is the radius of groove and a is the radius of the specimen at groove as shown in Figure 3.3. Hydrostatic stress is given as

$$\sigma_h = \frac{\sigma_x + \sigma_y + \sigma_z}{3} = \frac{\sigma_1 + \sigma_2 + \sigma_3}{3} \tag{3.4}$$

where, σ_x, σ_y and σ_z are the applied stresses in the x-, y- and z-axis and σ_1, σ_2 and σ_3 are the principal stresses in the principal plane 1, 2 and 3, respectively. The Von-misses equivalent stress is

$$\bar{\sigma} = \frac{1}{\sqrt{2}}\sqrt{(\sigma_1 - \sigma_2)^2 + (\sigma_2 - \sigma_3)^2 + (\sigma_3 - \sigma_1)^2} \tag{3.5}$$

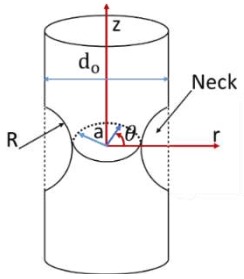

Figure 3.3. The geometrical parameters of a circular notched specimen: a, and R.

3.2. Quasi-static room temperature tests

The quasi-static tension and compression tests were performed in a Shimadzu AG-X 300 kN universal testing machine, depicted in Figures 3.4(a) and (b), respectively. A extensometer was used to measure the displacements both in tension and compression. The surfaces of compression specimens were lubricated using grease before the test to reduce the friction in the contact points. In a few tests, DIC method was used by coating specimens with a white paint and then black points with air brush (Figure 3.5). the DIC analysis was performed on the frames using a Matlab-code (Ncorr) [90].

3.3. Quasi-static elevated temperature tests

Elevated temperature tension tests at 60 and 90^{o}C were performed using a split furnace (ALSER) inserted into the universal test machine (Figure 3.6). Specially designed grips were used to hold the specimens during the tests. The temperature of test specimens was measured both externally and in-situ by using thermocouples.

3.4. High strain rate room temperature tests

The specimens were tested both in tension and compression at HSRs by using SHTB and conventional compression SHPB. The schematic and the picture of the used SHTB set-up are shown in Figures 3.7(a) and (b), respectively. The incident and transmitter bars were all made of 316L stainless steel (2 cm in diameter), with a 316L striker tube with a length of 30 cm (2 cm inner diameter and 2.9 cm outer diameter). The incident and transmitted bar lengths were equal and 241 cm. The mechanical and physical properties of the bar material are as follows: Elastic modulus=193 GPa, density=8000 kg m^{-3} and yield strength= ~300 MPa. The loading of the specimens in SHTB testing was captured using a Photron Fast-Cam high speed camera at 100,000 fps. In a typical SHTB test, a gas gun fires a striker tube to the steeped end of the incident bar (see the inset of Figure 3.7(b)). This creates a tension wave on the incident bar which moves to the sample-bar interface where it is partly reflected as compressive wave to the incident bar and partly transmitted as tension wave to the transmitter bar. The incident reflected and transmitted waves are measured by means of strain gages mounted on the incident and transmitter bars. The strain rate, strain and stress in the sample are calculated using the equations based on one-dimensional wave propagation in long bars. The plate specimens were inserted into the SHTB test machine using specimen grips as depicted in Figure 3.7(a). The specimens were placed to the inset of the grips and tightened using stainless steel pins (Figure 3.7(a)). Then, the grips were screwed to the bars tightly. The axisymmetric samples were directly screwed to the bars. In both case, there existed wave reflections from the pins and treats. Therefore, the pins and the specimen surfaces were filled with an epoxy-based glue (Bison). With these modifications, the early wave reflections were avoided and only the specimen gage length was experienced extension during a test. In a few tests, semi-circular Al (1010) pulse shapers having almost the same inner diameter with the bars were inserted in the front of flange as seen in the inset of Figure 3.7(b). With the deformation pulse shaper, a gradually increasing incident wave was obtained as

shown in Figure 3.7(c). The compression SHPB set-up consisted of a 1.940 cm diameter Inconel 718 bar; 200 cm-long incident bar, 180 cm-long transmitted bar and 50 cm-long striker bar. The elastic modulus and density of the bar were sequentially 204 GPa and 8394 kg m^{-3}. The details of the used SHTB and SHPB set-up are given in reference[91] and reference[92], respectively. The stresses on the bars were measured by a full Wheatstone-bridge configuration of 350 Ω foil strain gages. After recording the waves using an oscilloscope and amplifier, the strain (ε_s), stress (σ_s) and strain rate ($\dot{\varepsilon}_s$) of the sample were using the following relations

$$\varepsilon_s(t) = -\frac{2C_b}{L_s}\int_0^t \varepsilon_R(t)\,dt \tag{3.6}$$

$$\sigma_s(t) = \frac{A_b}{A_s}E_b\varepsilon_T(t) \tag{3.7}$$

$$\dot{\varepsilon_s}(t) = -\frac{2C_b}{L_s}\varepsilon_R(t) \tag{3.7}$$

where L_s, A_b, A_s, E_b, C_b and t are the specimen length, the bar cross-sectional area, the specimen cross-sectional area, the bar elastic modulus, the bar elastic wave velocity and the time, respectively. ε_R and ε_T are the reflected and transmitted strains, respectively. The pulse shaping method is widely used to induce a gradual rise in incident wave in the 2700 and 4500 s^{-1} rated tests. In this method, a thin layer of a ductile material is placed at the front of the incident bar so that the deformation of the thin-metal layer in between the striker and incident bar shapes the incoming incident bar stress (Figure 3.8(a)). In the present study, a copper sheet in 5x5x1 mm size was placed at the front of the incident bar by applying grease with a thin layer. All the SHPB test setup is shown in Figure 3.8(b). Figure 3.8(c) shows typical voltage-time readings of a SHPB test with and without using a pulse shaper. The pulse shaper induces a more gradually rising stress wave on the incident bar and results in steady oscillations of the strain rate during the testing. In the classical SHPB tests, the strain gages on the incident and transmitter bar are placed at an equal distance from the specimen/bar interfaces so that the reflected and transmitted pulses start at the same point in the time domain.

(a)

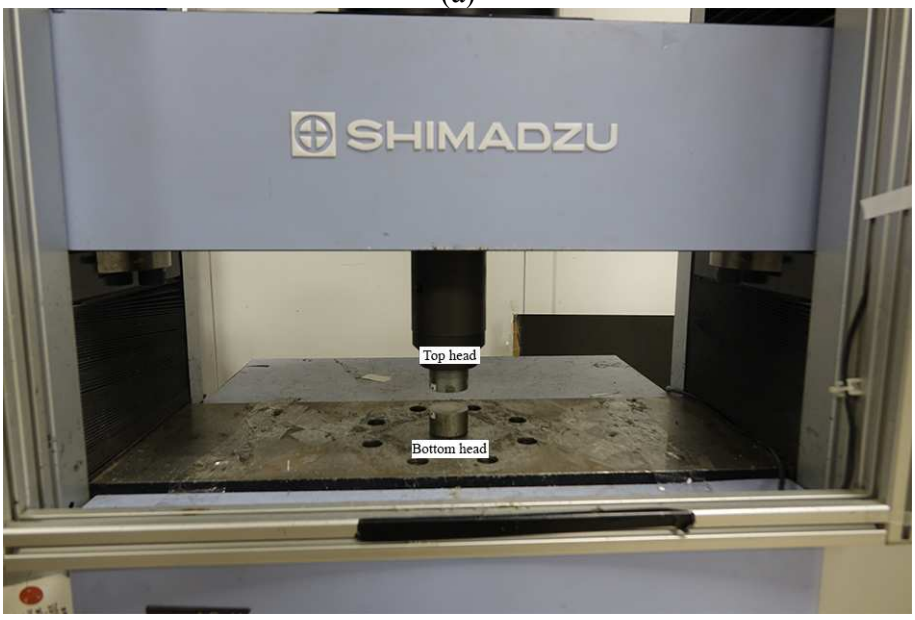

(b)

Figure 3.4. The quasi-static (a) tension and (b) compression test set-up

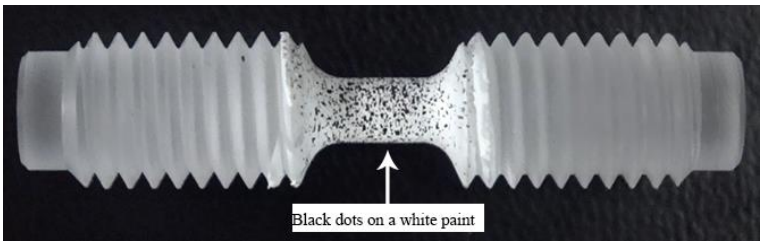

Figure 3.5. The picture of a specimen with paint for DIC measurement

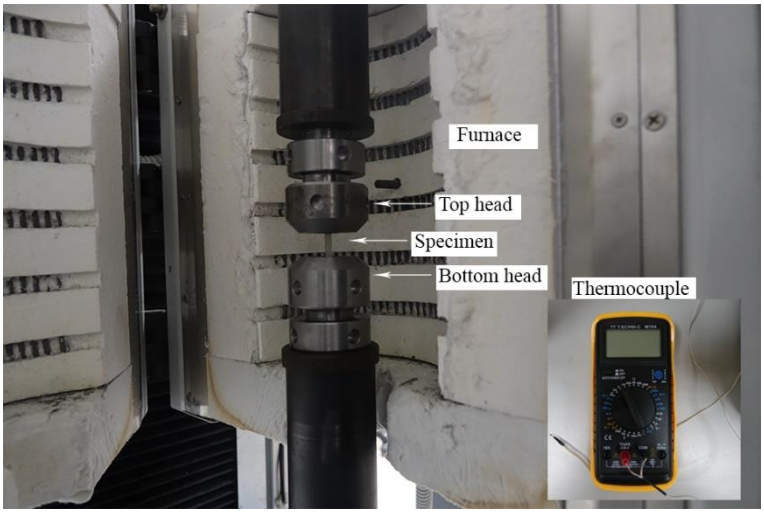

Figure 3.6. The elevated temperature test set-up, furnace, specimen, and thermocouple

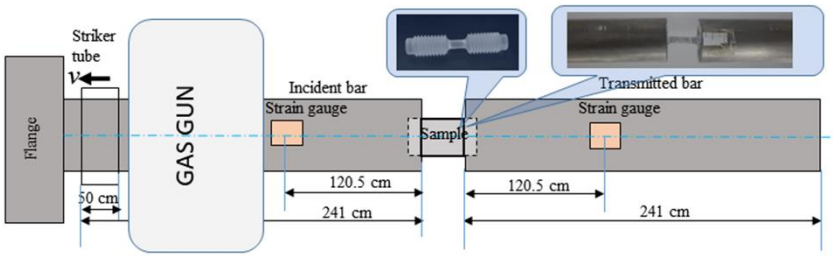

(a)

(cont. on next page)

Figure 3.7. The SHTB (a) schematic and dimension, (b) the picture and (c) typical SHTB waves measured by strain gages

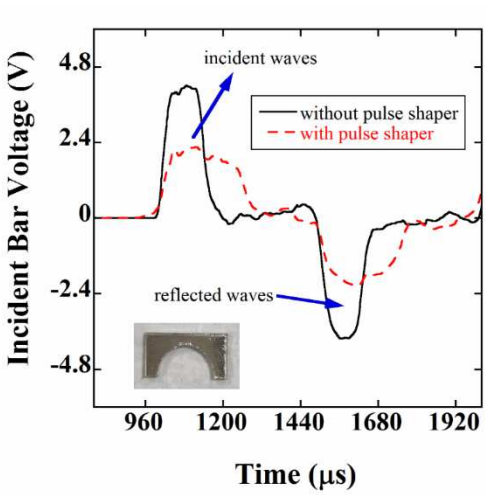

(b)

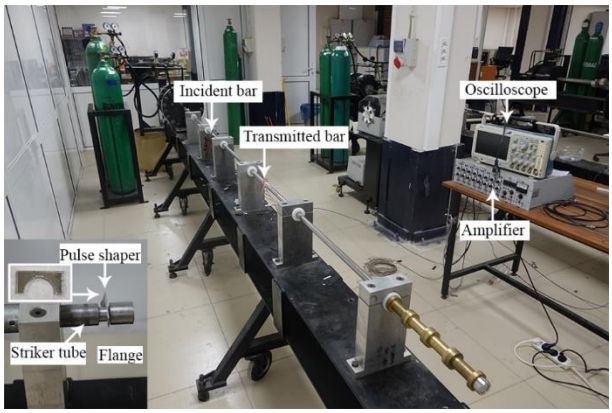

(c)

Figure 3.7.(cont.)

This requires a separate record of incident and reflected pulses. The use of pulse shaper however increases the time duration of the incident pulse, resulting in an interaction of the end of the incident pulse and the start of the reflected pulse. Strain gage 1 is placed on the incident bar to measure the incident and reflected pulse separately, as seen in Figure 3.8(a). In this case, the strain gage 1 reading is shifted in the time axis to the starting time of the transmitted pulse to make classical SHPB data reduction (Figure 3.8(c)). The QSI tests were performed in accord with the ASTM D6264 standard[93] in the Shimadzu Universal Testing Machine. A 16 mm-hemispherical tip indenter was used to indent the PC test plate at a crosshead speed of 6 mm s^{-1} (Figure 3.9). The QSI test specimens had a width of 100 mm and a length of 150 mm, in accord with the ASTM D7136[94] standard. In a typical test, the PC plate was placed on a steel support fixture and centered relative to the cut-out by the guide of the pins on the support fixture. The PC plate was fixed on the support fixture using four rubber-tipped clamps. The clamp tips were positioned approximately at the front side and back side of the PC plate. The picture of the QSI test set-up is shown in Figure 3.9(a). The low velocity impact tests were performed using a CEAST Fractovis Plus Drop Weight tester (Figure 3.9(b)). The total mass of the impactor with 16 mm-hemispherical tip was ~5.8 kg. A 16 mm-hemispherical tip indenter was the same as the indenter used in the QSI tests. The impactor hits the specimen at the velocity of 4.75 m s^{-1} and the energy level of ~66 J. The geometry of test specimen and the boundary conditions of low velocity impact test were in accordance with that of the QSI test. A Sony camera was used to record the deformation of QSI test sample.

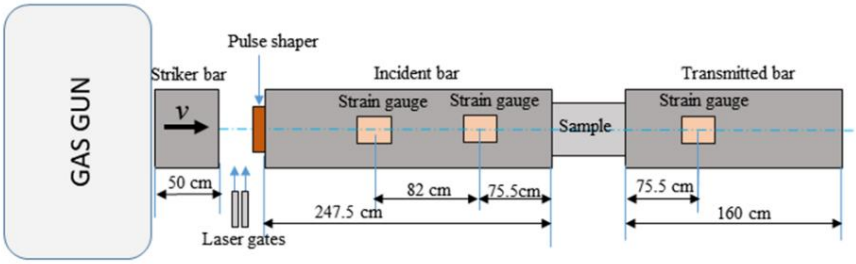

(a)

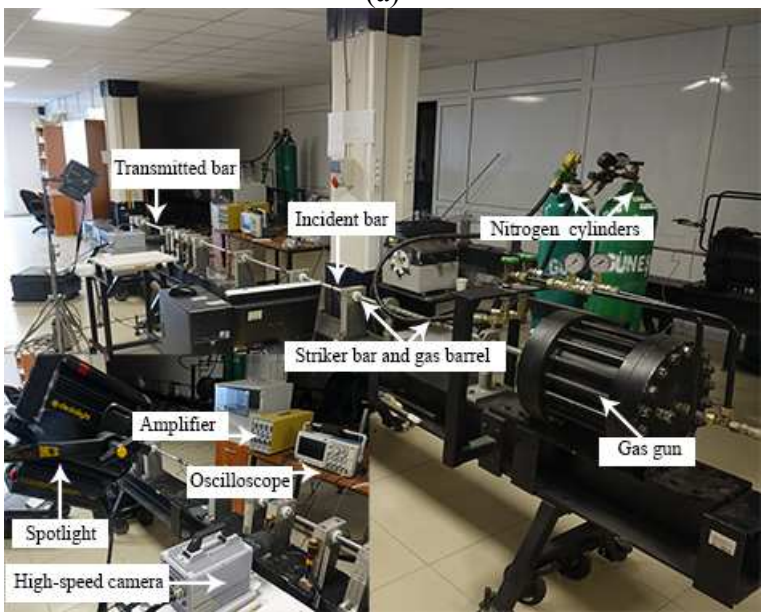

(b)

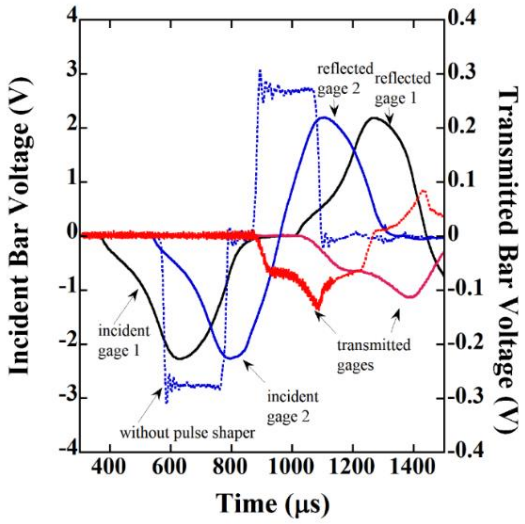

(c)

Figure 3.8. The SHPB (a) schematic and dimension, (b) the picture and (c) typical SHPB waves measured by strain gages with and without using a pulse shaper

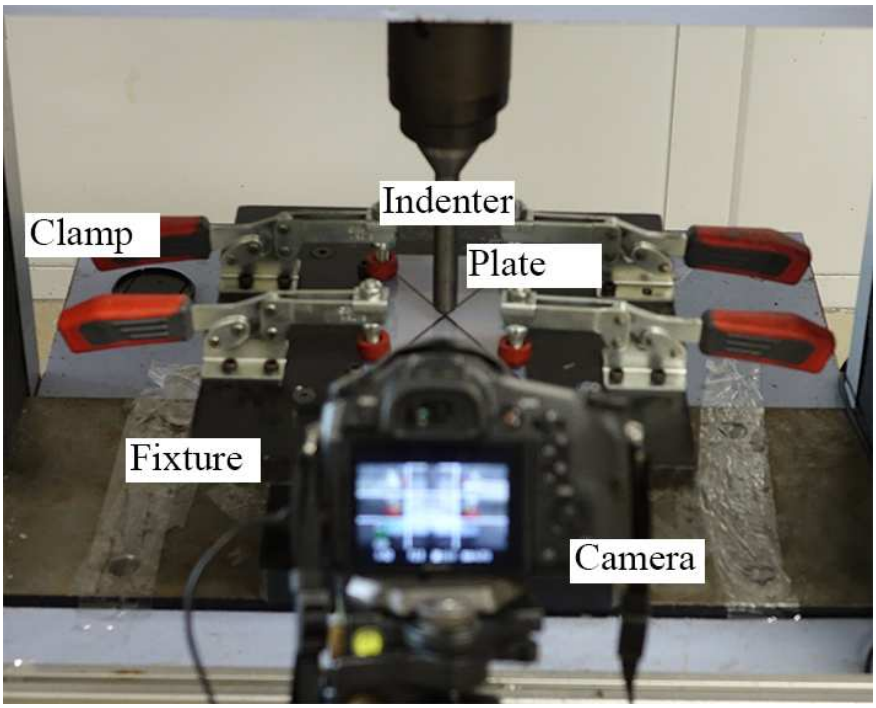

(a)

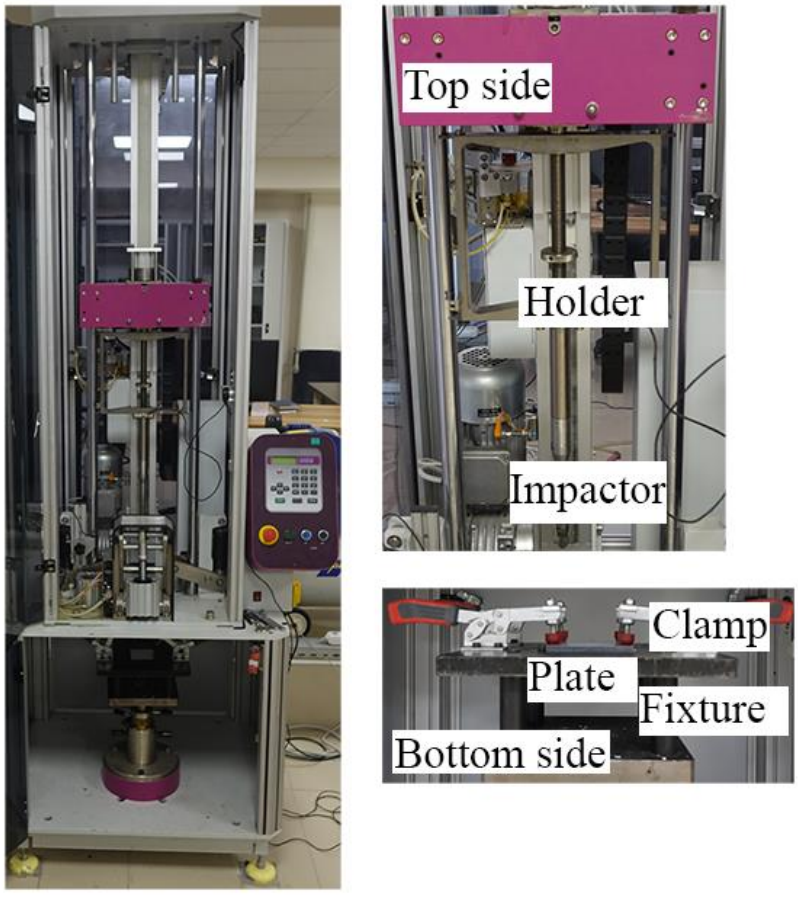

(b)

Figure 3.9. The QSI and LVI test set up

3.5. Projectile impact tests

Projectile impact tests were performed using a projectile gas gun test set-up shown in Figure 3.11. The test plate (200 x 200 mm) was inserted/fixed between two steel frames (square) having a thickness of 20 mm, an outer length of 400 mm and inner hole of 150 mm and the frames were tightened to fix the plate by using the bolts (Figure 3.11). A 30 mm- diameter steel ball was used as a projectile. In a typical test, the projectile is inserted inside a sabot (polyurethane foam). The sabot with the projectile is then inserted inside the barrel where it is fired by the release of the compressed air in the gas tanks. As soon as the sabot hits the holder at the entrance of the frame cabin, the projectile is released from the sabot and impinges onto target. The velocity of projectile before impacting target and after the perforation of target is measured using two velocity sensors located at the exit and entrance of the target frame. The PI tests were performed at the three different velocities: 100, 140 and 160 m s^{-1}. The maximum residual indentation depths in non-perforated PI specimens were measured by using a dial indicator. Finally, a high-speed FASTCAM camera was used to record the impact deformation and determine the projectile impact velocity. The recording was taken at 20,000 fps.

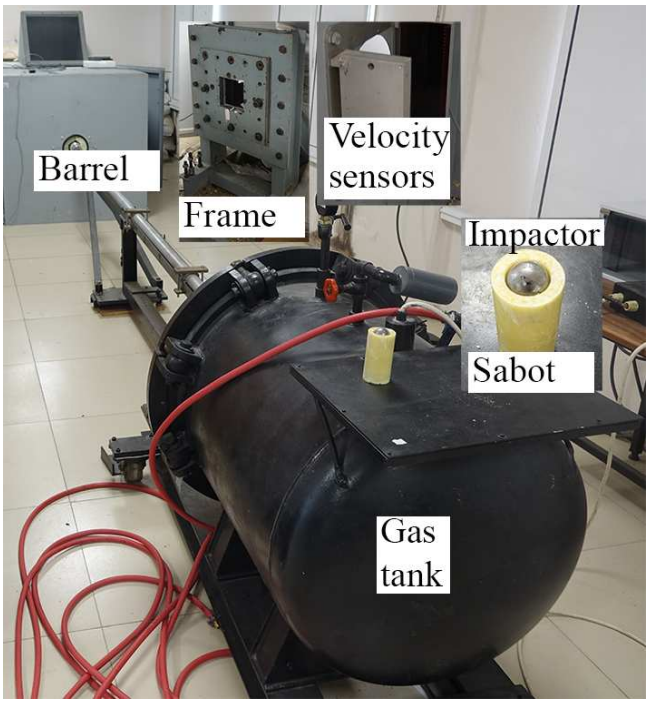

Figure 3.10. The PI test setup

CHAPTER 4

NUMERICAL MODELS

Chapter 4 contains all the numerical models used in the thesis. They can be listed as tension, notched tension, QSI, LVI, PI and bird strike models.

4.1. Test models

Three dimensional test models were developed in Solidworks and meshed in Hypermesh. The meshed geometries were then exported to LS-PrePost software to define the material model parameters, boundary conditions, contacts, test conditions, termination time and mass scaling (in case of quasi-static test modelling). The solution was performed in LS-Dyna Solver. The quasi-static tension (round and notched specimens), QSI, LVI, PI and the bird strike to a canopy were simulated.

The quasi-static tensile test model is shown in Figure 4.1. The numerical tensile test specimen had the same size as the experimental test specimen. The test specimen was modelled using 39,384 solid elements. The bottom and top sections where the grips hold the specimen were modelled using 15,606 single point constraint (SPC) nodes. The rotations and translations of the SPC nodes were fully constrained except the axial motion of the one of the ends (moving end, $u_x \neq 0$) in the loading axis as seen in Figure 4.1. The motion of the moving end was defined with PRESCRIBED_MOTION_SET in X direction with the same speed as the experiment.

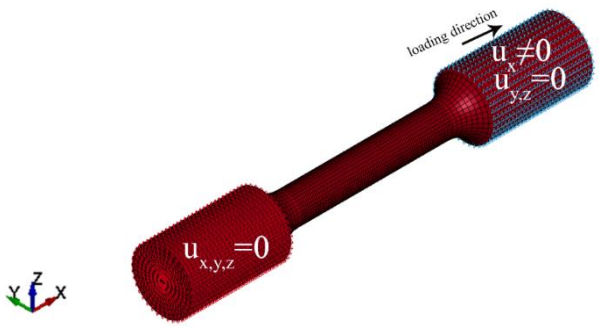

Figure 4.1. The quasi-static tension test model

Since the total CPU time for quasi-static test solutions are relatively long, a mass scaling was applied on the quasi-static tension models. The numerical model was initially run without mass scaling and the determined time step was multiplied by 10, 100 and 1000 to determine the mass scaling factor. It was found numerically that the kinetic energy change was substantially lower than the internal energy change when the mass scaling factor was 1000.

The tension test models were meshed using square elements. The use of square meshes avoids localized and unbiased damage progression in the simulations. A mesh sensitivity analysis was further performed. Three mesh sizes were implemented using 0.25 (coarse), 0.125 (medium) and 0.0625 (fine) mm mesh sizes (Figures 4.2(a-c)).

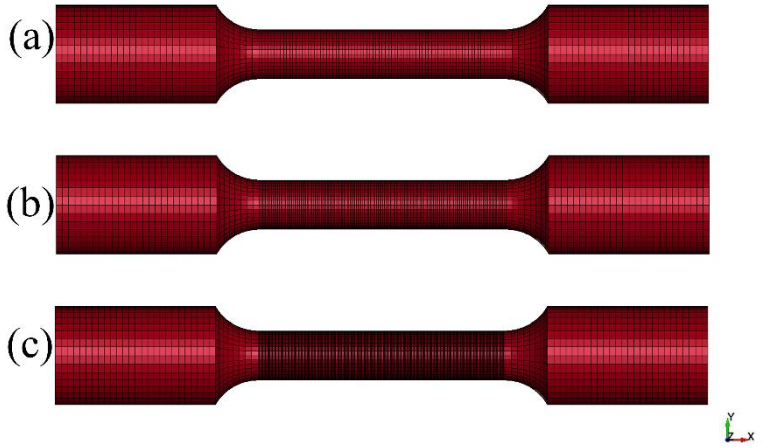

Figure 4.2. The mesh sensitivity analysis models of quasi-static tension test, (a) 0.25 mm (b) 0.125 and (c) 0.0625 mm mesh sizes

The quasi-static notched tension test models with 0.49 and 0.74 triaxialities are shown in Figures 4.3(a) and (b), respectively. The notched specimens with 0.49 and 0.74 triaxialities were modelled using 169,056 and 28,224 constant stress solid elements, respectively. The bottom and top sections were meshed with 19,494 SPC nodes. Except the moving end, the rotations and translations of the SPC nodes were fully constrained. The mesh sensitivity analysis was also performed for both triaxialities. For 0.49 stress triaxiality, the mesh sensitivity analysis was performed for the mesh sizes of 0.6, 0.3 and 0.15 mm (Figures 4.4(a-c)) and for 0.74 stress triaxiality for the mesh sizes of 0.8, 0.4 and 0.2 mm (Figures 4.4(d-f)).

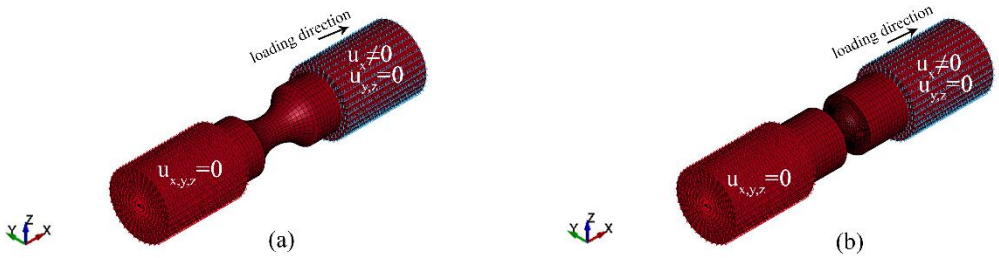

Figure 4.3. The quasi-static notched tension test models at the triaxiality value of (a) 0.49 and (b) 0.74

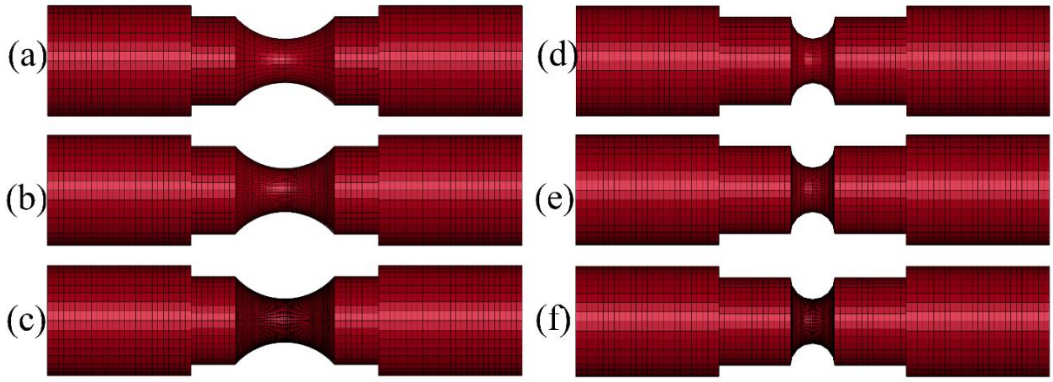

Figure 4.4. The quasi-static triaxiality tension test models at the triaxiality value of 0.49 (a) 0.6 mm (b) 0.3 mm and (c) 0.15 mm and the quasi-static triaxiality tension test models at the triaxiality value of 0.74 (d) 0.8 mm (e) 0.4 mm and (f) 0.2 mm mesh sizes

The QSI test model consists of an indenter, fixture, and PC plate as shown in Figures 4.5(a-d). The indenter, PC plate, and fixture were modelled using 13,828, 90,000, 206,400 constant stress solid elements, respectively. The clamps used to fix the test plate to the fixture in the experiments were modelled using fully constrained SPC nodes at the same locations with the experiments (Figure 4.5(a)). The velocity of the indenter (16 mm-diameter hemispherical tipped indenter) was the same as the experiments and defined by the INITIAL_VELOCITY_GENERATION card. The indenter was allowed to move along the Z-axis. The contacts in the specimen were defined by the AUTOMATIC_SINGLE_SURFACE to provide a better approximation of internal damages in the specimen. The contact between the indenter and PC plate was defined by the AUTOMATIC_SURFACE_TO_SURFACE.

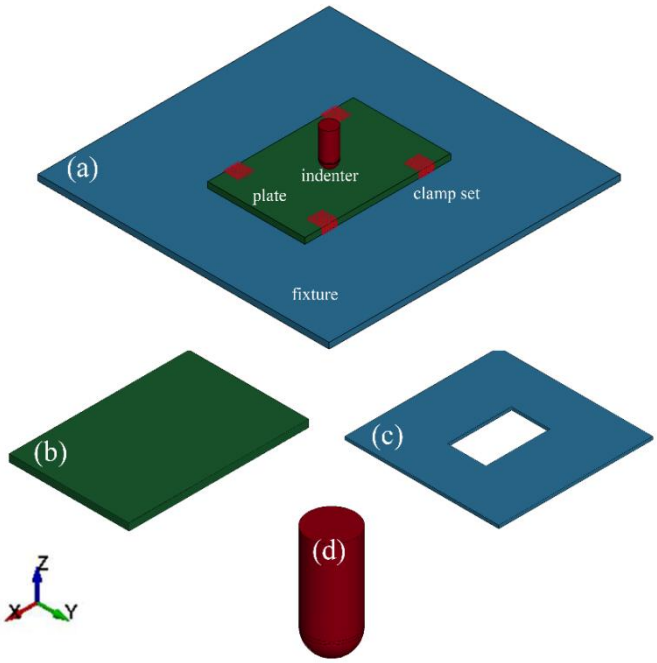

Figure 4.5. The quasi-static indentation test model (a)experimental setup, (b)100x150 mm PC test plate, (c) fixture and (d) indenter

The LVI test model consists of the impactor, fixture, and the PC plate (Figures 4.6(a-d)). The velocity of the 16 mm-diameter hemispherical tipped impactor was defined using VELOCITY_GENERATION card. The impactor was allowed to move freely along the Z-axis. The velocity of the LVI test was determined by the height of the impactor. The total weight of the impactor in the model was increased by increasing the density of the impactor to include total weight of the striker (impactor and additional mass) in the experiments. The clamps of the test specimen were modelled by preloading. Preloading was numerically determined with LOAD_RIGID_BODY card using 14 mm-diameter and 2 mm-thick cylinders as shown in Figure 4.6(e). The contacts in the specimen were defined by the AUTOMATIC_SINGLE_SURFACE. The contacts between the rigid cylinders and the PC plate were defined by the AUTOMATIC_SURFACE_TO_SURFACE and the contact between the impactor and the PC plate was defined by the ERODING_SURFACE_TO_SURFACE algorithm for penetration. The cylinders, PC plate, impactor, and fixture were modelled using 3072, 90,000, 103,164 and 206,400 constant stress solid elements, respectively. The mesh sensitivity analysis was implemented using 2, 1 and 0.5 mm mesh sizes (Figures 4.7(a-c)).

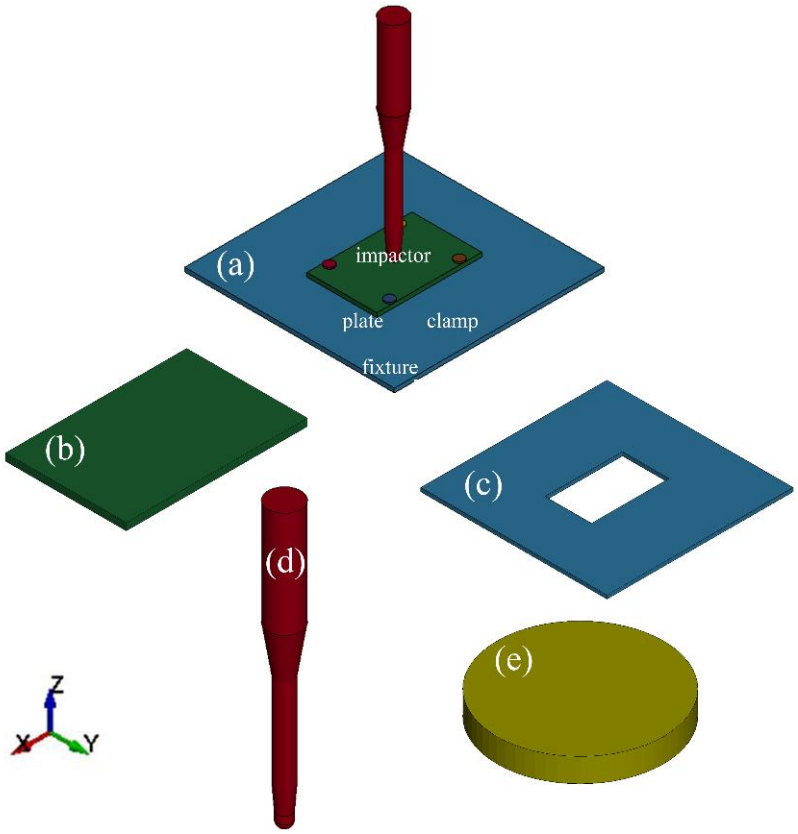

Figure 4.6. The LVI test model (a) experimental setup, (b) 100x150 mm PC plate, (c) fixture, (d) impactor, and (e) clamp

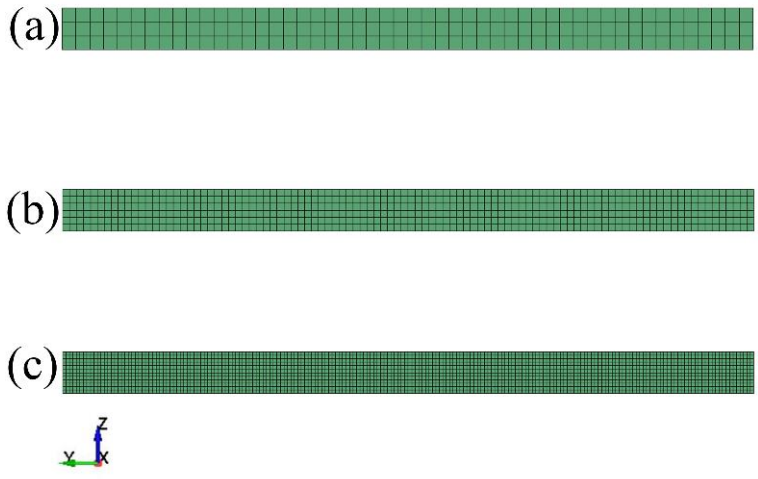

Figure 4.7. The mesh sensitivity analysis of the LVI test model (a) 2 mm, (b) 1 mm and (c) 0.5 mm mesh size models

The PI test model consists of the projectile, fixture, and the PC plate (Figures 4.8(a-d)). The velocity of the 30 mm-diameter sphere projectile was defined by the VELOCITY_GENERATION card without any constraints. The PC test plate was stabilized by using front and back fixtures as with the experiments. The PC plate, impactor, and fixtures were modelled using 22,464, 189,000, 240,000 constant stress solid elements, respectively. The contacts between plate and projectile in the PI models were defined by the ERODING_SURFACE_TO_SURFACE.

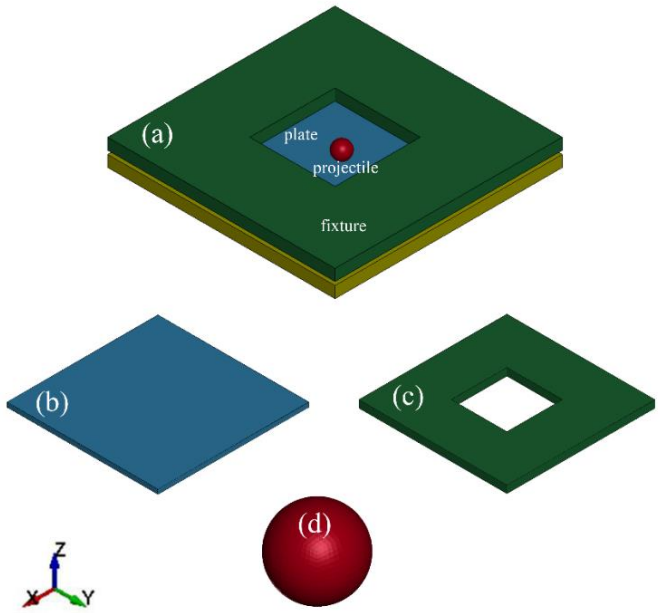

Figure 4.8. The projectile impact model (a) experimental setup (b) 200x200 mm^2 PC plate, (c) fixture and (d) projectile

The static and dynamic friction coefficients in the models were taken 0.3 and 0.2, respectively. The indenter, impactor, projectile, and fixture were modelled using MAT_020_RIGID material model card. The MAT_020_RIGID material model card parameters were as follows: the density=7800 kg m^{-3}, elastic modulus= 210 GPa, Poisson's ratio=0.33. The PC plate was modelled using the MAT_015_JOHNSON_COOK material model card. The material properties of the PC were as the followings: density=1200 kg m^{-3} [95], elastic modulus= 2.56 GPa (determined from the tension test at 10^{-3} s^{-1}), Poisson's ratio=0.39 (determined from the tension test at 10-3 s-1 from the strain-gaged test specimens), specific heat=1300 J kg^{-1} K^{-1} [68] and

the melting temperature= 538 K[95]. The equation of the state was defined by the Gruneisen equation with the following parameters: bulk sound speed=1933 m s^{-1}, the slope of the shock velocity vs. particle velocity curve= 2.65 and the Gruneisen gamma constant=0.61[96].

4.2. Bird strike model

The validation of the bird model is crucial in bird strike models. The substitute bird was modelled with Wilbeck's and the Welsh and Centonze's experiment models to verify the material properties of bird in the real-case scenario. The same material properties and geometry were used in both Wilbeck's and the Welsh and Centonze's experimental model. The substitute bird has a density of 950 kg m^{-3} and a porosity of 10%. That is, it is composed of 90% water and 10% air.

The bird was impacted on a rigid steel plate at the velocity of 116 m s^{-1} in the numerical model of Wilbeck's experiment. The peak and steady flow pressure values at the central point of impact region were determined. The rigid steel plate has 1x1 m cross-section and 51 mm thickness. The material model parameters of steel plates were as: the density= 7800 kg m^{-3}, elastic modulus= 210 GPa, Poisson's ratio=0.33. The rigid plate was modelled with 1200 Belytschko-Tsay shell elements, and 12.5x12.5 mm impact portion of plate was meshed with finer elements to accurately capture the pressure-time history (Figure 4.9). The data was taken from contact reaction forces between bird and steel plate. The force-time data alters the pressure-time data by dividing the contact reaction forces to cross-sectional area of the bird.

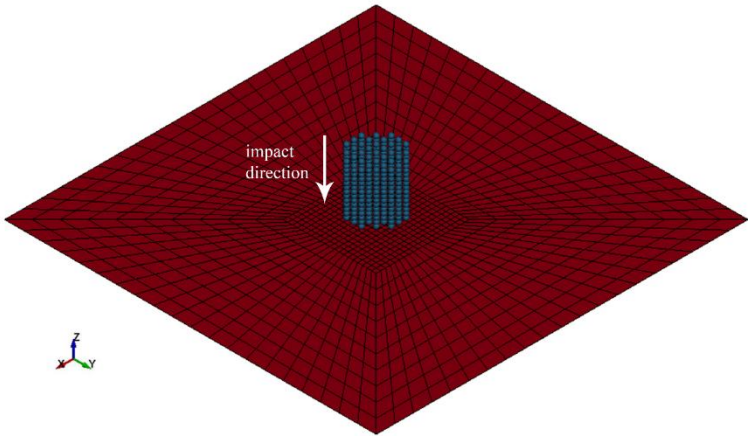

Figure 4.9. The numerical model of the Wilbeck's experiment model

The bird was impacted on a thin aluminum plate at a velocity of 146 m s^{-1} in the Welsh and Centonze's experiment model. The deflection of the aluminum plate was measured during the bird strike. The 6061-T6 aluminum plate was modeled using 50,000 constant stress solid elements, with a cross-section of 1x1 m and a thickness of 6.35 mm. The material model parameters of the 6061-T6 aluminum plate were taken from the literature[97]. The material model parameters of aluminum plate were as: the density= 2700 kg m^{-3}, elastic modulus= 69 GPa, Poisson's ratio=0.30, yield stress= 27.6 MPa. The PC plate had 10,000 elements at side and 5 through thickness elements (Figure 4.10).

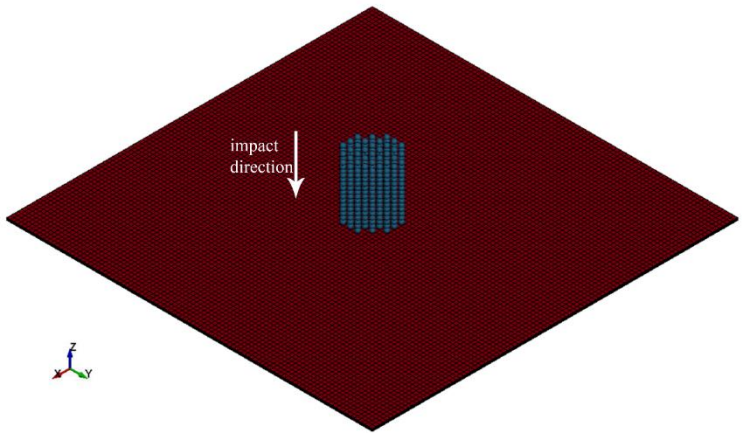

Figure 4.10. The numerical model of the Welsh and Centonze experiment

The bird strike model consists of a canopy and a bird with SPC nodes (Figure 4.11). The SPH bird model is a set of moving particles, each representing an interpolation point. Since the data is to be interpolated, the neighbor search algorithm plays the key role. The effect of each particle on its neighbors is formed inside a sphere of radius 2 h, known as support domain Ω_H. Here, 'h' is the smoothing length as shown in Figure 4.13. The smoothing length of every particle alters with time. The smoothing length of the bird model is tailored regarding arbitrary particle movements in the SPH computational method. There have to be enough particles in the neighborhood to validate a precise approximation of the numerical model. The JC material model was used to model canopy structure. The bird model was applied to a full-scale canopy model of an aerospace company after the validation of bird impact on rigid and deformable targets. Three impact velocities were specified as low (116 m s^{-1}), intermediate (140 m s^{-1}) and high (230 m s^{-1}), respectively. The PC canopy structure was modelled with 225,199 Belytschko-Tsay shell elements.

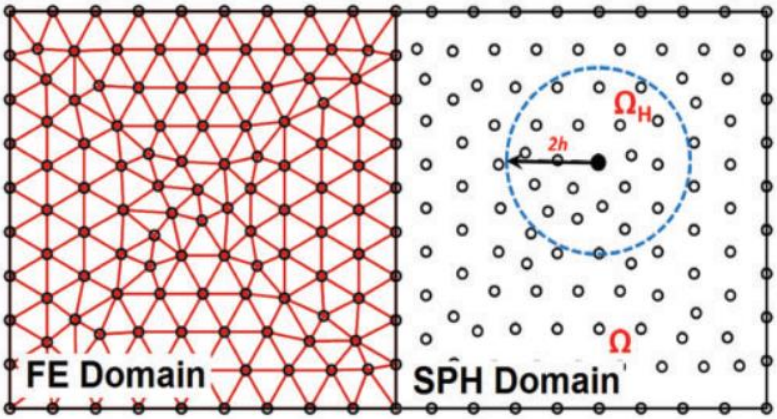

Figure 4.11. The comparison of (a) finite element and (b) SPH domains

The edges of the PC canopy structure were fully constrained. Besides, the PC canopy structure was modelled with thicknesses of 6 and 10 mm. The canopy was made with potential interface bow frames. The canopy had a length of 2500 mm, width of 1000 mm. The pilot's eye position and the two distinct regions of the canopy were located 35^o from the front view. Furthermore, the pilot's eye position and the bilateral point of the canopy were located 15^o from the left view. The position of the bird was tailored to align with the pilot's eye position. The SPH nodes were used to model the cylindrical bird with a diameter of 120 mm and a height of 140 mm. The MAT_010_ELASTO_PLASTIC_HYDRO material model card with EOS_GRUNIESEN EOS card was used to define material properties of bird. The MAT_010_ELASTO_PLASTIC_HYDRO material model card and EOS_GRUNIESEN EOS card were taken from the studies of Dar[70] and Cwiklak[76], respectively. The contact between bird and plates in the experiment models were defined with AUTOMATIC_NODES_TO_SURFACE without defining any friction coefficients. All the material properties are summarized in Table 4.1.

4.3. The Johnson-Cook flow stress and damage models

The used PC in the tests and canopy was modelled using MAT_015_JOHNSON_COOK material model. The MAT_015_JOHNSON_COOK material model card is based on the JC constitutive equation[59]. The JC constitutive equation depends on the strain ,strain rate and temperature. Besides, this equation is implemented into numerical models.

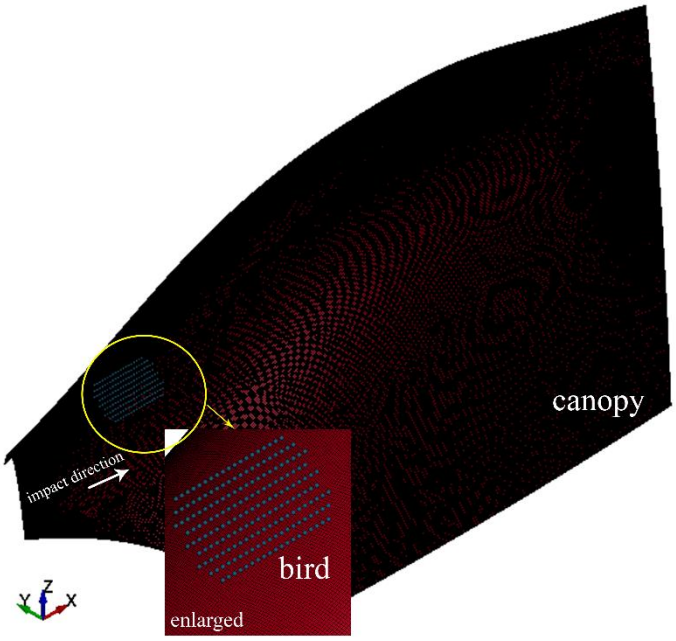

Figure 4.12. The numerical model of the bird strike on a canopy

Table 4.1. The material properties of bird

Mechanical Properties	
Density, ρ (kg m^{-3})	950
Shear Modulus, G (GPa)	2
Yield stress, σ_y (MPa)	0.02
Equation of state	
Bulk sound speed, C_0 (m s^{-1})	1438
Slope in Us versus Up diagram, S	1.92
Gruneisen gamma, γ	0.1

The JC constitutive equation includes both flow stress equation and failure equation. The flow stress incorporates with plastic strain, strain rate and temperature softening exponent in the flow stress model. The von Mises flow stress in the JC model, σ, expressed in Equation (4.1)

$$\sigma = [A + B\varepsilon_P^n]\left[1 + Cln\dot{\varepsilon}_P^*\right][1 - T^{*m}] \tag{4.1}$$

where A is the yield stress, B is the hardening coefficient, n is the hardening exponent, C strain rate sensitivity parameter m thermal softening exponent, ε_P is the equivalent plastic strain, ε_P^* is the strain rate ratio given as $\frac{\dot{\varepsilon_P}}{\dot{\varepsilon_0}}$ where $\dot{\varepsilon_P}$ is the equivalent plastic strain rate,

$\dot{\varepsilon_0}$ is the reference equivalent plastic strain rate , and T^m is the normalized temperature expressed in Equation (4.2)

$$T^* = \frac{T-T_r}{T_m-T_r} \tag{4.2}$$

where T, T_r and T_m are temperature, room temperature, melting temperature, respectively. The JC failure strain, ε_f, expressed in Equation (4.3)

$$\varepsilon_f = \left[D_1 + D_2 e^{D_3 \sigma^*}\right]\left[1 + D_4 ln\dot{\varepsilon_P^*}\right][1 + D_5 T^*] \tag{4.3}$$

where D_1 is the initial failure strain, D_2 is the exponential factor, D_3 is the triaxiality factor, D_4 strain rate factor, and D_5 is the temperature factor, respectively. σ^* is ratio of stress triaxiality, defined in Equation (4.4)

$$\sigma^* = \frac{\sigma_h}{\sigma_{eq}} = \frac{1}{3} + \ln\left(1 + \frac{a}{2R}\right) \tag{4.4}$$

where σ_{eq} is the von Mises equivalent stress and is given in Equation (4.5)

$$\sigma_{eq} = \sqrt{\frac{1}{2}(\sigma_1 - \sigma_2)^2 + (\sigma_2 - \sigma_3)^2 + (\sigma_1 - \sigma_3)^2} \tag{4.5}$$

and σ_h is the hydrostatic stress and given in Equation (4.6)

$$\sigma_h = \frac{\sigma_1+\sigma_2+\sigma_3}{3} \tag{4.6}$$

The quadratic form of strain rate sensitivity parameter proposed by HK[84] (2002) is given in Equation (4.7)

$$\sigma = [A + B\varepsilon_P^n]\left[1 + C_1 ln\dot{\varepsilon_P^*} + C_2\left(ln\dot{\varepsilon_P^*}\right)^2\right][1 - T^{*m}] \tag{4.7}$$

Three exponential forms of strain rate sensitivity parameters proposed by ARJ[85] (1997), CS[86] (1958), the nonlinear rate approach[87], respectively and listed as

$$\sigma = [A + B\varepsilon_P^n]\left[\dot{\varepsilon}_P^*\right]^{C_3}[1 - T^{*m}] \tag{4.8}$$

$$\sigma = [A + B\varepsilon_P^n]\left[1 + \left(\frac{\dot{\varepsilon}_P^*}{C_4}\right)^{\frac{1}{P}}\right][1 - T^{*m}] \tag{4.9}$$

$$\sigma = [A + B\varepsilon_P^n][(C_5 B\varepsilon_P^P)^{n'} ln\dot{\varepsilon}_P^*][1 - T^{*m}] \tag{4.10}$$

The material model card parameters are summarized in Table 4.2. The numerical and experimental approach used to determine the flow stress and damage models of the PC are summarized in Table 5.1, together with the determined parameters. Briefly, the experimental and numerical tension tests were used to determine both the flow stress and damage model parameters. The flow stress and damage model parameters were then calibrated by using the experimental and numerical force-displacement curves of the tension notched specimen. The SHTB test results were used to determine the damage parameter D_4.

The flow stress and damage rate sensitivity parameters were then determined by the experimental quasi-static and SHPB compression tests. A further calibration was made with the experimental and numerical QSI, DW and PI tests as shown in Figure 4.12.

4.4. Elastic-plastic-hydro model

The bird was modelled using the MAT_010_ELASTIC_PLASTIC_HYDRO material model. The MAT_010_ELASTIC_PLASTIC_HYDRO material model allows the modeling of an elastic-plastic hydrodynamic material and requires an EOS. The material model is used for modeling materials undergoing large strain during deformation such as bird. The plastic behavior of bird is defined with the yield stress and tangent modulus. Based on isotropic hardening principle, the yield strength σ_y is calculated by the following equation

$$\sigma_y = \sigma_0 + E_h\bar{\varepsilon}^P \tag{4.11}$$

Table 4.2. MAT_015_JOHNSON_COOK material model card parameters

Notation	LS-Dyna Notation	Parameter
ρ	RO	Density
G	G	Shear modulus
E	E	Young's modulus (shell elements only)
v	PR	Poisson's ratio
A	A	Yield stress
B	B	Strain hardening coefficient
n	N	Strain hardening exponent
C	C	Strain rate sensitivity
m	M	Thermal softening exponent
T_M	TM	Melting temperature
T_R	TR	Room temperature
c_P	CP	Specific heat
D_1	D1	Initial failure strain
D_2	D2	Exponential factor
D_3	D3	Triaxiality factor
D_4	D4	Strain rate factor
D_5	D5	Temperature factor
VP	VP	Formulation for rate effects
$RATEOP$	RATEOP	Optional forms of strain-rate forms
$C2/P$ $/XNP$	C2/P/XNP	Optional strain-rate parameter for Huh-Kang (C2) Cowper Symonds (P), Nonlinear rate approach (XNP)

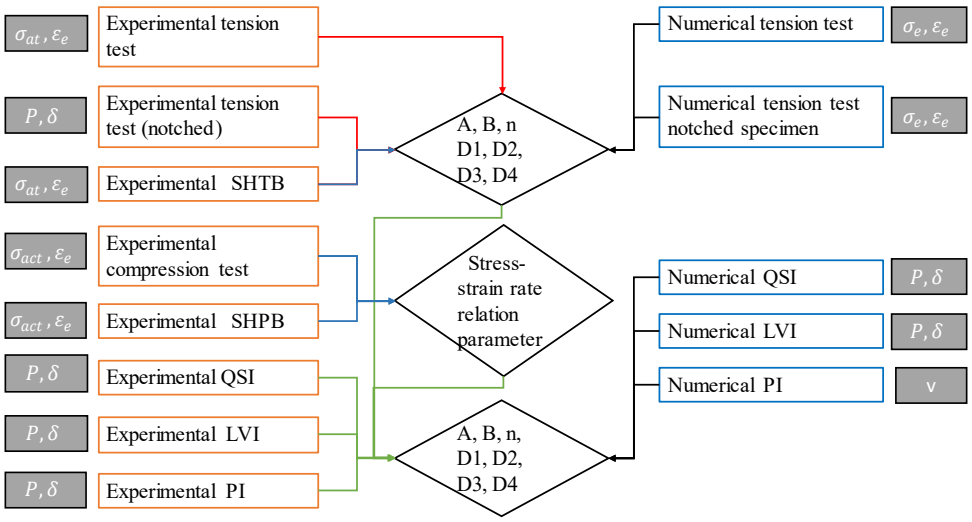

Figure 4.13. The numerical and experimental approach to determine the flow stress and damage model parameters

where $\bar{\varepsilon}^P$ is the effective plastic strain and E_h is the hardening modulus. The plasticity model is used in combination with Gruneisen EOS (*EOS_GRUNEISEN). EOS is based on the Hugoniot-jump theory. According to the Hugoniot-jump theory, when the impactor with an initial velocity, u_0 hits a surface, the material at the contact point is instantaneously brought to rest and a shock wave with the velocity u_s is generated. The orientation of this wave front is parallel to the surface and the running direction is perpendicular to the surface, propagating up the impactor body. A significant pressure gradient develops. This pressure gradient leads to an outward acceleration of the material particles and a release wave forms. The release wave causes a significant decrease in the pressure at the impact point. After several reflections of the release waves, the material flows steadily, leading to a constant pressure and velocity in the impactor. There have been mainly two types of EOS that were used in the numerical models. These EOS types can be listed as polynomial and Mie-Gruneisen. The Mie-Gruneisen EOS relates the change in pressure to the change in the corresponding specific internal energy. The EOS with shock velocity defines pressure for materials in compression gives in Equation (4.12)

$$P = \rho_0 C^2 \mu \left\{ \frac{\left[1+\left(1-\frac{\gamma_0}{2}\right)\mu-\frac{a}{2}\mu^2\right]}{\left[1-(S_1-1)\mu-S_2\frac{\mu^2}{\mu+1}-S_3\frac{\mu^3}{(\mu+1)}\right]^2} \right\} + (\gamma_0 + a\mu)E \qquad (4.12)$$

whereas for materials in tension gives in Equation (4.12)

$$P = \rho_0 C^2 \mu + (\gamma_0 + a\mu)E \qquad (4.13)$$

where C is bulk speed of sound; γ_0 is Grüneisen gamma; S_1 is linear coefficient; S_2 is quadratic coefficient; S_3 is cubic coefficient; a first order volume correction to γ_0; μ is volume parameter, expressed as $\mu = (\rho/\rho_0) - 1$; ρ is actual density; ρ_0 is initial density; and finally E is internal energy per unit of mass. The parameters of the MAT_010_ELASTIC_PLASTIC_HYDRO material model card are given in Table 4.3.

The nodes at edges were fully constrained. The bird was modelled as right cylinder and its SPH model consists of 555 nodes with lumped mass of 3.2613 g and the minimum distance between two nodes is approximately 10 mm. The Lagrangian modeling method is the standard approach for most structural finite element analyses.

Table 4.3. MAT_010_ELASTIC_PLASTIC_HYDRO material model card parameters

Notation	LS-Dyna Notation	Parameter
ρ	RO	Density
G	G	Shear modulus
σ_y	SIGY	Yield stress

. The nodes of the Lagrangian mesh are associated to the material and therefore each node of the mesh follows the material under motion and deformation. This approach is typically used for solid materials. The major problem of Lagrangian bird impactor models is the severe mesh deformations. Therefore, SPH modeling was chosen for bird model in the bird strike model.

4.5. Hardening exponent

The flow stress in JC flow stress equations is

$$\sigma = A + B\varepsilon^n \tag{4.13}$$

The load (P) is

$$P = \sigma A_s \tag{4.14}$$

where A_s is cross-sectional area of the specimen, The the derivative of Equation (4.14) at the necking is

$$\sigma dA_s + A_s d\sigma = 0 \tag{4.15}$$

Rearranging Equation (4.15) gives

$$\frac{d\sigma}{\sigma} = d\varepsilon \tag{4.16}$$

Rewriting $\sigma = A + B\varepsilon^n$ gives

$$\frac{d\varepsilon\left(nB\varepsilon^{(n-1)}\right)}{A+B\varepsilon^n} = d\varepsilon \tag{4.17}$$

Finally, we get

$$d\varepsilon\left(nB\varepsilon^{(n-1)}\right) = (A + B\varepsilon^n)d\varepsilon \tag{4.18}$$

The derivative of Equation (4.18) once again

$$d^2\varepsilon\left(nB\varepsilon^{(n-1)}\right) + d^2\varepsilon\left(n(n-1)B\varepsilon^{(n-2)}\right) = \left(nB\varepsilon^{(n-1)}\right)d^2\varepsilon + (A + B\varepsilon^n)d^2\varepsilon \tag{4.19}$$

The simplified form of Equation (4.19) is

$$n(n-1)B\varepsilon^{(n-2)} = (A + B\varepsilon^n) \tag{4.20}$$

The final equation is

$$\frac{n(n-1)}{\varepsilon^2} = \frac{A}{B\varepsilon^n} + 1 \tag{4.21}$$

CHAPTER 5

RESULTS AND DISCUSSION

Chapter 5 shows all the results and discussions regarding experiments and models

5.1. Tension and compression stress-strain behavior

Figure 5.1(a) shows the tensile engineering stress-engineering strain curves of three tests at 10^{-3} s^{-1}. As is seen in the same figure, the tests are repeatable, exhibiting almost similar flow stresses and failure strains. The stress-strain curves are further drawn in the elastic region together with the variation of the Poisson's ratio with strain and are shown in Figure 5.1(b). The quasi-static average elastic modulus of the tested PC is determined 2.56 GPa from the slopes of the engineering stress-engineering strain curves in the elastic region as depicted in Figure 5.1(b). The Poisson's ratios determined by the strain gage and DIC are also shown to be very similar in the same figure and found to be ~0.39 on average. Furthermore, the yield strength and yield strain are determined sequentially 51 MPa and 0.022 based on the 0.2% offset method at 10^{-3} s^{-1}. The tensile engineering stress-engineering strain curves at increasing quasi-static strain rates, 10^{-2} and 10^{-1} s^{-1} are further shown sequentially in Figures 5.1(c) and (d), respectively. The deformation pictures of the specimens tested at 10^{-3}, 10^{-2} and 10^{-1} s^{-1} at increasing strain levels and the fracture are shown in the insets of Figures 5.1(a), (c) and (d). At all quasi-static strain rates, the stress-strain curves depict typical cold drawing deformation, which is composed of an upper yield point after an elastic region, a following necking region and a final fully drawn region. At the beginning of the tensile deformation, the tested PC exhibits a viscoelastic behavior until the yielding at a strain of ~0.045, corresponding to the upper yield point. At the onset of the upper yield point, a neck region appears in the mid-sections of the specimens. This localized necking propagates along the test specimen until a strain of ~0.75 (Figure 5.1(a)). The propagation of necking along the gage length of the specimen is called cold drawing. After the completion of cold drawing (after 0.75 strain), the stress starts to increase. The point at which the neck propagation is completed and the stress starts to increase is called locking. The last region of the stress-strain curves

from locking to the fracture is known as the fully drawn region. In this region the cold drawn test specimen is pulled until the fracture strain. The representative engineering stress-engineering strain curves at 10^{-3}, 10^{-2} and 10^{-1} s^{-1} until the fracture and at relatively low strains are further shown in Figures 5.1(e) and (f), respectively. As is seen in Figure 5.1(f), the upper yield point of the tested PC increases as the strain rate increases from 10^{-3} to 10^{-1} s^{-1}. The upper yield points of three tests at 10^{-3} s^{-1} are 67.6, 68.1 and 67.1 MPa with an average value of 67.6 MPa. The upper yield points at 10^{-2} s^{-1} are 69.6, 67.9 and 68.6 MPa with an average value of 68.7 MPa and the upper yield points at 10^{-1} are 71.0, 69.9 and 68.6 MPa, with an average value of 69.8 MPa. The average true stresses and true strains were the calculated using the following relations $\sigma_{at} = \frac{P}{A}$ and $\varepsilon_{at} = \ln(\frac{a_0}{a})$ where A, a and $a_0$are the instantaneous area and diameter and initial diameter of specimen, respectively. The instantaneous diameter was determined from the pictures of the deforming specimens captured from the video records. The calculated typical average true stress-true plastic strain curve is shown in Figure 5.1(g), together with the true stress-true strain curve calculated using the constant volume assumption. The average true stress slightly increases with increasing strain in the necking region, while it increases more rapidly in the fully drawn region (the dotted lines in Figure 5.1(g)). The average true stress values in the fully drawn region are seen in the same figure are comparable with the true stress calculated using the constant volume assumption. The true stresses calculated using the constant volume assumption is further fitted with $[A + B\varepsilon_P^n]$ using A=51 MPa (yield strength). This fit gives B=176 MPa and n=2.12 (Figure 5.1(h)). The average true stresses are further fitted $[A + B\varepsilon_P^n]$ by taking the value of A=51 MPa as the yield strength. The fitting as shown in Figure 5.1(h) gives the similar values of B (165.8 MPa) and n (2.23). Figure 5.2(a) shows a typical SHTB incident and transmitted bar strain readings. The PC specimens in the SHTB tests did not fracture and were repeatedly reloaded by the stress waves reflected from the ends of the bars. The numbers in Figure 5.2(a) are the first and second loadings of a specimen in a SHTB test. The true stress-true strain curves of each loading cycle were then calculated until the fracture. The true stress-strain and true strain rate-strain curves of the repeatedly loaded three SHTB tests are shown in Figure 5.2(b). The stress and strain rate values for each test are comparable to each other by considering complex wave reflection in the HSR tension test. The specimens in the same figure are reloaded 6 times until the fracture. Figure 5.2(c) shows true stress-true strain.

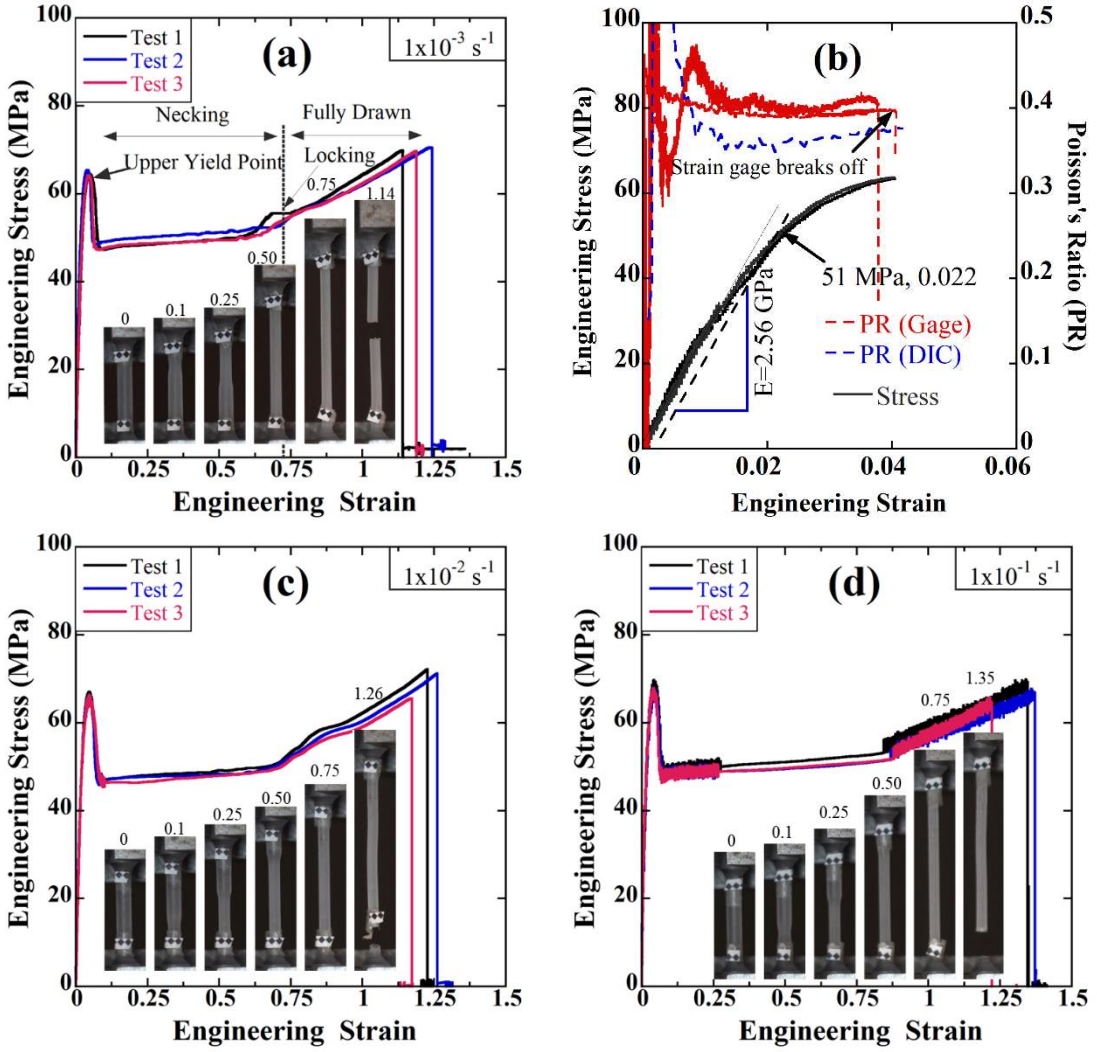

(cont. on next page)

Figure 5.1. (a) and (b) engineering stress- engineering strain curve at 10^{-3} s^{-1}, (c) at 10^{-2} s^{-1} and (d) at 10^{-1} s^{-1}, (e) and (f) engineering stress- engineering strain curve at 10^{-3},10^{-2} and 10^{-1} s^{-1}, (g) true stress-true plastic strain curves using measured diameter and constant volume assumption and (h) fitting the measured stresses with $A + B\varepsilon_P^n$

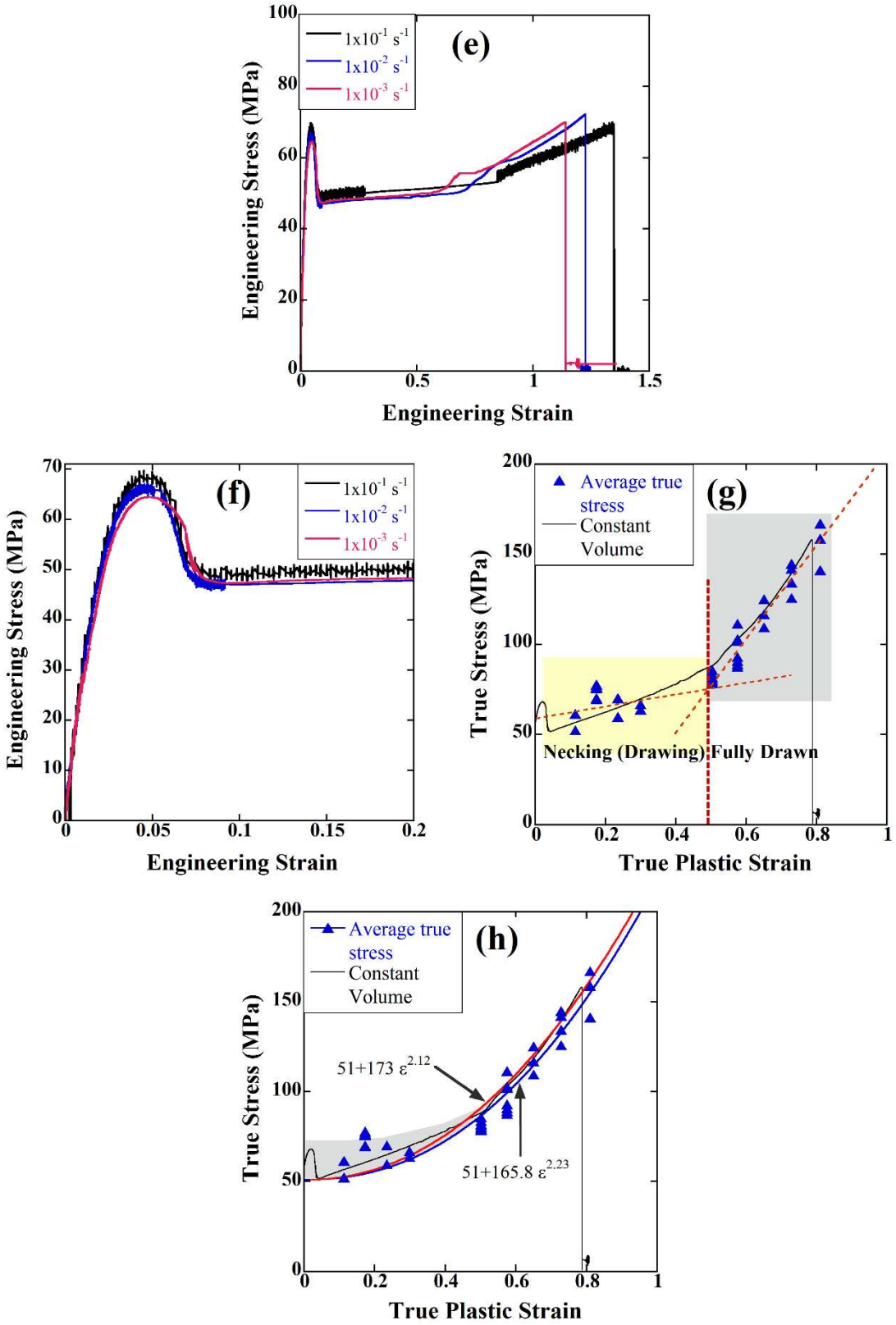

Figure 5.1. (cont.)

Besides, true strain rate-true strain curves determined from the strain gage of the SHTB and DIC. The curves seen in the same figure are very similar to each other, also proving the validity of the SHTB strain calculations. The deformation pictures of the specimen are also shown in the inset of Figure 5.2(c) at different strains. As is seen in the pictures, the strain is localized in the neck region and the specimen fractures in the neck region in the third loading. The specimen failure is ductile tearing as with the quasi-static tests. The DIC true fracture strain is also found to be very similar to the one calculated using the SHTB equations. Figure 5.2(d) shows the true stress-true strain and true strain rate-true strain curves of a SHTB test specimen together with the quasi-static (10^{-3} s^{-1}) true stress-true strain curve. The numbers in the same figure correspond again to the reloading (6 cycles). In the first loading, the maximum true strain rate ~1250 s^{-1} decreases to ~400 s^{-1} in the 6^{th} loading cycle. The rate sensitive flow stress behavior of the tested PC is also seen in Figure 5.2(d). The upper yield point increases from 67.6 MPa at 10^{-3} s^{-1} to 91 MPa at 1250 s^{-1}. This result should however be approached cautiously. Since, relatively shorter tension specimens were used in the SHTB tests to obtain large strains, the local strain rate in the tension test in the necking region is higher than that of the average strain rate. This makes it rather difficult to determine the strain rate sensitivity parameters using the tensile true stress-true strain curves. The deformation in compression tests was relatively homogeneous and the same specimen sizes were used both in the quasi-static and HSR tests. The strain rate sensitivity parameters were, therefore, extracted from the quasi-static and HSR compression tests. Figures 5.3(a), (b), (c) and (d) show three compressive engineering stress-engineering strain curves at the strain rates of 10^{-3}, 10^{-2}, 10^{-1} and 1 s^{-1}, respectively. The deformation pictures of the tested specimen at increasing strains are further shown in the inset of Figures 5.3(a-c). As with the tension tests, the compression tests are also repeatable and the specimens are deformed until about large strains (over 1) without fracture. The quasi-static compression tests also exhibit a rate sensitive flow stress behavior as depicted in Figure 5.3(d). The average upper yield points are 66.5 MPa (66.9, 66.4 and 66.1 MPa), 69.5 MPa (69.5, 69.6 and 69.3 MPa), 73.2 MPa (72.9, 73.3 and 73.4 MPa) and 80.73 MPa (80.83, 80.84 and 81.5 MPa) at 10^{-3}, 10^{-2}, 10^{-1} and 1 s^{-1} respectively Typical strain readings of the incident and transmitted bars of a compression SHPB test specimen are shown in Figure 5.4(a). The specimen shown in the same figure is deformed until about 0.14 strain.

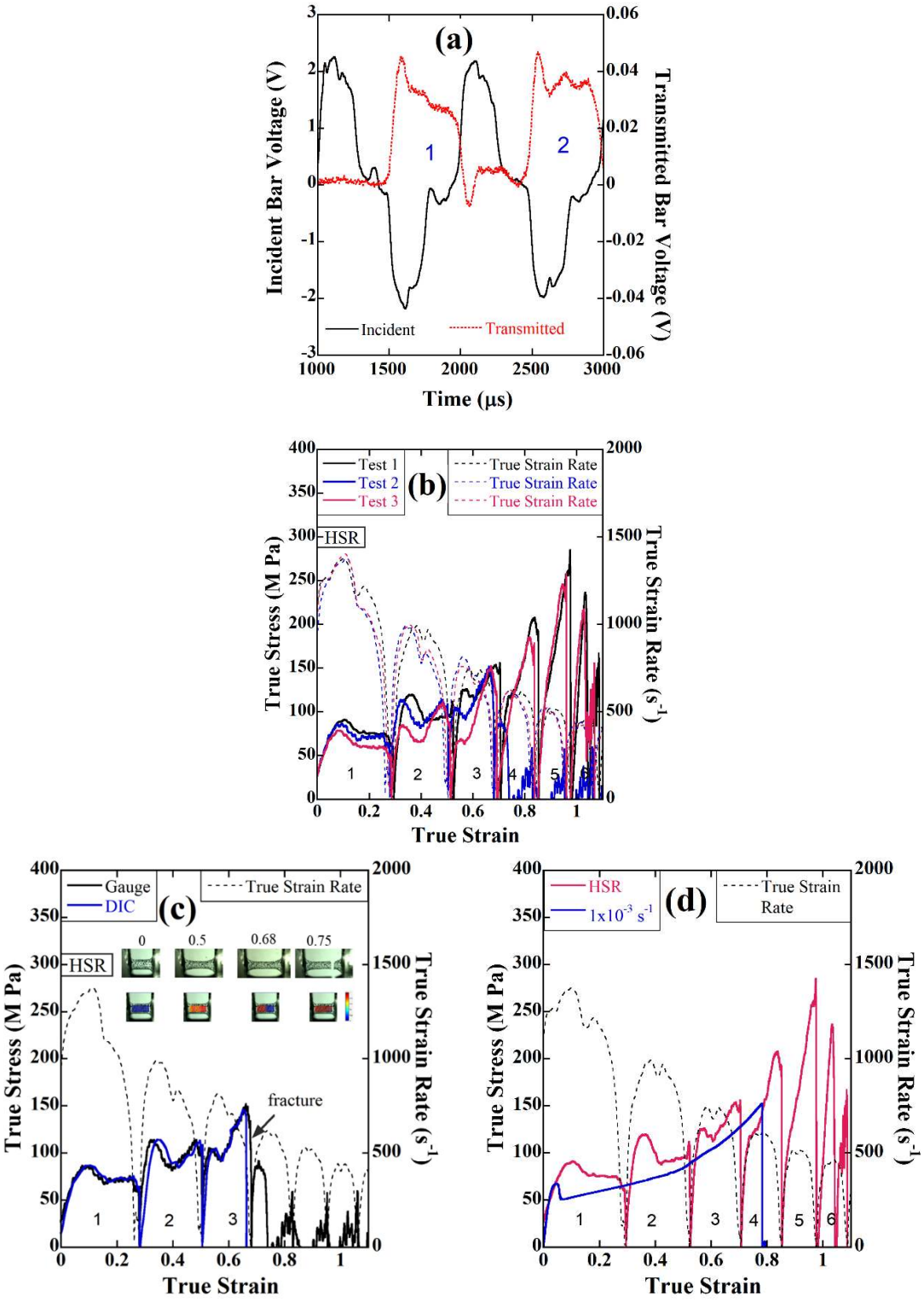

Figure 5.2. (a) SHTB repeated-loading bar response, (b) HSR true stress-true strain curves, (c) HSR test with gage and DIC measurement and (d) HSR and $1x10^{-3}$ s^{-1} true stress-true plastic strain curves and true strain rate variation in the HSR test

The true stress-true strain curves of three tests of compression SHPB tests at the average strain rates of 450, 1300, 2700 and 4500 s^{-1} are shown sequentially in Figures 5.4(c-e). The average upper yield points at these strain rates are sequentially of this strain rate is 94.5 MPa. (94.0, 100.8 and 88.8 MPa), 103.4 MPa (97.8, 102.2 and 101.1 MPa), 104.4 MPa (107.6, 102.6 and 103.1 MPa) and 107.0 MPa (110.6, 104.9 and 105.6 MPa). These values are greater than those of the quasi-static strain rates, 66.5, 69.5, 73.2 and 80.73 MPa at 10^{-3}, 10^{-2}, 10^{-1} and 1 s^{-1}, respectively.

The representative true stress-true strain curves and representative true strain rate-true strain curves at different average strain rates are shown in Figure 5.4(f). The average true strain rate was determined as the maximum true strain rate in the tests (the lines in Figure 5.4(f) show the level of true strain rate: 450, 1300, 2700 and 4500 s^{-1}). The compressive true stress-true strain curves at different true strain rates including the quasi-static true strain rates are further shown in Figures 5.4(g) and (h). As with the tension test, increasing the true strain rate from quasi-static to HSRs increases the flow stress of the compression test specimens (Figures 5.4(g) and (h)). The SHPB tests that performed at the strain rate of 450 s^{-1} and 1300 s^{-1} did not exhibit the strain softening region and the strain hardening region, respectively. The specimens were only loaded to a strain of ~0.06 and ~0.25 at 450 s^{-1} and 1300 s^{-1}, respectively. Furthermore, specimens did not fracture until about large strains in the compression SHPB tests.

5.2. Rate sensitivity and experimental damage parameters

Figures 5.5(a-e) show the compression initial peak strength variation with the logarithm of the plastic strain rate and the fitted parameters of the JC, HK, ARJ, CS and NLA stress-strain rate relations, respectively. The peak stress values in the same figures were fitted with the Quasi-static (QS) peak stresses (10^{-3}, 10^{-2}, 10^{-1} and 1 s^{-1}) and Quasi-static+Dynamic peaks stress (QSDYNA). The fitted parameters of the above flow stress relations are shown in Figures 5.5(a-e). The following values of the parameters are determined from the fitting QS peak stresses: C=0.022, C1=0.017 and C2=0.0011, C3=0.021, C4=2.07 and P=1.49, C5=0.12 and n'=0.90 for JC, HK, ARJ, CS and NLA, respectively. The determined the parameters after witting with QSDYN peak stresses are as follows: C=0.037, C1=0.02 and C2=0.0012, C3=0.030, C4=90081 and P=6.33, C5=0.028 and n'=0.038 for JC, HK, ARJ, CS and NLA, respectively.

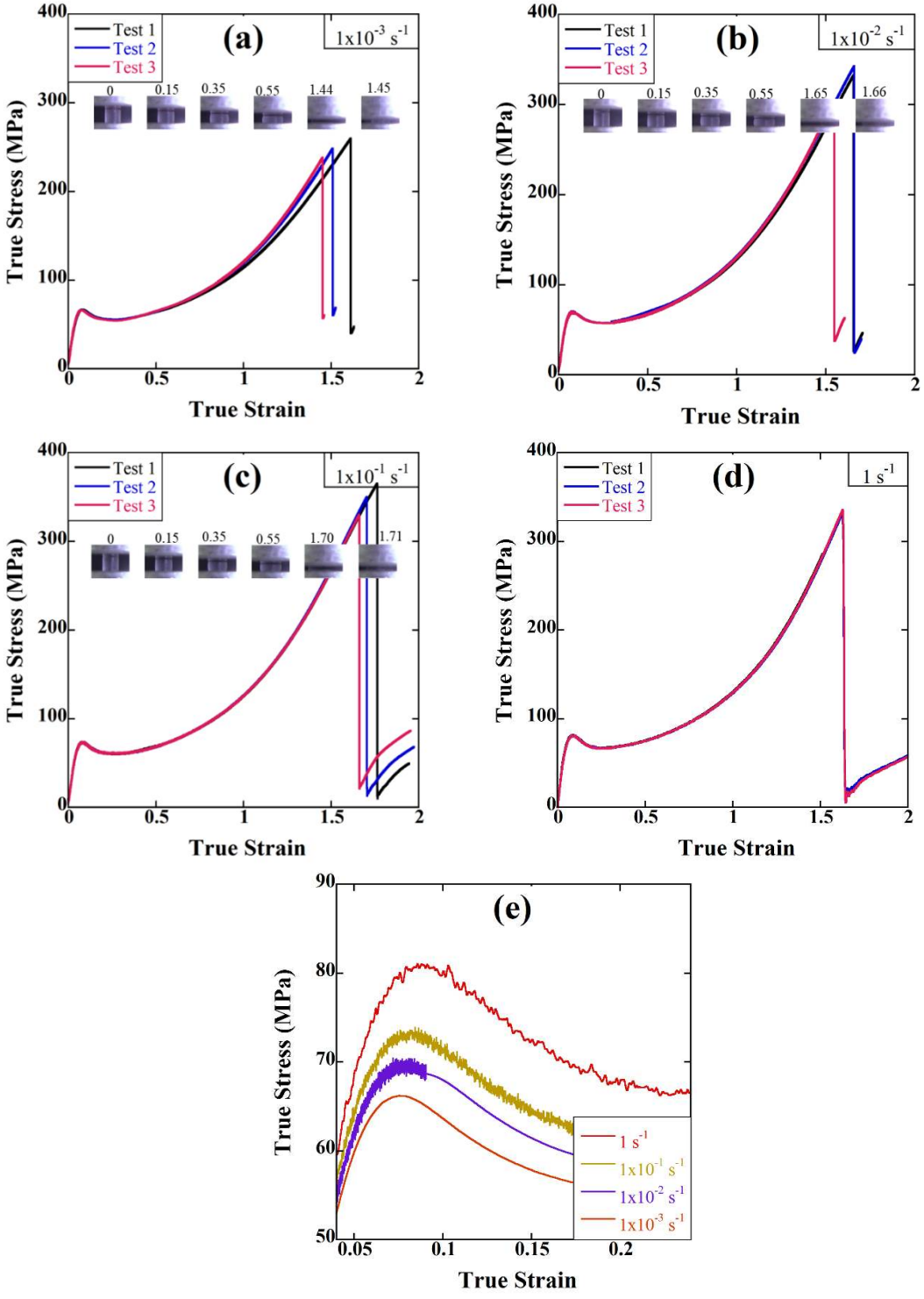

Figure 5.3. (a) engineering stress-engineering strain curve at the strain rate of 10^{-3} s^{-1} (b) engineering stress-engineering strain curve at the strain rate of 10^{-2} s^{-1} (c) engineering stress-engineering strain curve at the strain rate of 10^{-1} s^{-1}(d) 1 s^{-1} and (e) engineering stress-engineering strain curve at the strain rate of 10^{-3} ,10^{-2}, 10^{-1} and 1 s^{-1} (1 test)

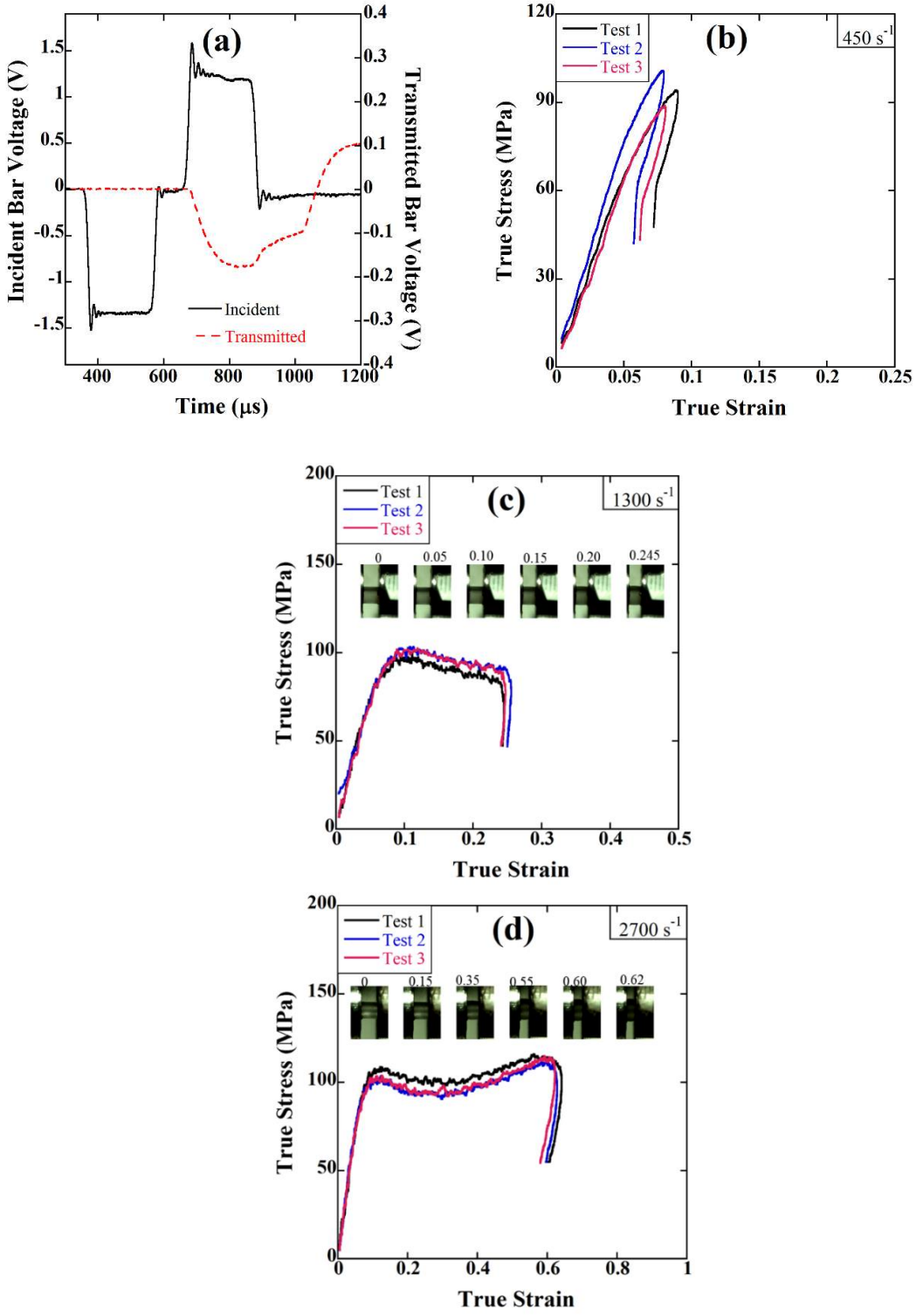

(cont. on next page)

Figure 5.4. (a) SHPB test strain gage reading, (b) true stress-strain curve at the strain rate of 450 s^{-1}, (c) 1300 s^{-1}, (d) 2700 s^{-1}, (e) 4500 s^{-1}, (f) true stress-true strain curve at the strain rate of 450 ,1300, 2700 and 4500 s^{-1}, (g) and (h) true stress-strain curve at the strain rate of 10^{-3},10^{-2}, 10^{-1}, 1, 450 ,1300, 2700 and 4500 s^{-1}

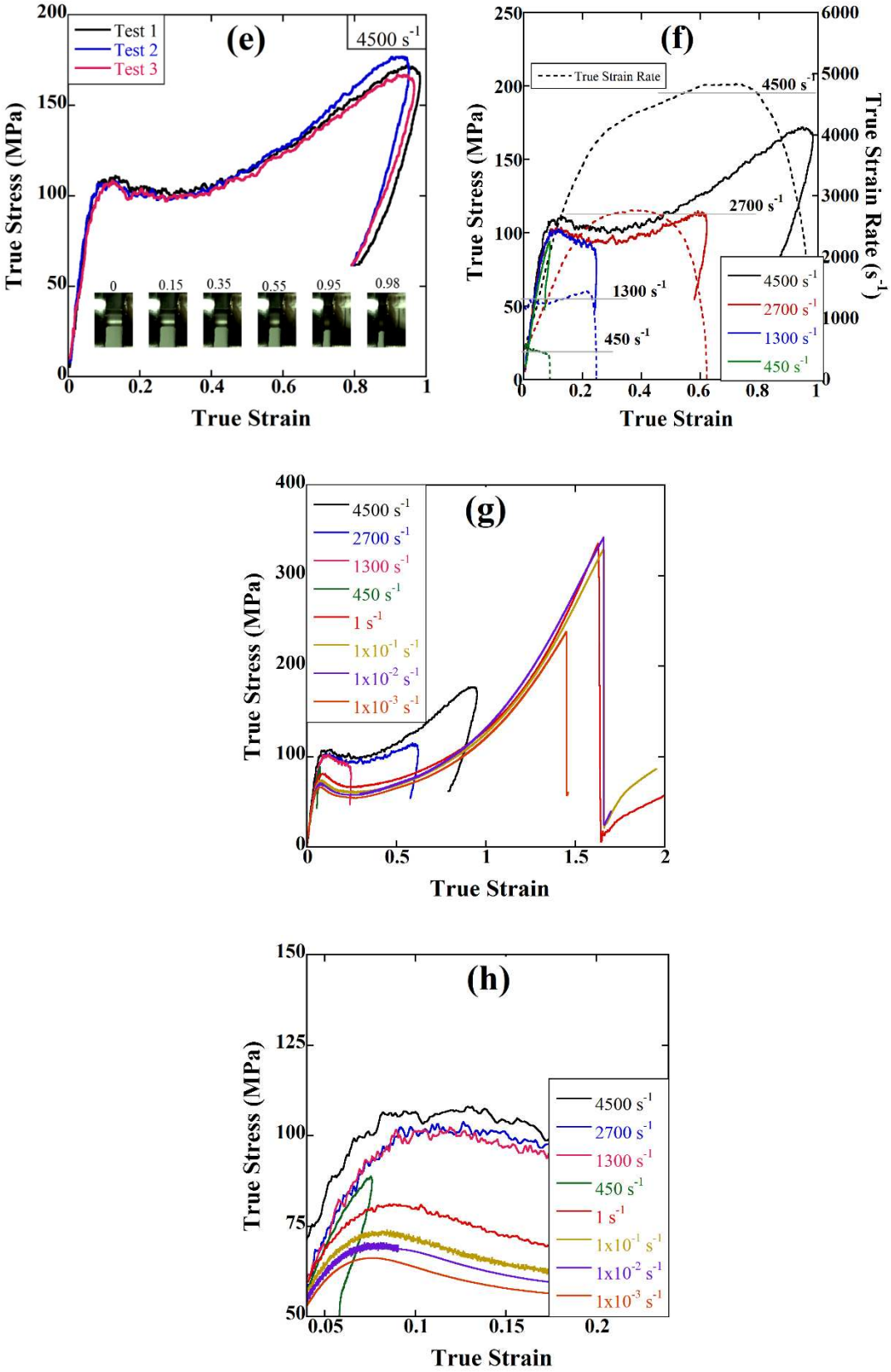

Figure 5.4. (cont)

All the relations more or less show similar trends of the compression peak stress with the strain rate within the studied strain rate regime. Furthermore, two different strain rate sensitivity regions as stated in the introduction are also seen in the tested PC, marked as 1 and 2 in Figure 5.5(f). The transition strain rate is determined by drawing straight lines to the data on the compressive strength-logarithm of the strain rate graph in the same figure. The critical strain rate is determined between 10 and 100 s^{-1}, respectively by excluding and including the compression strength at 1 s^{-1} (the data at 1 s^{-1} are in the transition range). The determined transition strain rate range agree well with the previous studies, for example 150 s^{-1} was reported in reference[3], 100 s^{-1} in reference[98] and 10 s^{-1} in reference[68]. A lower strain rate sensitivity at lower strain rates is governed by the α-transition (the restriction of the rotation and translation of the main chains) and a higher strain rate sensitivity at HSRs by the β-transition (the restriction of the main chain phenyl group) [17, 99] . The temperature of the α-transition was measured ~150°C and the β-transition ~-95°C at 3.2 x 10^{-3} s^{-1} [3].

The damage parameters D_1, D_2 and D_3 were extracted from the true plastic fracture strains of the round and notched tensile test specimens and the true plastic fracture strains of the compression test specimens (triaxiality is -0.33) at the quasi-static reference strain rate as shown in Figure 5.6(a). The damage parameter D_4 was determined using the true plastic fracture strains of the quasi-static (10^{-3}-10^{-1} s^{-1}) and dynamic round (500-1250 s^{-1}) tensile test specimens (triaxiality=0.33). From Figure 5.6(a), the following values of the damage parameters are extracted: D_1=0.75, D_2=0.060, D_3=-7.8. The value of D_4 is determined 0.025 from Figure 5.6(b).

As is noted in the same figure, the tested PC specimen is nearly notch insensitive in the tensile triaxiality region, while the tensile fracture strain increases as the strain rate increases from quasi-static to HSRs. The increased fracture strain with increasing strain rate is most likely due to the adiabatic heating of the specimens. The resultant experimental and numerical true plastic fracture strain versus stress triaxiality curves at 10^{-3}, at 10^{-2}, 10^{-1} and 1200 s^{-1} are shown in Figure 5.6(c).

The numerical fracture strains were determined using the fitted damage parameters of JC constitutive equation. These damage parameters are sorted as: D_1=0.75, D_2=0.060, D_3=-7.8 and D_4=0.025. It is seen in the same figure that the fitted fracture strain values can match the experimental fracture strains at all strain rates from quasi-static to HSR were investigated.

5.3. Rate sensitivity and experimental damage parameters

The experimentally determined flow stress equations using the constant volume and the average true stress-true strain curve shown in Figure 5.1(h) were further used to simulate the quasi-static tension test of the round specimen. Figure 5.7(a) shows the experimental force-displacement curve and the numerical force-displacement curve using the flow stress equation based on the constant volume and the damage parameters are listed in Figure 5.6(c). The flow stress equations using the constant volume results in much lower numerical force values and the displacement at fracture than the determined from the average true stress-true strain curve. After many iterations, it was found that the JC flow stress equation of $\sigma_y(MPa) = (72 + 720\varepsilon_P^{3.3})$ with a mesh size of 0.25 mm. The damage parameters of Figure 5.6(c) resulted in similar numerical force values and the displacement at fracture with the experiment as seen in Figure 5.7(a). The use of finer meshes has almost no effect on the force values in the necking region, while it decreases the force values in the fully drawn region. The experimental and 0.25, 0.125 and 0.0625 mm mesh numerical deformation pictures of the PC at the displacements corresponding to 1-6 in Figure 5.7(a) are shown in Figures 5.7(b-e), respectively. The diameters of the experimental and numerical test specimens were also determined at the displacements corresponding to 1-6 in Figure 5.7(a). Experimental specimen diameters for the displacements corresponding to 1-6 are sequentially 4, 3.33, 3.20, 3.06, 2.78 and 2.61 mm. The numerical 0.25 mm mesh specimen diameter are sequentially 4, 3.22, 3.12, 3.08, 2.79 and 2.73 mm. These values are 4, 3.43, 3.16, 3.05, 2.79 and 2.76 for 0.125 mm mesh model specimen and 4, 3.24,3, 2.91, 2.77 and 2.76 mm for 0.0625 mm mesh model specimen. As with the experiment, the numerical model test specimen is deformed by forming necking after the maximum force (numbered as 2 and shown by the arrows in Figure 5.7(b)). The necking progresses to the length of the specimen at the point 4 of Figure 5.7(a). The deformation then continues with the extension of the fully drawn specimen after the point 4 until fracture (the point 6). A further verification of fidelity of the flow stress and damage model parameters was made by comparing the numerical force-displacement curves of the notched specimens of $\sigma^* = 0.486$ (R=6), $\sigma^* = 0.739$ (R=2) with the experiments. The flow stress equation $(72 + 720\varepsilon_P^{3.3})$ and the damage parameters (D_1=0.75, D_2=0.060 and D_3=-7.8) over predicted the experimental force-displacement curves and the displacement at fracture of the notched tensile specimens.

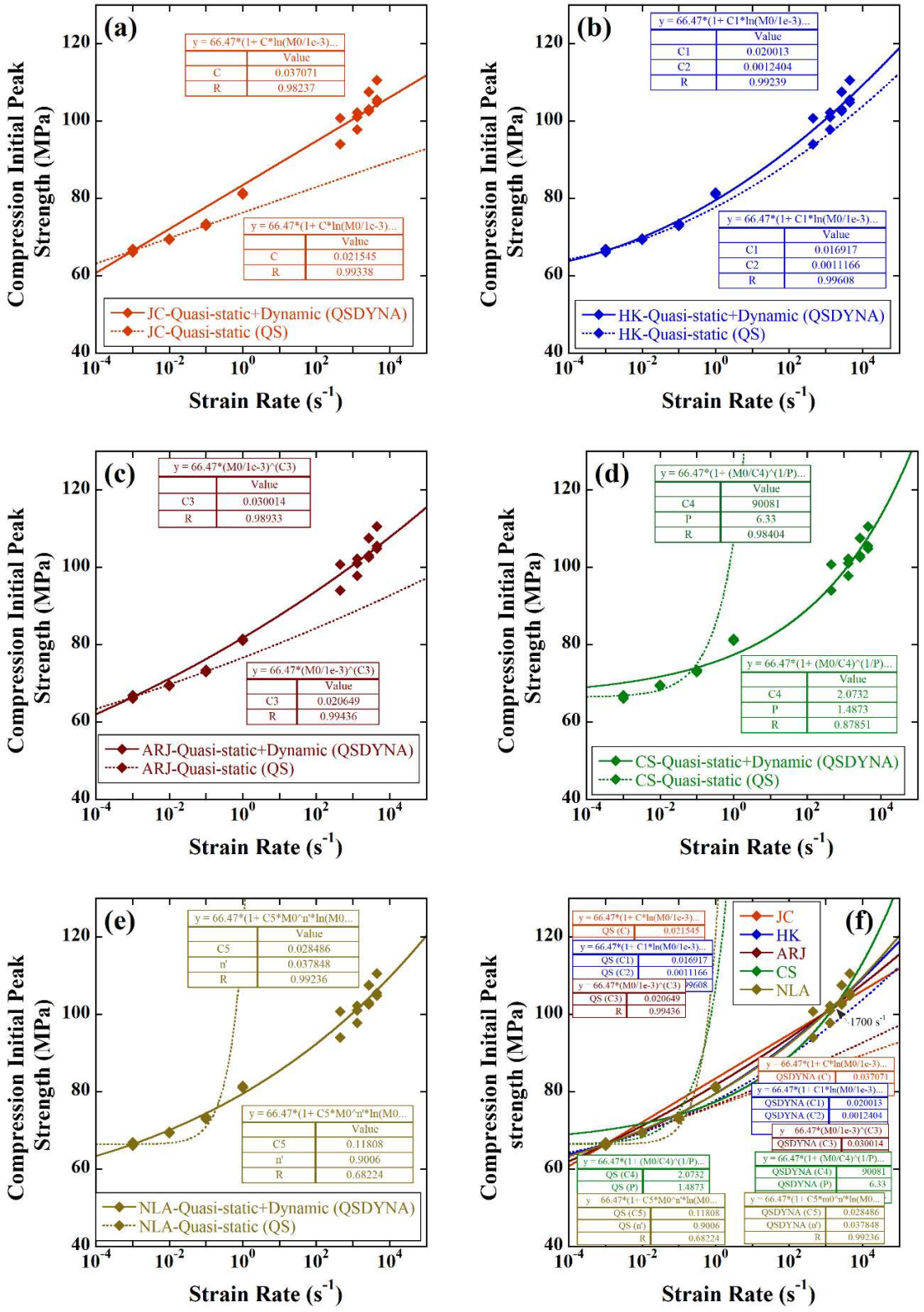

Figure 5.5. The compressive initial peak strength vs. strain rate graph showing two different strain rate sensitivity regions both QS and QSDYNA (a) JC, (b) HK, (c) ARJ, (d) CS (e) NLA and (f) all of them

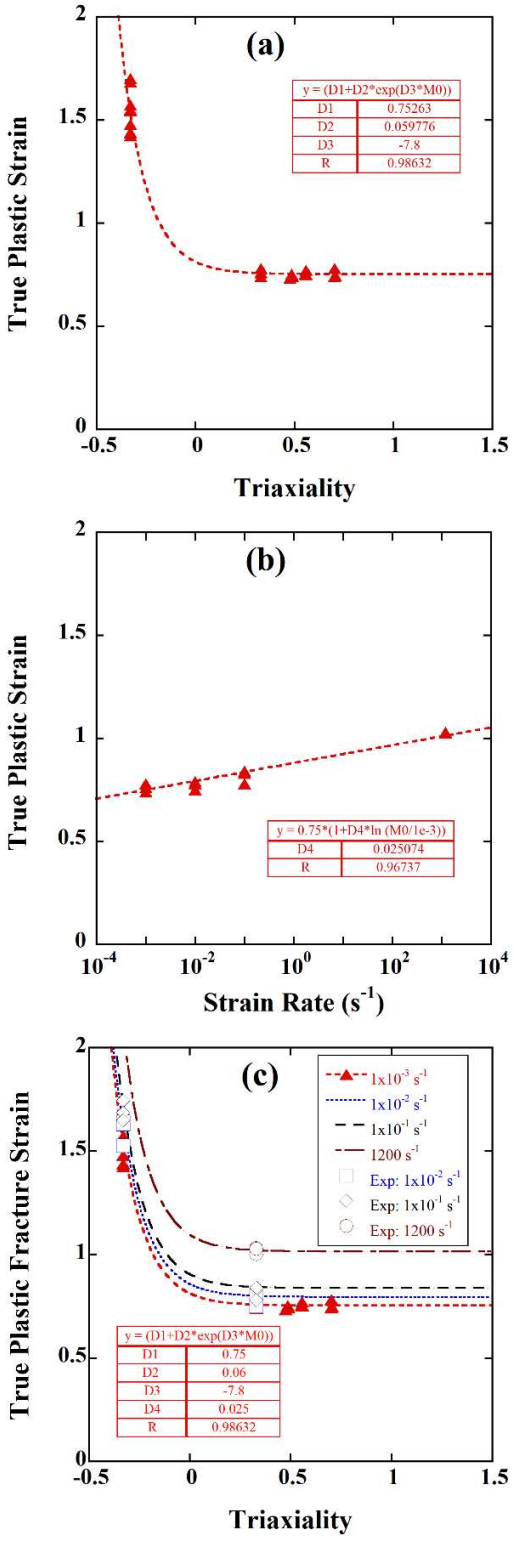

Figure 5.6. The damage parameters of JC (a) D_1 (initial failure strain), D_2 (exponential factor), D_3 (triaxiality factor) and (b) D_4 (strain rate factor) (c) the true plastic fracture strain-triaxiality curve at increasing strain rates of 10^{-3},10^{-2}, 10^{-1} and 1200 s^{-1}

In the fully drawn region, the determined flow stress equation and damage model parameters using the numerical notched tensile test specimens also give an effective stress-effective plastic strain curve having a better match with the average true stress-average strain than the flow stress equation and damage model parameters determined using the numerical round tensile test specimens as seen in Figure 5.7(f). The effective stress-effective plastic strain curve was determined from an element in the mid-section of the numerical test specimen. A fit to the effective stress-effective plastic strain curves of the numerical notched tensile test specimen gives a flow stress equation $\sigma_y(MPa) = (56 + 176\varepsilon_P^{2.67})$ which is very similar to the flow stress equation obtained from the average true stress-true strain curve $\sigma_y(MPa) = (51 + 173\varepsilon_P^{2.12})$, as seen in Figure 5.7(g). In the same figure, the fitting results of the compression average true stress-true strain curves are also shown, $\sigma_y(MPa) = (55 + 68\varepsilon_P^{2.64})$.

Note that at low strains, the true stress-true strain curves of the tension and compression are similar, but they differ significantly at increasing strains (Figure 5.7(g)). Boyce et al[8]. investigated and compared the stress-strain responses of the uniaxial tension and compression tests of a PC under constant extension rate. The obtained local true stress-true strain curve of the uniaxial tension test was also shown to be above the true stress-true strain curve of the compression test. The difference was ascribed to the increased local strain rates in the necking region of the tension test by a several order of magnitude higher than the average true strain rate. The strain hardening behavior of the specimens in the tension and compression is also different due to the difference in the molecular chain orientation[8]. A planar random molecular chain orientation is expected in the compression loading axis, while a uniaxial molecular chain orientation in the tensile loading axis. This leads to an anisotropy between the compression and tension behavior of PC[15]. Necking starts both experimentally and numerically at the center of the notched region and continues until the fracture. The experimental and numerical R=2 notched specimens (using 0.8, 0.4 and 0.2 mm meshes) exhibit similar deformation scheme with the R=6 specimens as seen in Figures 5.9(a), respectively.

A mesh size 0.2 mm well agrees with the experimental force-displacement curve as seen in the same figure. The necking region in these specimens is again pulled until the fracture. The deformation pictures of experimental and 0.8, 0.4 and 0.2 mm mesh numerical model specimens at different displacements are shown in Figures 5.9(b-e), respectively.

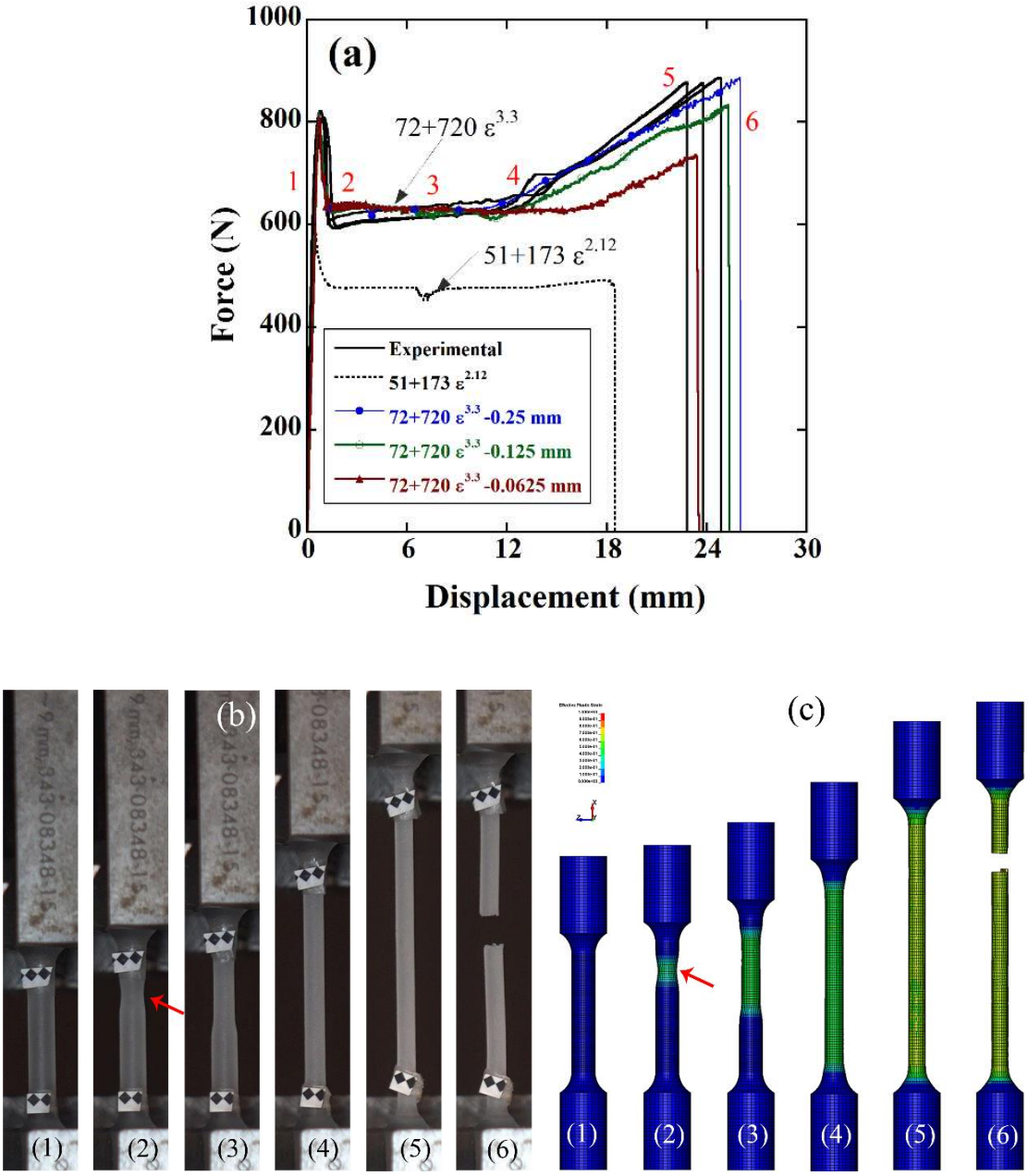

(cont. on next page)

Figure 5.7. The experimental and numerical force displacement curves of the (a) round at the strain rate of 10^{-3} s^{-1}, the deformation pictures of the round tensile PC specimens (b) experimental, numerical (c) 0.25 mm (d) 0.125 mm (e) 0.0625 mm mesh sizes (f) effective stress-effective plastic strain curves of the numerical models and (g) effective stress-effective plastic strain curves of the tension and compression tests

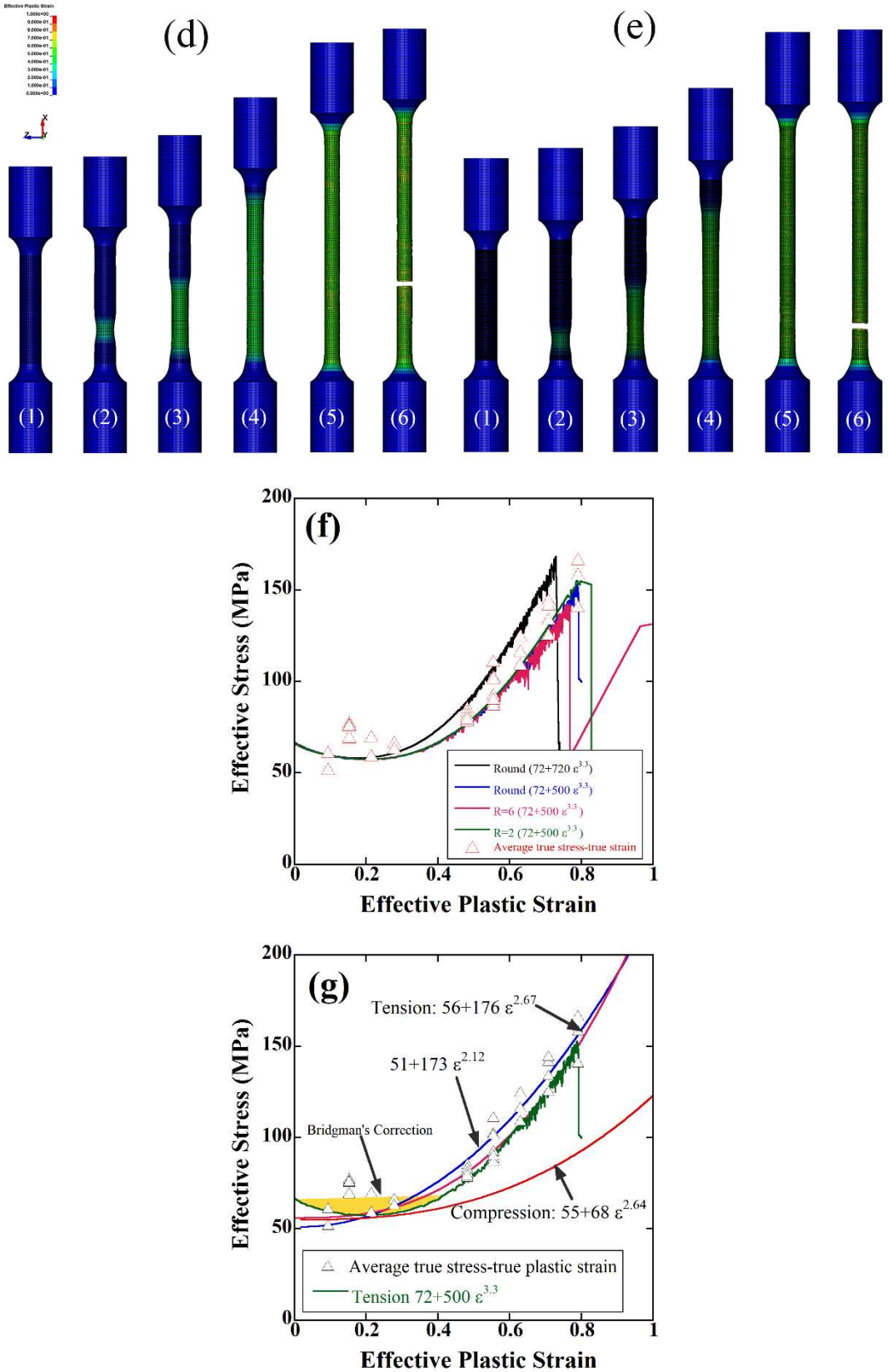

Figure 5.7. (cont.)

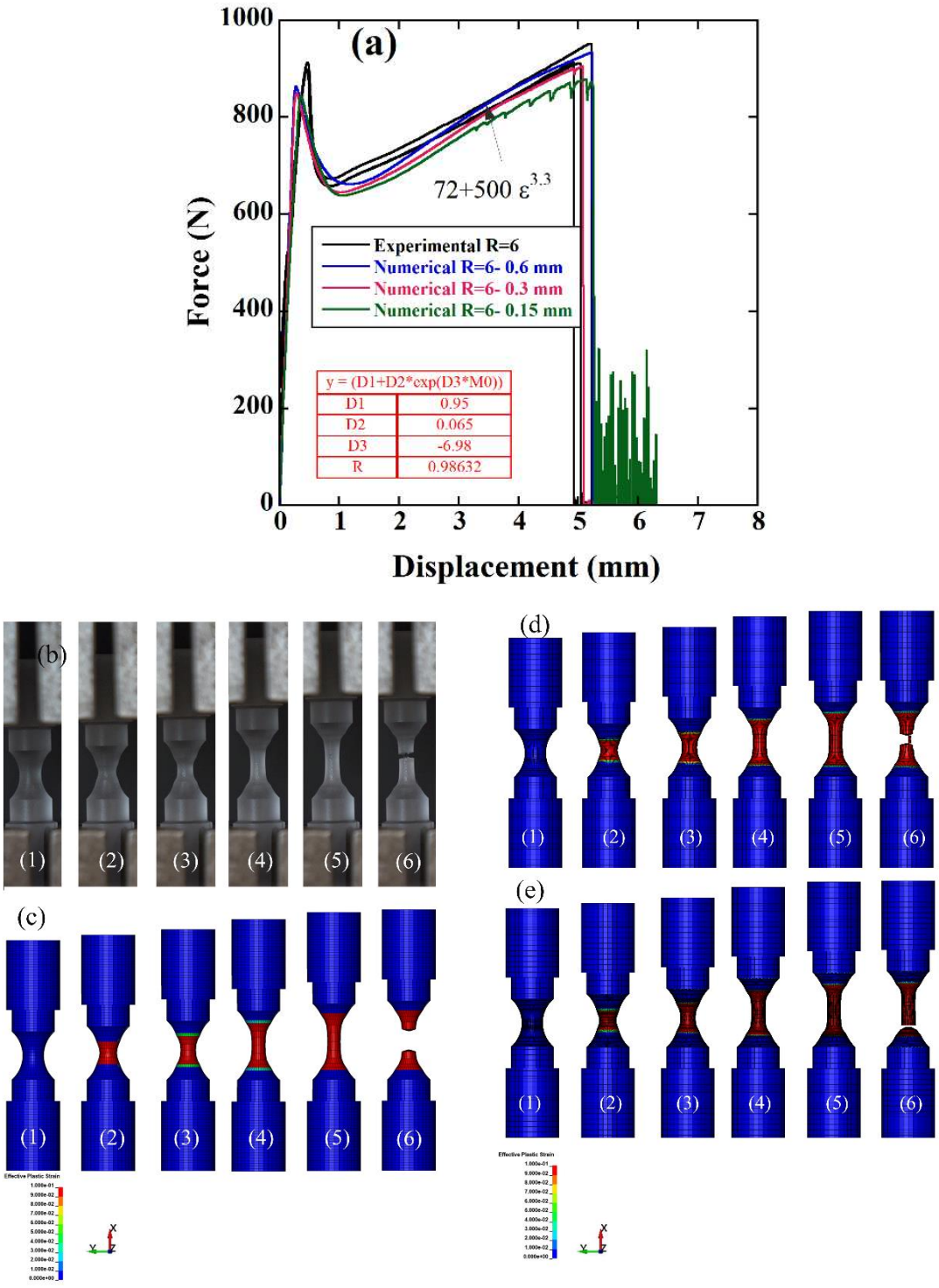

Figure 5.8. The experimental and numerical force displacement curves of the (a) notched R=6 at the strain rate of 10^{-3} s^{-1}, the deformation pictures of the notched tensile PC specimens R=6 (b) experimental, numerical (c) 0.6 mm (d) 0.3 mm (e) 0.15 mm mesh sizes

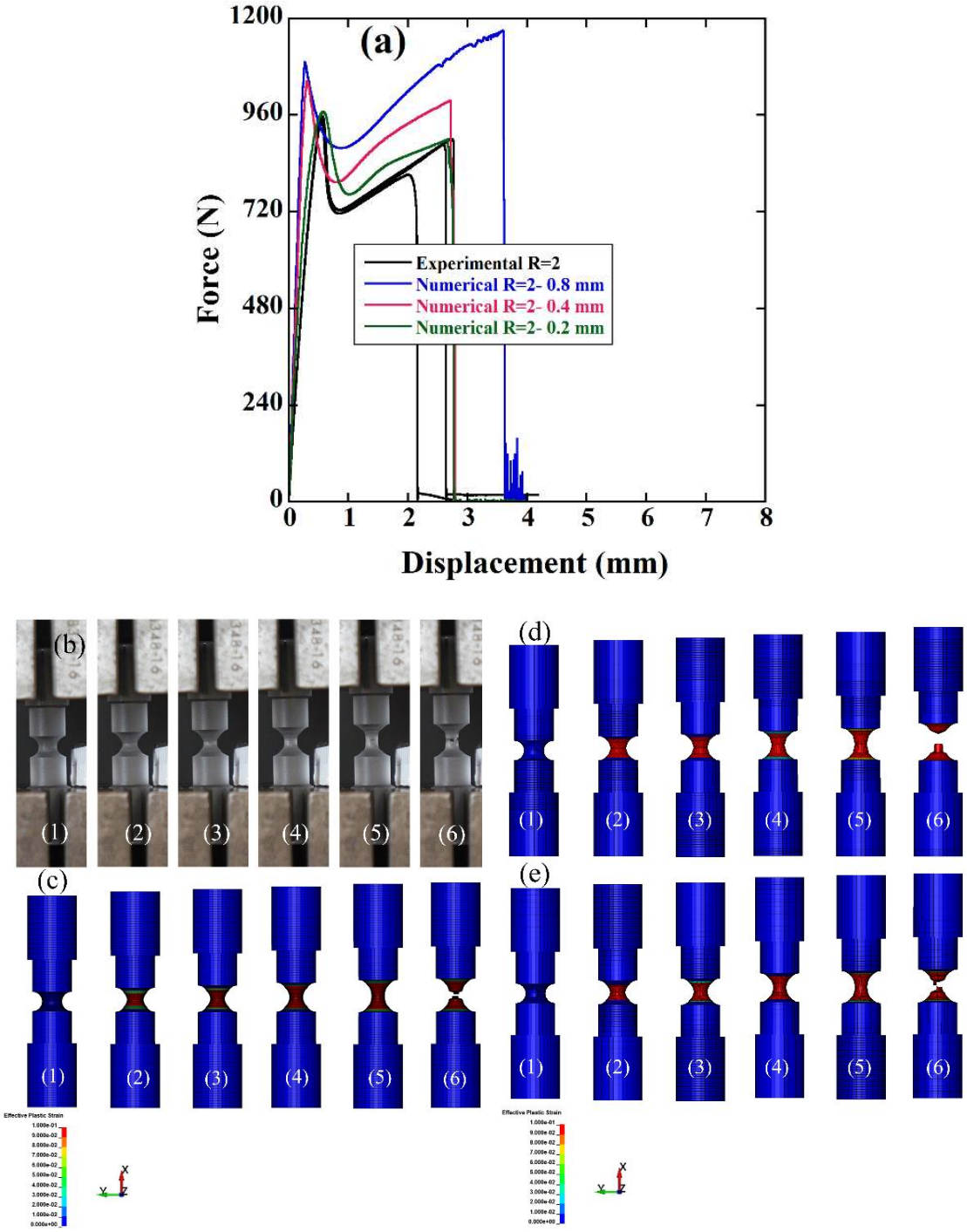

Figure 5.9. The experimental and numerical force displacement curves of the (a) notched R=2 at the strain rate of 10^{-3} s^{-1}, the deformation pictures of the notched tensile PC specimens R=2 (b) experimental, numerical (c) 0.8 mm (d) 0.4 mm (e) 0.2 mm mesh sizes

5.4. The Quasi-static tension temperature tests

The effect of the temperature was determined by performing the tests at the increasing temperatures of 25, 60 and 90°C. All the tests were performed at the strain rate of 10^{-3} s^{-1}. The temperature tests were repeated three times. The PC specimens were in the furnace during the tests. Therefore, extensometer could not used in these tests. The engineering stress-engineering strain curves of these tests are shown in Figure 5.10(a). As seen in the same figure fractured specimens were illustrated, as well. The upper, lower yield points and fracture strains were calculated using stroke strain data taken from the universal testing machine. The average upper yield points at these temperatures (25, 60, and 90°C) are sequentially of the temperature is 69.8 MPa (70.7, 69.8 and 68.9 MPa), 49.0 MPa (50.4, 49.8 and 46.9 MPa) and 31.2 MPa (32.4, 32.2 and 29.1 MPa). The average lower yield points at these temperatures (25, 60, and 90°C) are sequentially of the temperature is 53.9 MPa (54.4, 54.4 and 52.9 MPa), 33.8 MPa (35.1, 35.1 and 31.3 MPa), 19.9 MPa (20.7, 20.7 and 18.4 MPa). The average fracture strains at these temperatures are sequentially of the temperature is 1.41 (1.42, 1.39 and 1.41), 0.73 (1.26, 1.20 and 0.97) and 0.53 (0.59, 0.47 and 0.54). Furthermore, the temperature softening parameter (m) was determined using true stress at 0.11 strain-temperature curve at increasing temperatures. It was found to be 0.438 as seen in Figure 5.10(b).

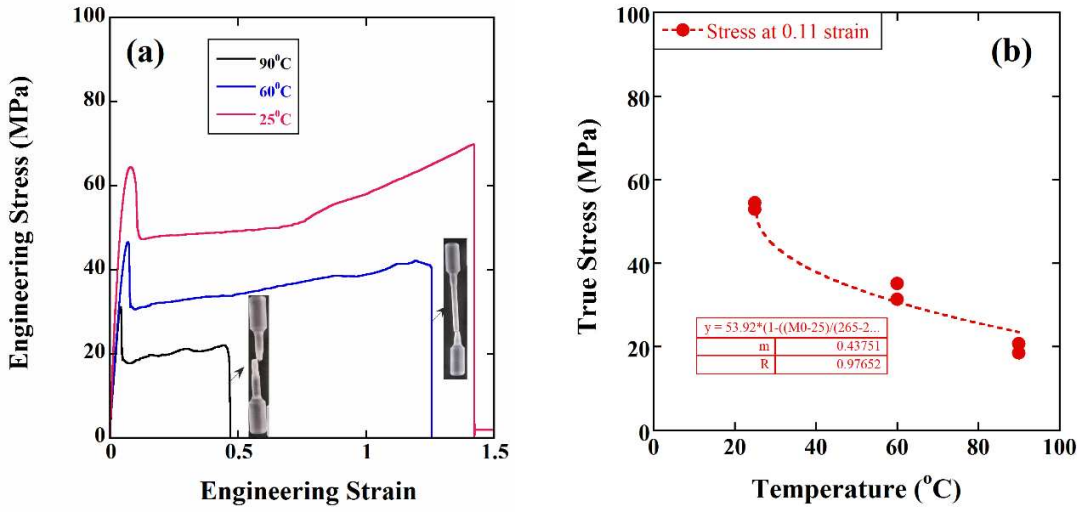

Figure 5.10. (a) the quasi-static tension temperature tests at the strain rate of 10^{-3} s^{-1} (b) true stress-temperature curve of the JC temperature softening parameter (m)

5.5. Quasi-static indentation and low velocity impact tests and simulations

The experimentally and numerically determined flow stress equations and damage parameters so far are tabulated in Table 5.1. The force-displacement curves of the numerical QSI tests using the numerical round tension and notched tension flow stress equations and notched tension flow stress equations result in higher force values than the experiments. The round tension model damage parameters (Table 5.1) are shown in the inset of Figure 5.11(a), together with the experimental QSI test force-displacement curves (3 tests). As seen in the same figure, all the experiment curves exhibit quasi-linear behavior up to failure which corresponds to ~28 mm displacement and rounded peak force ~12000 N. Even though the numerical model curves have a similar trend as with the experimental curves, the numerical round and notched tension flow stress equations result in higher force values than that of the experiments. The round tension damage parameters predict a smaller displacement at the fracture, while the notched tension damage parameters a slightly larger displacement at the fracture than the experiments. The experimentally determined average tension flow stress equation and the numerical notched specimen effective stress equation, however, exhibit comparable force-displacement curves with the experiments as shown in Figure 5.11(b). But they result in smaller displacements at the fracture than the experiments. The damage parameters were then reiterated to match the experimental displacement at fracture. The use of the following damage parameters D_1=1.17, D_2=0.058 and D_3=-5.63 results in very similar force-displacement and the displacement at fracture values with the experiments as shown in Figure 5.11(b). The experimental average compression stress equation gives similar force values with the experiments at low displacements, but it predicts a lower displacement at fracture than the experiment by using the same damage parameters: D_1=1.17, D_2=0.058 and D_3=-5.63 (Figure 5.10(b)). All the flow stress equations and damage parameters listed in Table 5.1. Figures 5.12(a) and (b) show sequentially the side picture of the experimental and numerical QSI test plates (experimental average tension stress equations and the corresponding damage parameters) before, during and after the test. The fracture of the experimental QSI plate occurs with the dome-cap formation as seen in Figure 5.12(a). While the numerical plate forms denting on the impact face of the plate and followed by the petalling fracture (Figure 5.12(b)).

Table 5.1. The determined flow stress equations and damage model parameters

Equation Name	$\boldsymbol{\sigma}$ $\boldsymbol{(MPa)}$ $(A + B\varepsilon_P^n)$	$\boldsymbol{\varepsilon_f}$ $(\mathrm{D}_1 + \mathrm{D}_2 e^{D_3\sigma^*})$
Round tension	$72 + 720\varepsilon_P^{3.3}$	D_1=0.75, D_2=0.060 and D_3=-7.8
Notched tension	$72 + 500\varepsilon_P^{3.3}$	D_1=0.95, D_2=0.065 and D_3=-6.98
Notched effective stress	$56 + 176\varepsilon_P^{2.67}$	D_1=1.17, D_2=0.058 and D_3=-5.63
Experimental average tension stress	$51 + 173\varepsilon_P^{2.12}$	D_1=1.17, D_2=0.058 and D_3=-5.63
Experimental average compression stress	$55 + 68\varepsilon_P^{2.64}$	D_1=1.17, D_2=0.058 and D_3=-5.63

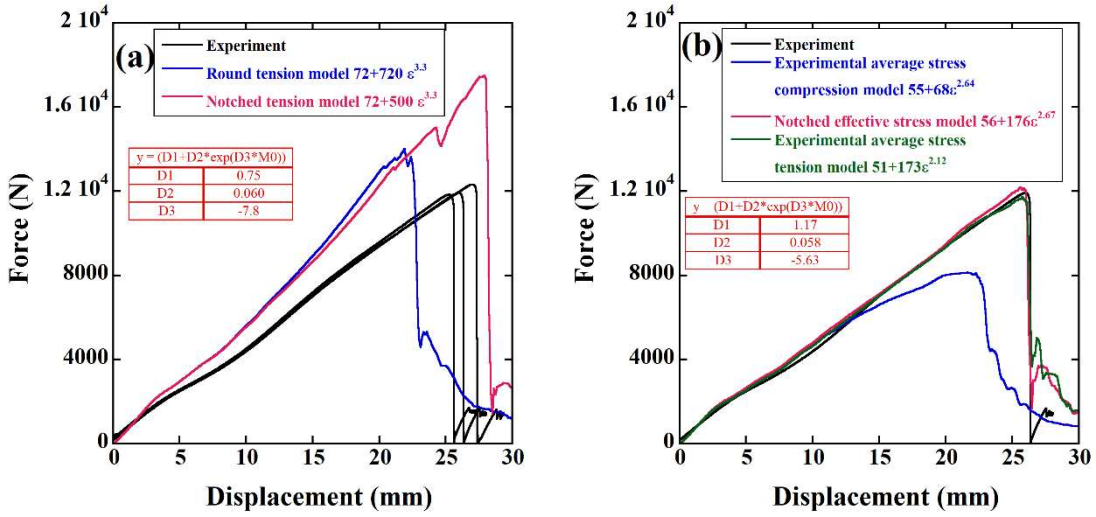

Figure 5.11. The QSI force displacement curves: (a) experimental and round and notched tension equations and (b) experimental and experimental average tension and compression and notched effective stress equations

Figure 5.12 (c) shows the deformation pictures of numerical QSI test plates ($51 + 173\varepsilon_P^{2.80}$). As with Figure 5.12(b), the deformation type is not much altered when the n value increases from 2.12 to 2.80. Figures 5.13(a-e) show the experimental pictures of the fractured plates (rear faces) together with the numerical pictures of the plates. Although the experimental fracture is dome-cap type, a close inspection of the damage reveals small micro-cracks or hackles at the tip of indenter (as seen the inset of the Figure 5.13(a), damaged zone). These hackles do not combine to give a petalling type of fracture as with the numerical model. During the tests, the frictional forces between the indenter and PC plate caused the heating of the specimen at the contact area. This naturally increased the failure strain of the PC locally and prevented formation of a petalling type

fracture and led to the formation of a dome-cap type fracture. After the test, the dome-cap was stuck to the indenter tip due to heating and the dome was separated from the tip by applying external force. The used models cannot however predict the formation of dome-cap failure as the thermal solver was not included in the numerical simulations. A petalling type of fracture starting from the tip of the indenter as shown in Figures 5.13(a-e). The LVI and PI tests were modeled using the experimental average tension stress equation and the corresponding damage parameters. The mesh sensitivity analysis of the LVI experiment was implemented for JC constitutive equation without any rate sensitivity. The mesh sizes were selected as 2, 1 and 0.5 mm, respectively. As seen in Figure 5.14(a), the LVI numerical model results with 1 and 0.5 mm mesh sizes are nearly the same with each other. The deformation pictures of the models with 2, 1 and 0.5 mm mesh sizes are shown in Figures 5.14(c-e). As seen in the same figures, there is no fracture in the numerical specimens as with experiments. The main deformation type is still dishing. The numerical thicknesses of dishes are 3.54, 3.30, 3.35 mm for 2, 1, 0.5 mm, and the numerical diameters of the dishes are 14.08, 14.04, 14.22 mm for 2, 1, 0.5 mm, respectively. The LVI numerical model with 1 mm mesh size is well-agreed with experimental results. Therefore, 1 mm mesh size was used in the numerical models. Five different stress-strain rate relations were implemented to see the effect of strain rate on the deformation and fracture. In the experimental and numerical LVI tests (4.75 m s^{-1} and ~66 J energy), there was no perforation in the PC. Among the investigated strain rate relations with QS-fit, most of the relations show similar force-displacement and force-time curves with the experiments as seen in Figures 5.15(a) and (b) except for CS. Furthermore, the CS relation has relatively more ductility and the peak forces of the CS relation are nearly the same with experiments. The other relations, however, significantly overpredict the experimental force values in the curves. Among the investigated strain rate relations with QSDYNA-fit, CS show nearly similar force-displacement and force-time curves with the experiments as seen in Figures 5.16(a) and (b). As similar with QS-fit, both the other relations result in similar force values with all the displacements; however, they overpredict the experimental force values in the curves (Figure 5.16(a) and (b)).

The experimental and QS- and QSDYNA-fit numerical thicknesses and diameters of the dishes are tabulated in Table 5.2. The CS relations result in the lowest dish thicknesses and the highest dish diameters than the experiments and the other relations.

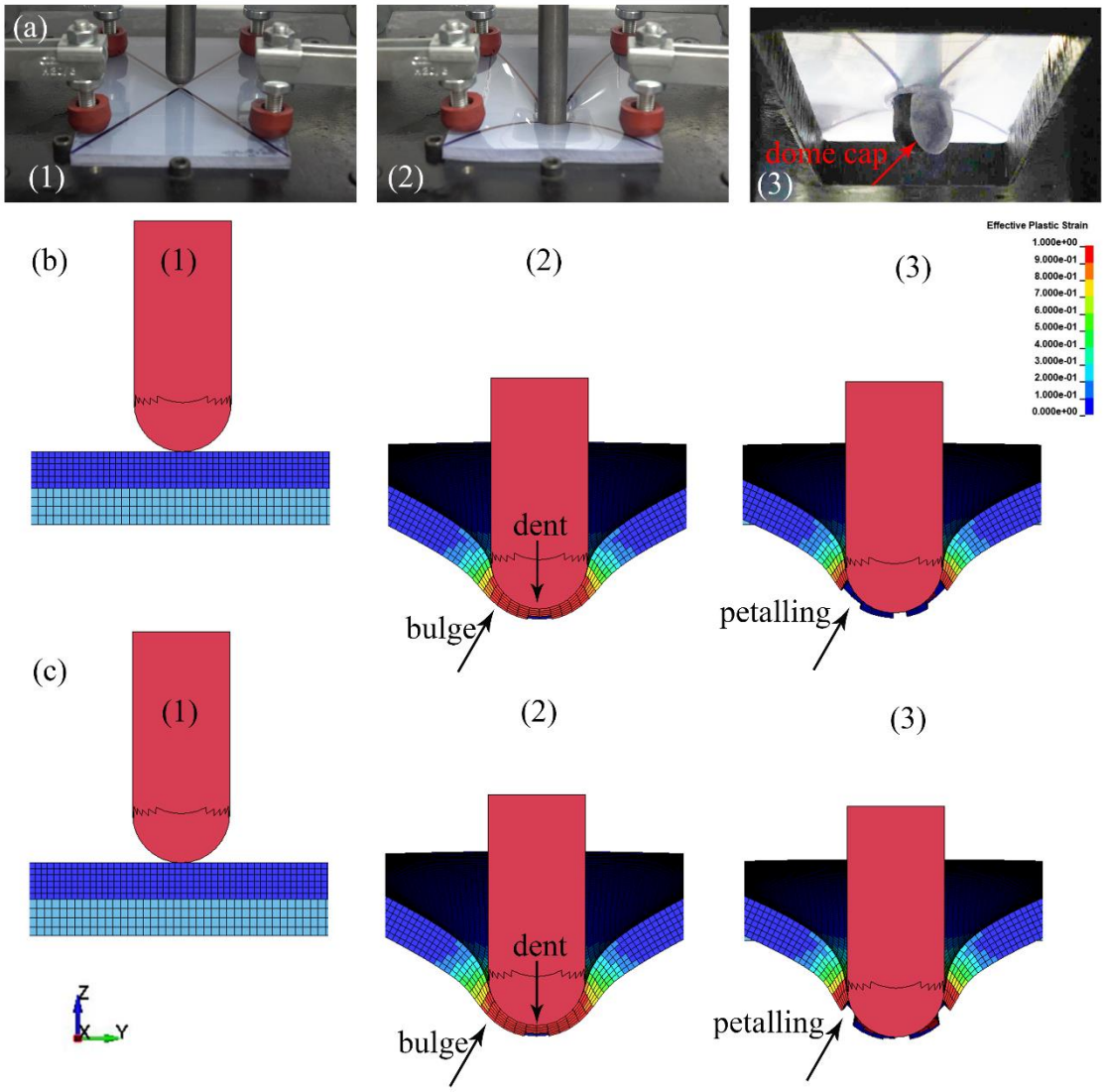

Figure 5.12. The quasi-static indentation force-displacement curves and deformation pictures (a) experiment ,numerical model (b) n=2.12 and (c) n=2.80 (1-before test, 2-just before the fracture and 3-after the fracture)

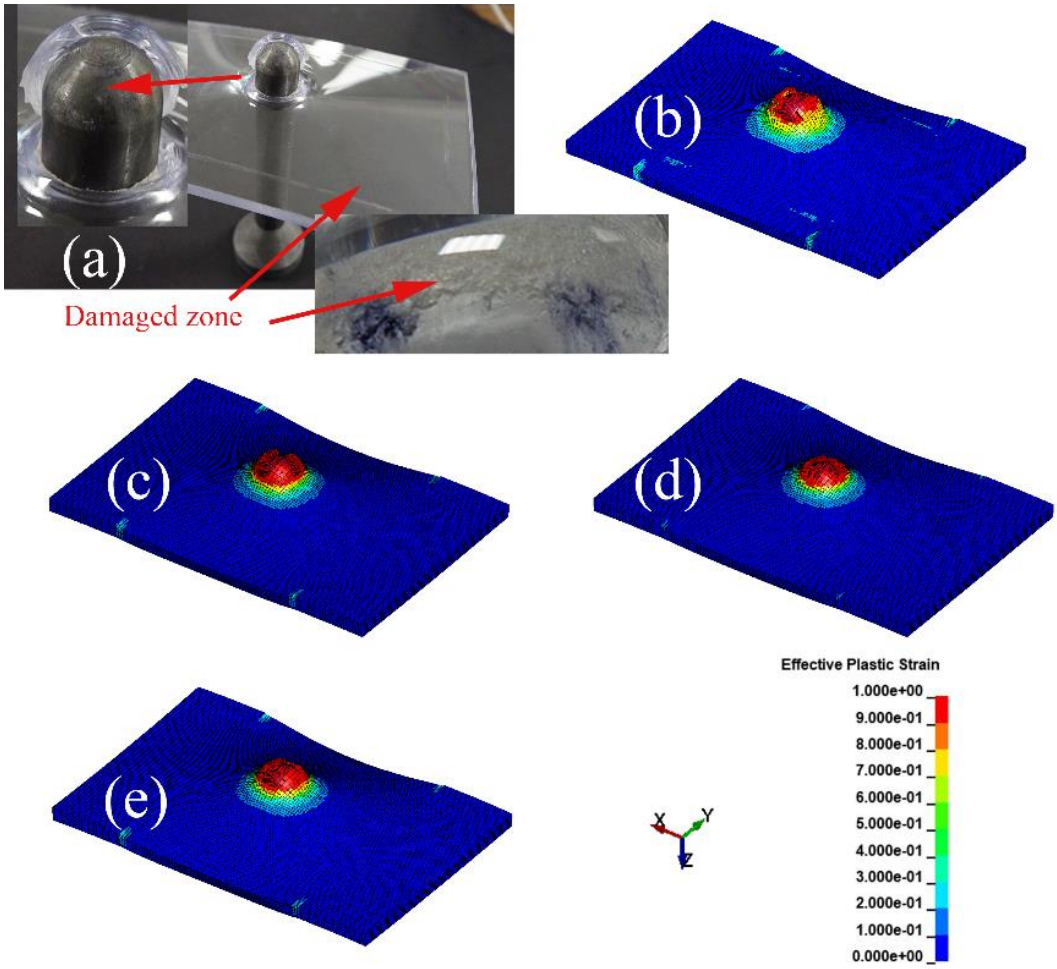

Figure 5.13. The experimental and numerical QSI fracture pictures of the PC plate; (b) round tension, (c) notched equivalent stress (d) experimental average compression stress and (e) experimental average tension stress equation

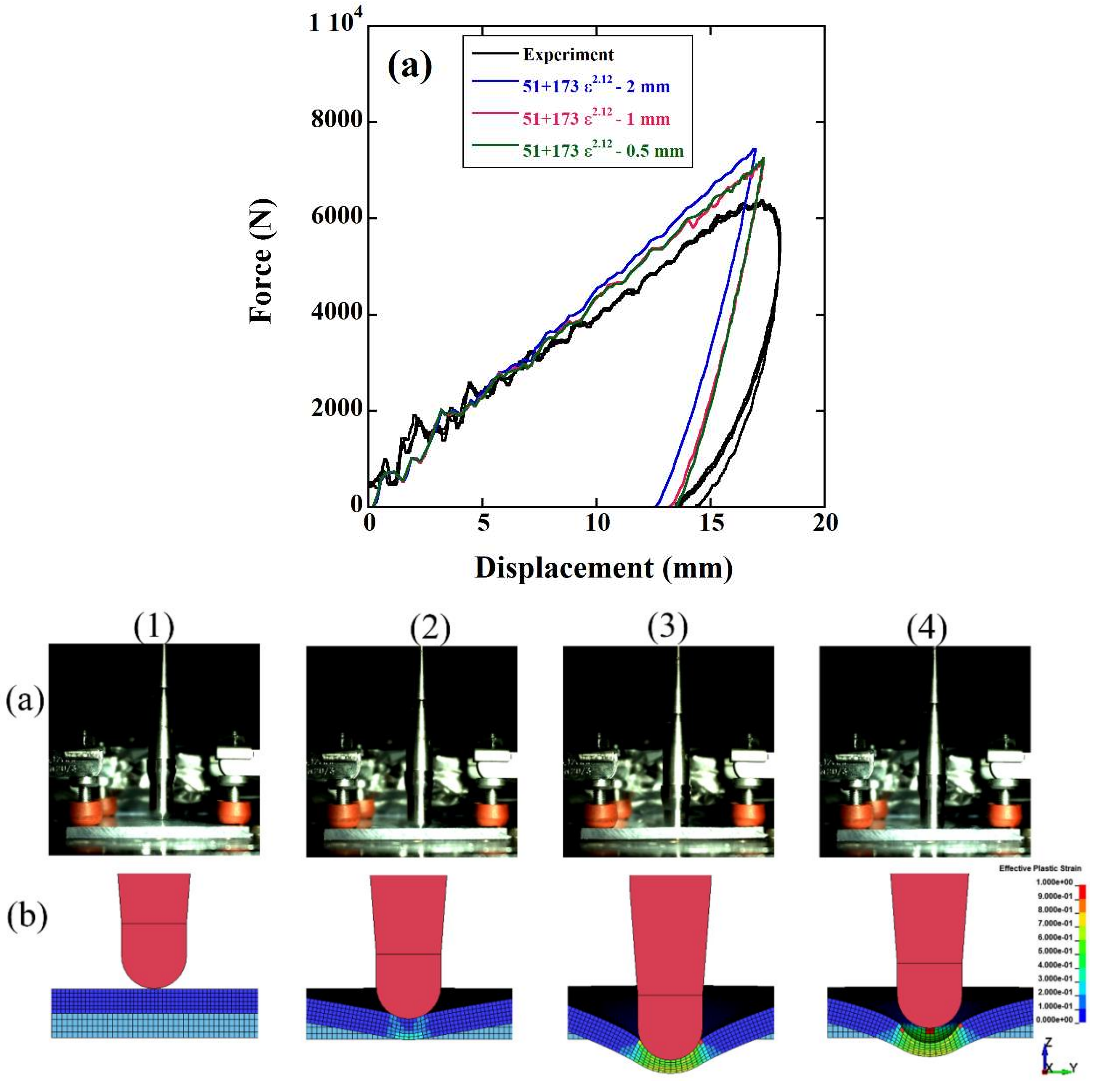

(cont. on next page)

Figure 5.14. (a) the force-displacement curve of LVI test and numerical models of 2, 1, 0.5 mm mesh sized numerical models, the deformation pictures of (b) experiment (c) 1 mm mesh sized (d) 2 mm mesh sized and (e) 0.5 mm mesh sized numerical models 1-before, 2- 7mm displacement, 3-at maximum force and 4- after the experiment

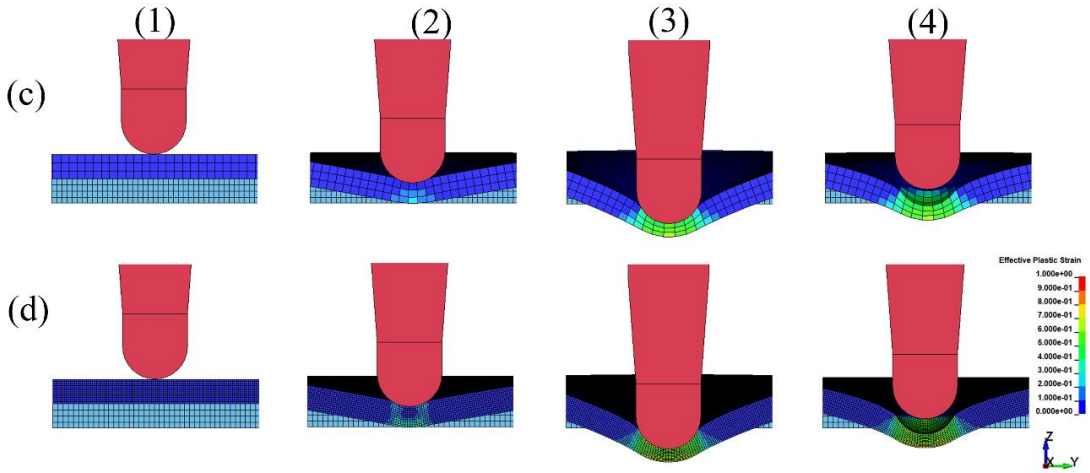

Figure 5.14. (cont)

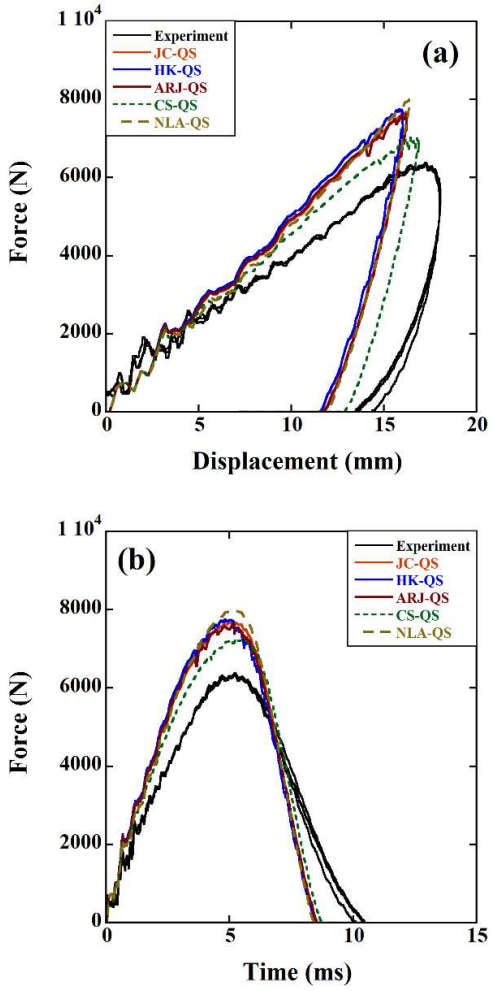

Figure 5.15. (a) The force-displacement and (s) force-time curves of the experimental and QS-fitted strain rate sensitivities numerical LVI tests

The nearest dish thickness of experiment is the NLA relation and the dish diameter is the CS relation. The indenter in LVI model was modeled with MAT_020_RIGID material model card in LS-Dyna. Using rigid material model may neglect some elastic properties in the numerical model of LVI. Therefore, the indenter was modeled with MAT_001_ELASTIC material model card in LS-Dyna. There is no dramatic difference between the force-displacement curve and the deformation behavior of the two models as seen in Figures 5.17(a) and (b). The numerical thicknesses of dishes are 3.30, 3.46 mm for rigid and elastic indenters, and the numerical diameters of the dishes are 14.04, 13.94 mm for rigid and elastic indenters, respectively.

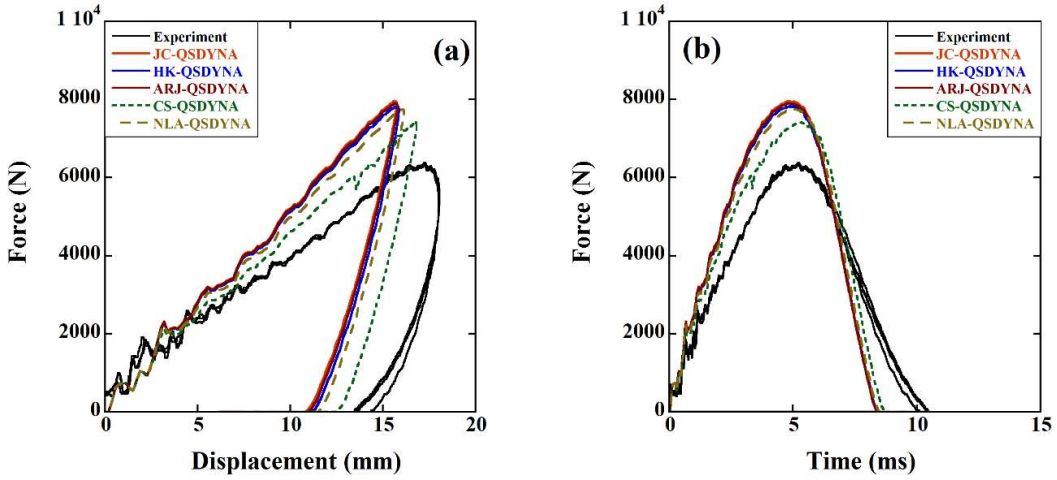

Figure 5.16. (a) the force-displacement and (b) force-time curves of the experimental and Quasi-static+Dynamic fitted strain rate sensitivities in the numerical LVI tests

Table 5.2. Experimental and numerical dish thicknesses and diameters

Property	Experimental	Rate sensitivity	QSDYNA fit	QS fit
Thickness (mm)	3.83 (3.73, 3.83, 3.93)	JC	3.78	3.61
		HK	3.73	3.67
		ARJ	3.76	3.62
		CS	3.44	3.44
		NLA	3.67	3.86
Diameter (mm)	14.02 (14.06, 13.97, 14.02)	JC	13.60	13.72
		HK	13.64	13.68
		ARJ	13.62	13.74
		CS	13.88	13.88
		NLA	13.68	13.58

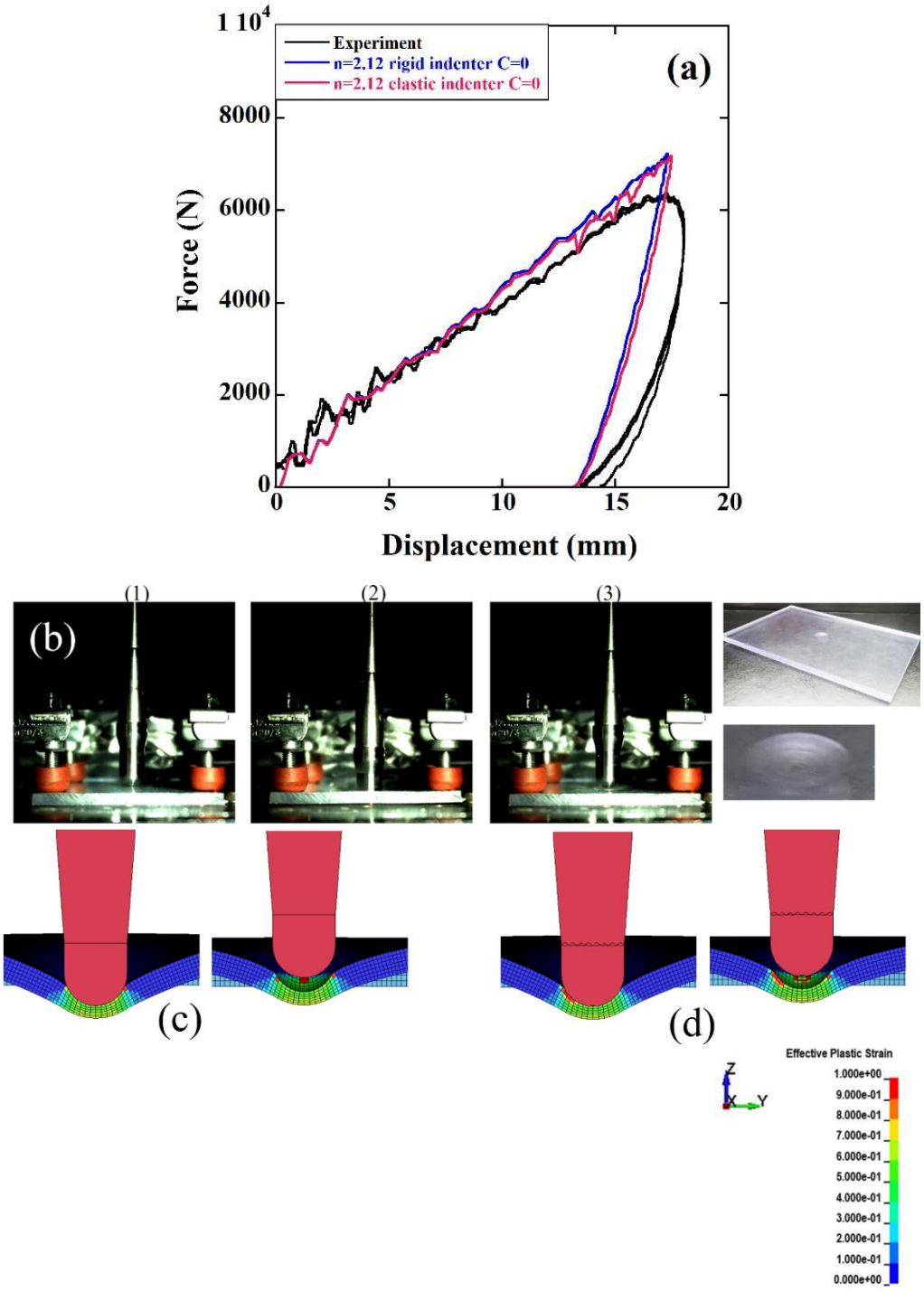

Figure 5.17. The LVI test deformation pictures of the PC plate: (a) experimental (1-before the test, 2) just before the fracture and 3-after the fracture and (b) rigid intender (c) elastic indenter (at and after the maximum force)

5.6. Projectile impact tests and simulations

The PC plates did not fracture experimentally at 100 m s^{-1}. The main damage at these velocities is dishing. Figure 5.18(a) shows the pictures of the projectile and PC target before, during, at maximum, and after the impact at 100 m s^{-1} (1, 2, 3 and 4, respectively). A piece of white paper, as seen in Figure 5.18(a), was inserted at the back of the PC plate to differentiate the formed damage on the PC plate during the test because the PC is transparent. The front and back pictures of the dished region are also shown in Figure 5.18(a). The thickness of the plate in the dished zone gets relatively thinner at the center of the impact, while no fracture is seen on the dish. All the models of five different strain rate relations showed the same deformation type dishing at 100 m s^{-1}, the same as the experiments. Figure 5.18(b) shows the numerical model deformation pictures of JC relation before, during, at maximum, and after the impact at 100 m s^{-1} (1, 2, 3 and 4, respectively). The dent depths of the dished region were measured using a dial micrometer experimentally and determined numerically for the relations investigated. The dent depths of the experimental average and the numerical model with JC relation at the velocity of 100 m s^{-1} are 10.79 and 10.87, respectively.

The PC plates did not fracture experimentally at the velocity of 140 m s^{-1}. The main deformation type is still dishing. This phenomenon is well-agreed with the impact mechanism map reported by Wright and Fleck[33]. There has been, however, an extra denting zone around and in front of the projectile. In the case of the thickness of the specimen becoming larger or the projectile diameter becomes smaller, the deformation behavior of PC would alter from dishing to deep penetration. All the dent depth results are further tabulated in Table 5.3. The JC relation is mainly used for PI numerical models due to having good correlation QSDYNA-fit results (Figure 5.16(d)). The dent depths of the experimental average and the numerical model with JC relation at the velocity of 140 m s^{-1} are 17.06 and 17.90, respectively. The numerical model deformation pictures of JC, HK, ARJ, CS and NLA relations before at and after the impact at 140 m s^{-1} are shown sequentially in Figures 5.19(b-f). All the models result in dishing as seen in Figures 5.19(b-f), as with the experiments. On the other side, the CS relation result in fracture of the plate by petalling as seen in Figure 5.19(c). The numerical values of the depth of dent are higher than that of the experiment at 100 m s^{-1}, while it is just the opposite at 140 m s^{-1}. All the models show similar dent depth at 100 m s^{-1}. Furthermore, the CS relation shows the highest dent depth at 100 m s^{-1} among others. All the relations result in a depth

of dent at 140 m s^{-1} very similar with the experiment (17.06 mm), while the NLA relation shows the lowest dent of depth (17.70 mm) than the experiment. The maximum difference between the experimental and numerical dent depths is 9% at 100 m s^{-1} and increases to 5% at 140 m s^{-1}. The use of JC relation at 100 m s^{-1} and at 140 m s^{-1}gives a dent depth 0.7 % and 5% different from the experimental average dent depth, respectively.

The PC plates were experimentally and numerically perforated by the projectile at 160 m s^{-1} (Figure 5.20(a) and (b)). The fracture of the tested plates was petalling. The petals were entangled with each other as shown in Figure 5.21(a). As seen in the same figure, the petals possessed melted thin layers. These melted thin layers are also evidence of the adiabatic heating of the specimens. The petal thickness is found to be minimum at the center of the projectile impact zone. The numerical models of the JC, HK, ARJ, CS and NLA relations also show petalling type of failure as seen in Figures 5.21(b-f), respectively. An average petal thickness was determined experimentally by measuring the thickness of the fractured sections at the projectile impact zone. The petal thicknesses were also numerically determined at the impact zone. Table 5.4 tabulates the resultant experimental and numerical projectile exit velocities and the average petal thicknesses. The average exit velocity is determined 87.01 m s^{-1} in the experiments and the numerical models using all the relations result in similar exit velocities with the experiment and the maximum difference is 3.69 m s^{-1}, respectively. Furthermore, the numerical models of the all the relations exhibit acceptable exit velocities with the experiments. On the other side, the numerical petal thicknesses (2.84-3.15 mm) were found smaller than that of the experiment (3.84 mm on the average). The PI tests were also simulated using the round tension and experimental average compression stress equations and corresponding damage parameters (listed in Table 5.1), together with the JC strain rate relation. These results further indicate that experimental average tension stress equation and damage parameters correctly predict the main damage type on the PC plates at increasing velocities as tabulated in Table 5.5. Note that the energy absorption values tabulated in Table 5.5 increase more than twice in the PI test at 160 m s^{-1} with respect to the energy absorption in the QSI test.

This also proves the high energy absorption capability of the PC at high velocities. The difference between inner and outer kinetic energies yielded to determine the critical impact velocity. In this study, it was evaluated as ~135 m s^{-1}. This phenomenon is consistent with deformation type of the PC plate.

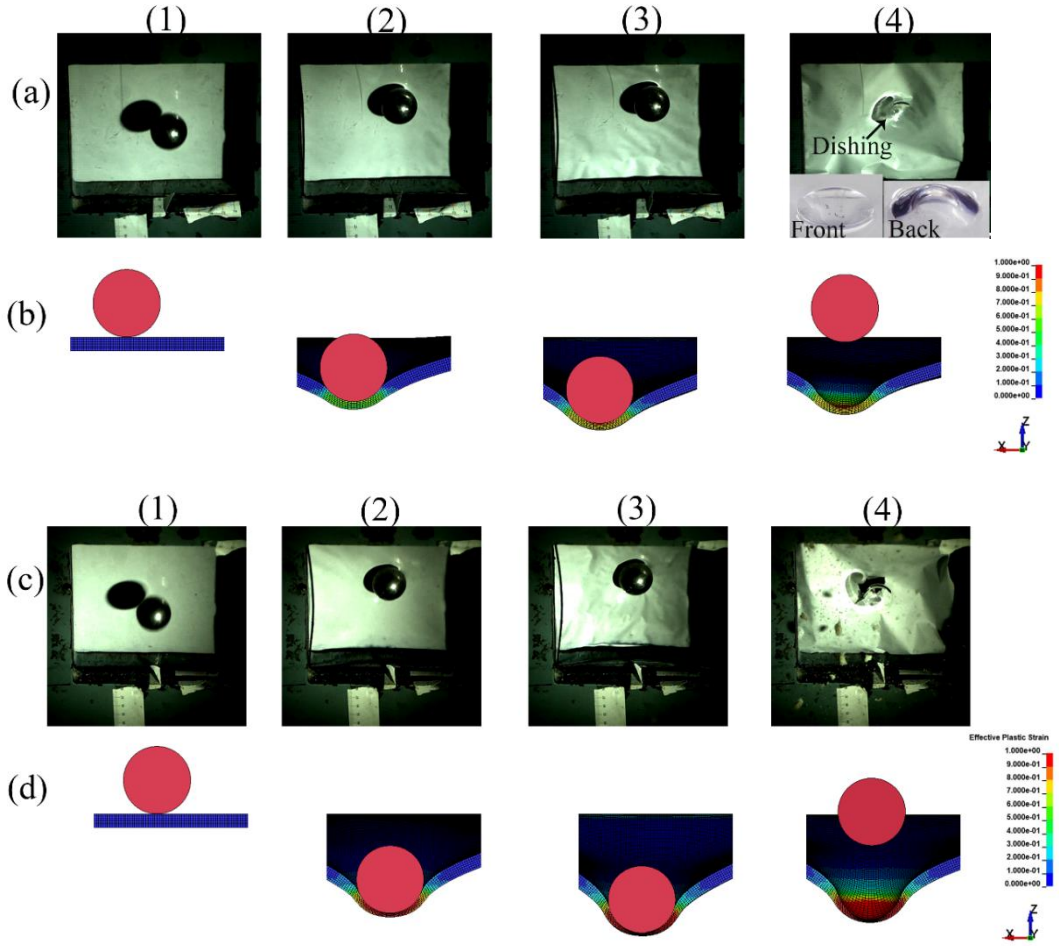

Figure 5.18. The projectile impact test at the velocity of (a) 100, (c) 140 m s^{-1} test and QSDYNA-fitted JC approached model (c)100 (d) 140 m s^{-1} (1-before 2-initial contact 3-maximum depth and 4-after deformation)

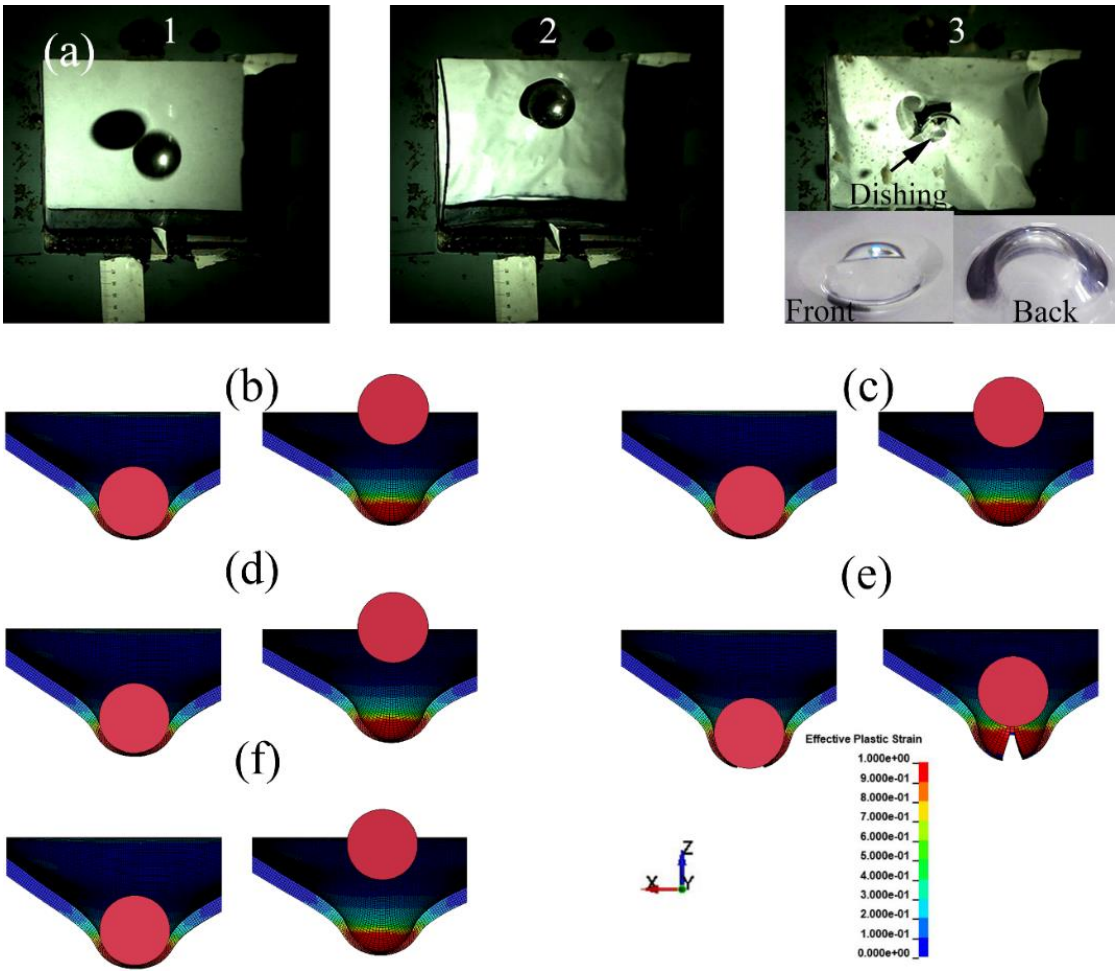

Figure 5.19. The projectile impact at the velocity of 140 m s^{-1} deformation pictures (a) test (b)JC, (c) HK, (d) ARJ, (e) CS and (f) NLA

Table 5.3. The experimental and numerical dent depths of PC at 100 and 140 m s^{-1} PI tests

Velocity (m s^{-1})	Experimental	JC	HK	ARJ	CS	NLA
100	10.79 (10.25, 10.77, 11.36)	10.87	10.88	10.87	11.88	11.19
140	17.06 (16.58, 17.03, 17.30)	17.90	17.94	17.87	-	17.70

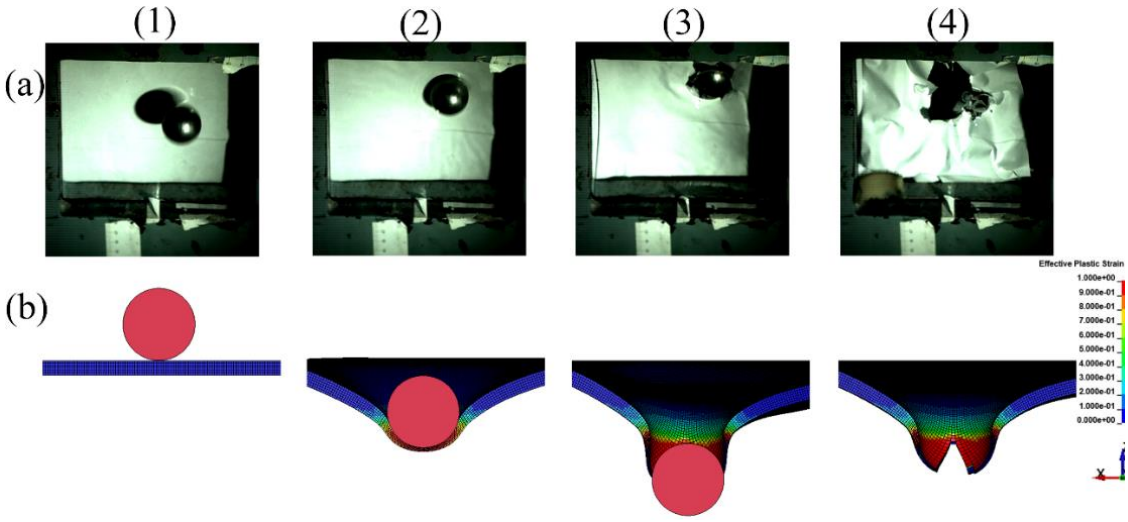

Figure 5.20. The projectile impact test at the velocity of 160 m s^{-1} (a) test and (b) QSDYNA-fitted JC approached model (1-before, 2-initial contact 3-before fracture and 4-after fracture)

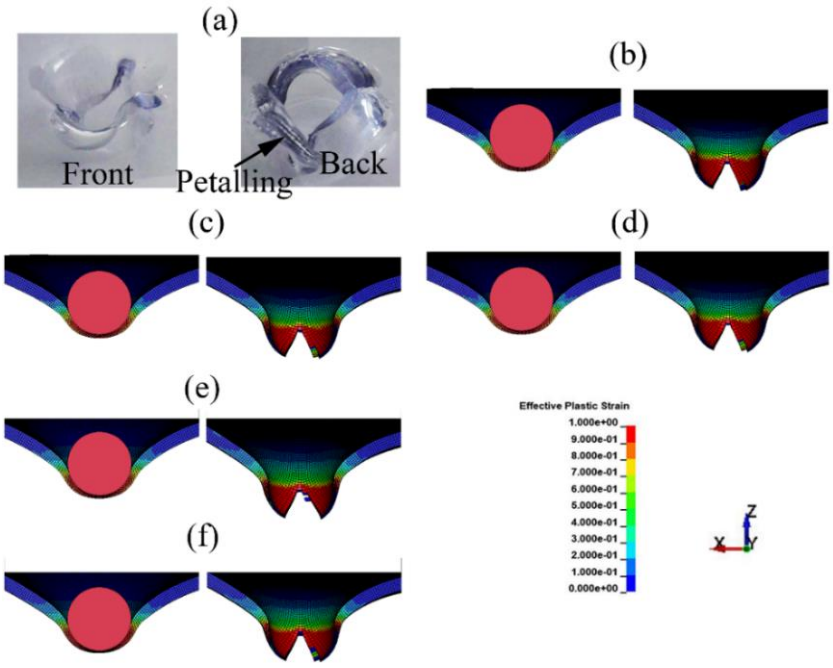

Figure 5.21. (a) the picture of a perforated PC plate after the PI test at 160 m s^{-1} and the side views of the numerical PI test just before and after the perforation using (b) JC, (c) HK, (d) ARJ, (e) CS and (f) NLA relations

Table 5.4. Experimental and numerical exit velocities and petal thicknesses at 160 m/s

Property	Experimental	JC	HK	ARJ	CS	NLA
Exit velocity (m s^{-1})	87(85-89)	87.2	86.4	86.8	91.4	87.3
Petal thickness (mm)	3.84(3.8, 3.84, 3.87)	2.89	2.84	2.86	3.15	3.01

The maximum depth dent occurred at 140 m s^{-1} and the deformation type altered to petalling at the velocity of 160 m s^{-1}.

Table 5.5. The summary of impact velocities, energy levels and damage types of the PC plates

Test type	Velocity (m s^{-1})	Absorbed Energy (J)	Damage type	
			Experiment	Experimental average tension stress equation (JC)
QSI	$6x10^{-3}$	164.68	Denting-petalling	Denting-petalling
LVI	4.75	-	Dishing	Dishing
PI	100	-	Dishing	Dishing
	140	-	Dishing	Dishing
	160	270	Petalling	Petalling

The derivative of the above equation with respect to strain gives the following relation taking ($\sigma = A + B\varepsilon^n$)

$$\frac{n(n-1)}{\varepsilon_u^2} = \frac{A}{B\varepsilon_u^n} - 1 \qquad (4.21)$$

Note that necking starts experimentally at about 0.035 true plastic strain (Figure 5.1(a)). The left and right side of the Equation (4.21) are drawn for the flow stress equations tabulated in Table 5.1 in order to predict the value of n. The resultant n values for $\varepsilon_u = 0.035$ are shown in Figure 5.22(a) with the arrowed numbers. As is noted in the same figure, fairly large B values give an n value higher than 3 which is valid for both the round tension and notched tension stress equations (n=3.3 and 3.14, respectively). The value of n decreases at decreasing B values and n=2.85 for the notched equivalent stress equation, n=2.8 for the experimental average tension stress equation and n=2.4 for the experimental average tension stress equation in the simulations than the predicted one. To see the effect of n value on the stress-strain curve, the experimental average tension

stress equation stress-strain curve is drawn for both n values, 2.8 and 2.12, and the results are shown in Figure 5.22(b). In the same figure, the equivalent stress-strain curve and the experimental average stress and strain data are also shown for comparison. An increase in the n value from 2.12 to 2.8 slightly decreases the flow stresses. But the stress equation with higher n value well approximates the equivalent stresses in the necking region, while the stress equation with lower n value well approximates the equivalent stress near the fracture. The QSI and LVI tests were further simulated using n=2.8 in the experimental average tension stress equation and damage parameters and the no strain rate sensitivity relation. The results are shown for the QSI and LVI tests in Figures 5.22(c) and (d), respectively. The numerical QSI and LVI tests force-displacement curves are nearly the same for n=2.12 and 2.8 until about 12 mm displacement and at increasing displacements, n=2.8 results in slightly lower force values (Table 5.6). The use of n=2.8 results in a lower LVI dish thickness and a higher dish diameter than the use of n=2.12. When the impact velocity is 160 m s^{-1}, the use of n=2.8 results in a higher petal thickness and a lower exit velocity than the use of n=2.12. This is ascribed to a higher fracture strain of the equation with n=2.8, which leads to an increase in the absorbed energy.

Table 5.6. Experimental and numerical dish thicknesses and diameter, dent depth, exit velocity and petal thickness of the experimental average tension stress equation with n=2.12 and n=2.8

Property	Experiment	n=2.12	n=2.8
LVI dish thickness (mm)	3.83 (3.73-3.93)	3.30	3.11
LVI dish diameter (mm)	14.02 (13.97-14.06)	14.04	14.22
Dent depth at 100 m s^{-1} (mm)	10.79 (10.25, 10.77, 11.36)	10.87	11.74
Dent depth at 140 m s^{-1} (mm)	17.06 (16.58-17.30)	17.90	17.27
Exit velocity at 160 m s^{-1} (m s^{-1})	87 (85-89)	87.2	81.8
Petal thickness at 160 m s^{-1} (mm)	3.84 (3.8-3.87)	2.91	3.09

The numerical test at 160 m s^{-1} was also simulated using an elastic projectile (E=210 GPa and density=7800 kg m^{-3}) with the strain rate sensitivity of the JC relation in order to check the projectile material model on the PI deformation behavior of the plates. The use of the elastic projectile results in about 0.4 m s^{-1} lower exit velocity than the use of the rigid projectile as shown in Figure 5.22(a).

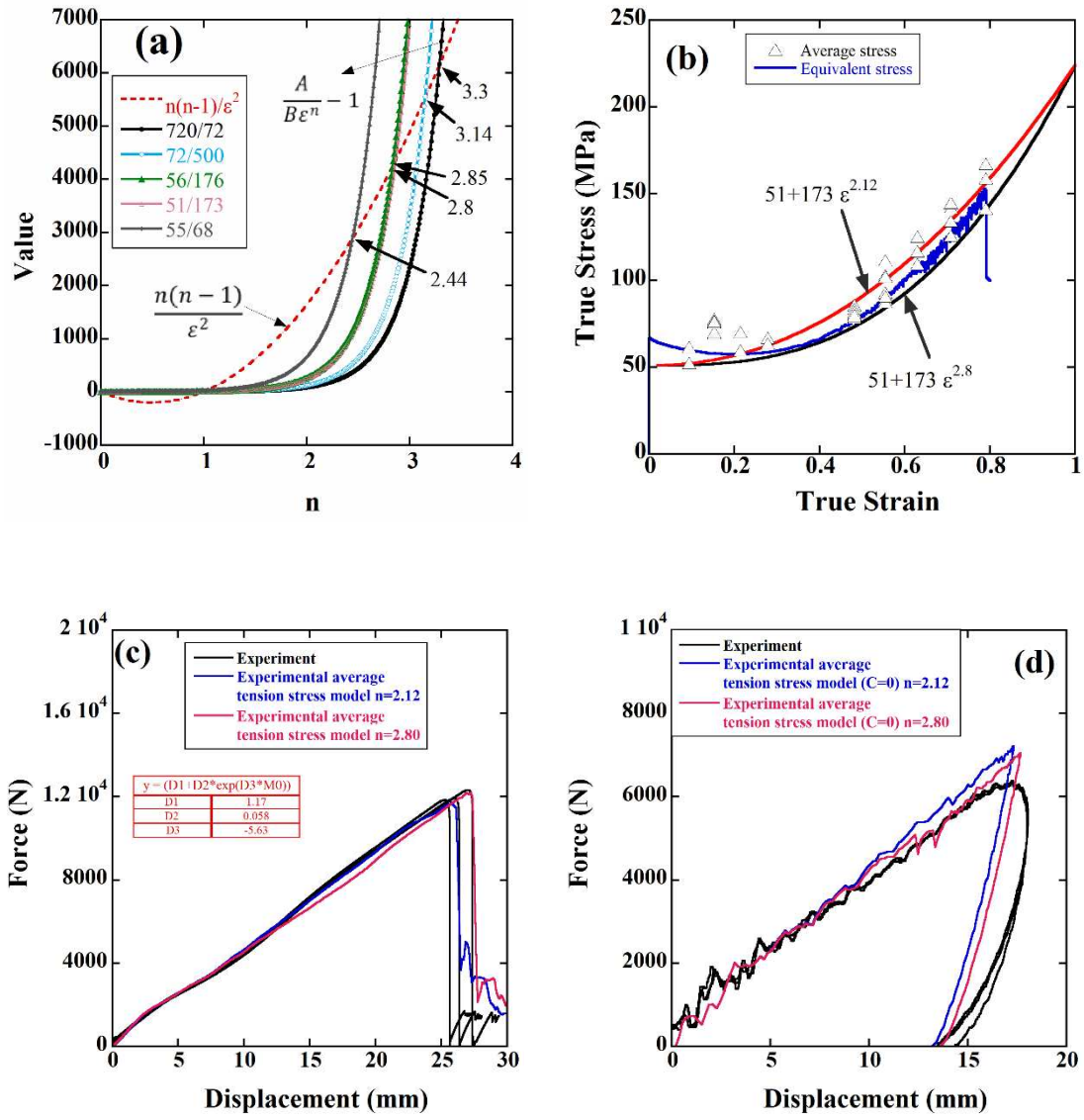

Figure 5.22. (a) predicted n values of the equations in Table 5.1 using Equation. 4.21, (b) comparison of stress models with different n values and force displacement curves of experimental average tension stress no rate sensitivity with n=2.12 and n=2.8 (c) QSI and (d) LVI

On the other side, the no strain rate sensitivity model resulted in projectile exit velocity of 106 and 99.3 m s^{-1} for n=2.12 and n=2.8, respectively. These velocities are much greater than those of the experiments. These results further confirm an increased energy absorption capability of the tested PC at high impact velocities. Two different strain rate sensitivity regions as stated in the introduction are also seen in the tested PC, marked as 1 and 2 in Figure 5.22(b). The transition strain rate is determined by drawing straight lines to the data on the initial peak stress and the compressive stress at 0.5 strain-logarithm of the strain rate graph in the same figure. The critical strain rate is determined at about 200 s^{-1}. The determined transition strain rate range well agrees with the previous studies 150 s^{-1} was reported in reference[3]., 100 s^{-1} in reference[98]. and 10 s^{-1} in reference[68] aforementioned before. As stated earlier, the strain rate sensitivity in region 1; however, decreases as the strain increases and almost no strain rate sensitivity is seen at 0.9 strain at the quasi-static rate range as shown in Figure 5.22(b). A lower strain rate sensitivity at lower strain rates is governed by the α-transition (the restriction of the rotation and translation of the main chains) and higher strain rate sensitivity at HSRs by the β-transition (the restriction of the main chain phenyl group)[17, 99]. The temperature of the α-transition was measured $\sim 150^{o}$C and the β-transition $\sim -95^{o}$C at the 3.2 x 10^{-3} s^{-1} in reference[3]. The numerical strain rate histories of LVI and PI test at 140 m s^{-1} at the mid-section of the impacted area. The numerical (the JC relation) element effective strain rate histories of the LVI test and PI test at 140 m s^{-1} at the mid-section of the impacted area of the PC are shown in Figures 5.23 (a) and (b). The largest strains are determined at the back of the impact area. Therefore, the selected mid-section broadly represents the average strain rates on the tested plate. The strain rates are shown for selected left, center and right elements in the mid-section. An average strain rate was further calculated for each test and is shown in the corresponding graphs. In the LVI test, the strain rate at the center element is the highest while the strain rates at the left and right elements are lower. The average strain rate is determined 57 s^{-1} which falls into the region 1 of Figure 5.23(c).

The detected almost no strain rate sensitivity in the LVI tests is partly due to the dependency of the flow stress at these relatively high strains. Any strain rate dependency of the flow stress is likely to be concealed by the adiabatic heating at the intermediate strain rates. At this average strain rate, the CS relation has the lowest and the JC relation has the highest flow stress. Therefore, the CS relation predicted the lowest forces, and the JC relations predicted the highest forces in Figure 5.16(a). The average strain rate of the PI test is determined 1400 s^{-1} as shown in Figure 5.23(d).

The determined strain rate falls into the second region of Figure 5.23(c). As noted in Figure 5.16(a), all the relations predict pretty much similar flow stresses at the strain rate of 1700 s^{-1} except the CS relation. The CS relation predicts a lower flow stress just below the critical strain. Therefore, the CS relation results in fracture of the plate (with no perforation) at 140 m s^{-1}. On the other side, the average strain rate at 160 m s^{-1} was found to be similar projectile exit velocities with each other, except the CS relation. These results are however valid for impact velocities studied and higher impact velocities may give different results by using the different stress-strain rate relations.

5.7. Validation of bird strike model on the polycarbonate canopy

The bird strike numerical model was composed of PC canopy and bird. The JC material models of the PC determined previously by the experimental and numerical tests were used in the bird impact simulations. The most accurate material model was the experimental average tension stress with JC strain rate sensitive constitutive model among them. Therefore, that one was employed in the bird strike simulations. The MAT_010_ELASTIC_PLASTIC_HYDRO with EOS_GRUNEISEN material model of the bird used in the numerical simulations also needs to be clarified. The validation models of the bird impact are composed of bird impact on a rigid plate and bird impact on deformable plate models. In the bird impact on a rigid plate model, Wilbeck's experiment[73], was implemented in the LS-Dyna. In this model, the bird is impacted on a rigid steel plate and the peak and steady flow pressures are determined by averaging technique(using the ratio of the resultant contact force[100] on the impacted area instead of using the pressure applied on the center of impact). The pressure-time history of the used numerical simulation is compared with the experimental data in Figure 5.24(a). As is seen in the same figure, the numerical peak pressure does not match with the experimental peak pressure even though finer meshes were used in the impact region of the steel plate. The mean pressure values of the simulation and experiment of the bird strike, on the other side, are consistent with each other as depicted in Figure 5.24(b). The mean pressure values are 5.21 and 6.33 MPa for the Wilbeck's experiment and the numerical simulation, respectively. Note that the Hugoniot-jump pressures were ignored in the calculation. Cwiklak et al.[76] are tabulated the values of normalized Hugoniot's and steady-flow pressure at the velocity of 116 m s^{-1} obtained by other researchers

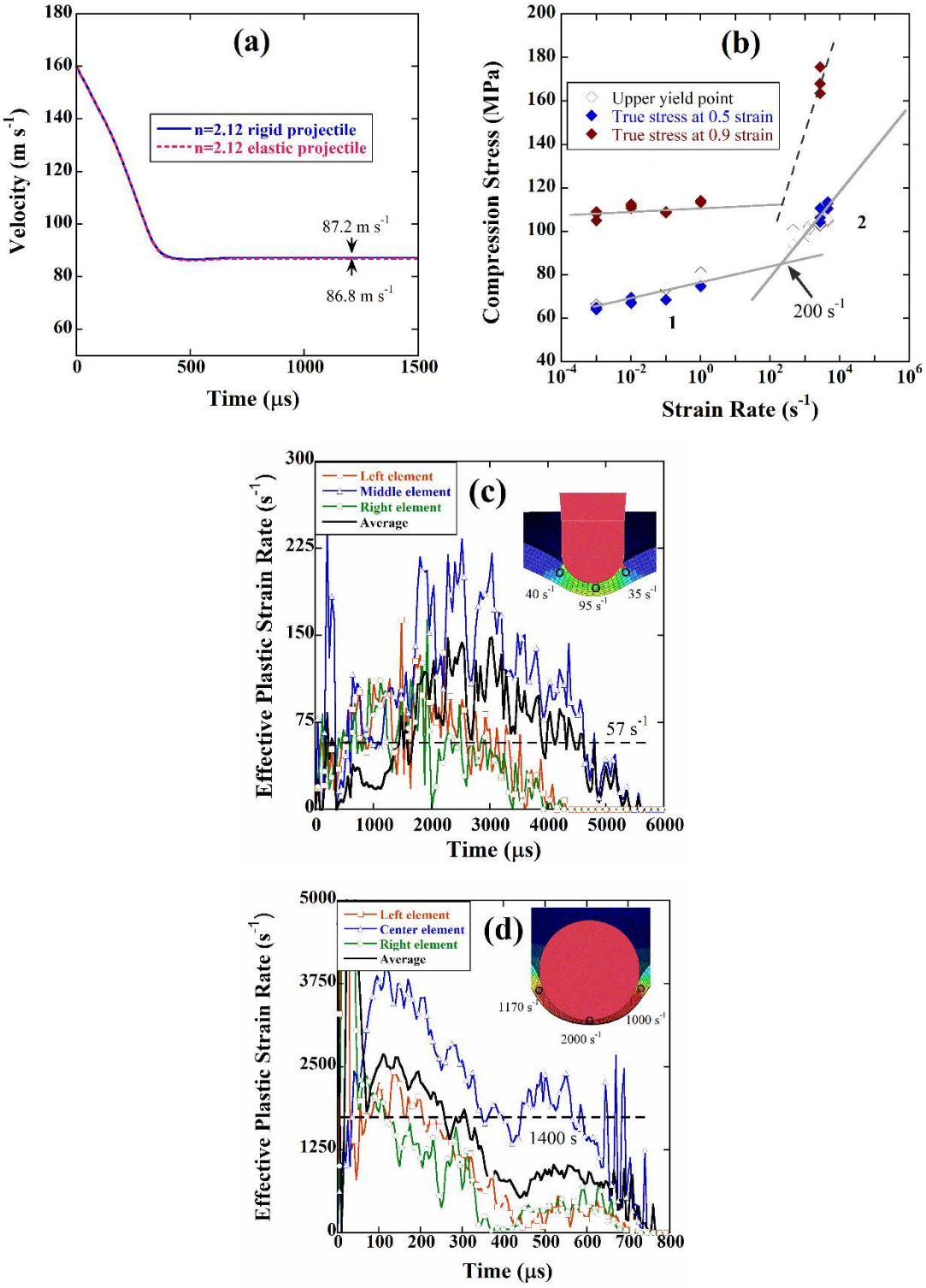

Figure 5.23. (a) PI projectile velocities with rigid and elastic projectile at 160 m s^{-1}, (b) compression stress-strain rate graph showing two different strain rate sensitivity regions and numerical element effective strain rate-time histories of the (c) LVI and (d) PI test at 140 m s^{-1} at the mid-section of the impacted area

The values are altering from 3.6 and 14.1 for the normalized Hugoniot's pressures and from 0.5 to 1.58 for a stagnation one.Therefore, the measurements of these pressures are not sufficient for being sure about the bird model. Furthermore, Figures 5.25(c) and (d) depicted the deformation of bird at different time intervals such as before, at and after impact times. The deformation began with the impact end of the bird and eventually the bird was thoroughly fractured. The numerical model of the bird was further verified by bird impact on deformable plate model. The experiment of Welsh and Centonze[77] was implemented as bird impact on deformable plate model in the numerical model. In this experiment, a substitute bird with 146 m s^{-1} velocity was impacted on thin aluminum plates to determine the resultant deformation in the plate. The displacement-time history of the numerical simulation was compared with the maximum experimental deformation data as depicted in Figure 5.26(a). The simulation predicted the maximum value of deformation of 50.7 mm which is in accordance with the experimentally measured value of 41.2 mm. Furthermore, Figure 5.26(b) shows the deformation pictures of the bird and plate at different time intervals.

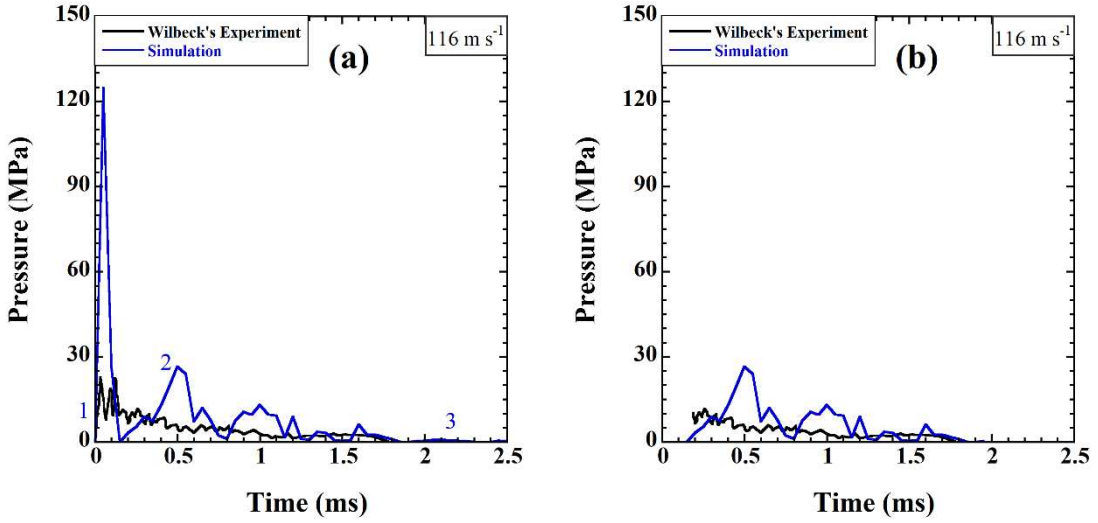

(cont. on next page)

Figure 5.24. The bird verification models (a) the pressure-time histories of the Wilbeck's experiment and its numerical model (b) pressure-time history for mean pressure calculation and (c) the Wilbeck's experiment 1-before, 2-after first contact 3- after impact (top and front views)

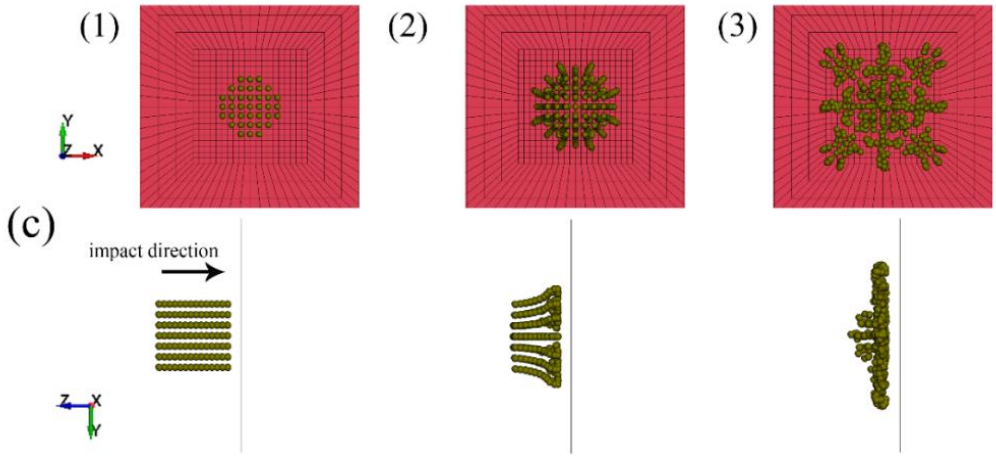

Figure 5.24. (cont.)

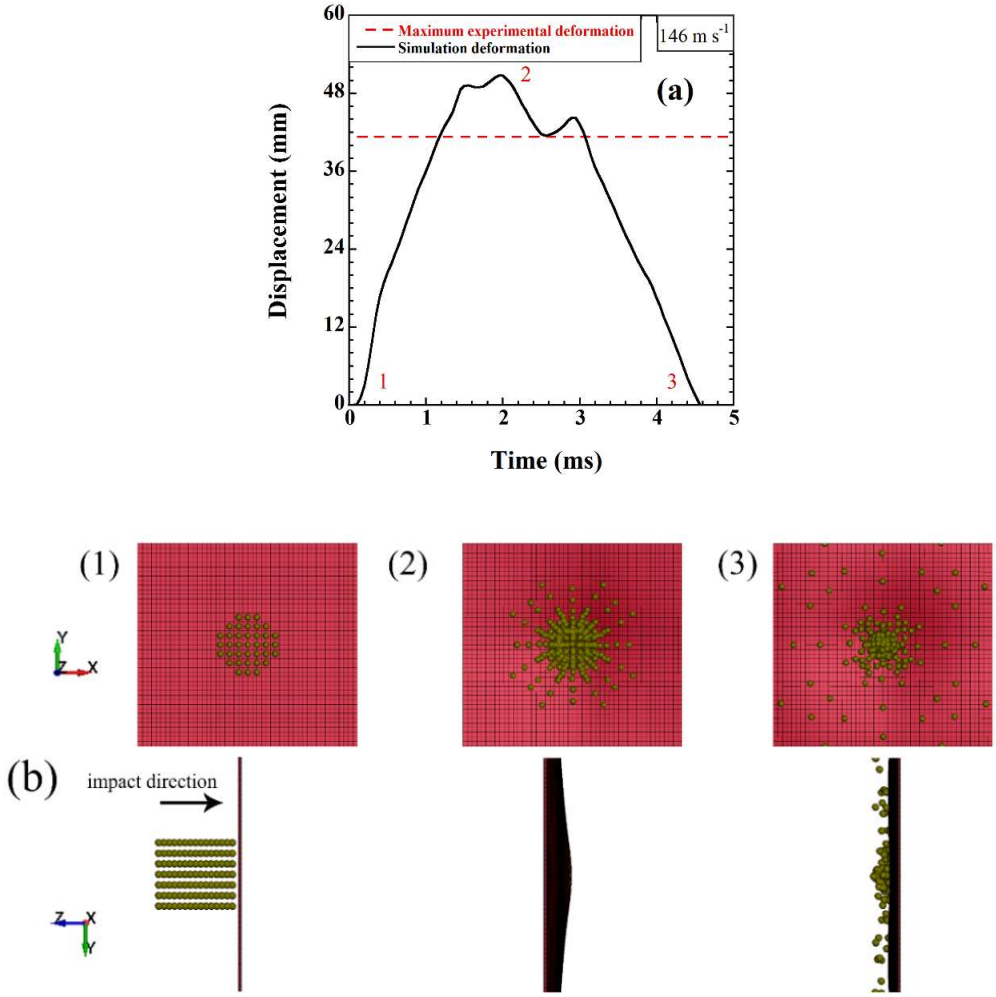

Figure 5.25. The bird verification models (a) the pressure-time histories of the Welsh and Centonze's experiment and its numerical model (b) its model 1-before, 2-at maximum displacement 3- after impact (top and front view)

A bird strike model was developed to simulate a full-scale bird strike on the PC canopy of an aircraft. The bird strike simulation was implemented at three different velocities, low velocity (116 m s^{-1}), intermediate velocity (140 m s^{-1}), and high velocity (230 m s^{-1}). In these simulations, canopies were modeled with two different thicknesses, 6 and 10 mm. Figure 5.26(a) and Figure 5.27(a) exhibit the percent thickness reduction-time history results of 6 and 10 mm, respectively. The percentage of thickness reductions are listed as 2.88, 7.94, 38.35%, for the thickness value of 6 mm at increasing velocities of 116, 140, 230 m s^{-1}, respectively. The deformation pictures of all the numerical simulations are depicted in Figures 5.26(b-d). As is seen in Figures 5.26(b-d), residual effects of bird enhance at the increasing velocities. Furthermore, the catastrophic failure approximately reaches the limit at the velocity of 116 m s^{-1} for 6 mm-thick canopy.

The thickness reductions are listed as 0.21, 0.56, 14.93%, for the thickness value of 10 mm at the increasing velocities of 116, 140, 230 m s^{-1}, respectively. The deformation pictures of all the numerical simulations are depicted in Figures 5.27(b-d). The bird's residual damages on the canopy are increasing as the impact velocities of bird increase. the catastrophic failure approximately reaches to the limit at the velocity of 230 m s^{-1} for 10 mm-thick canopy.

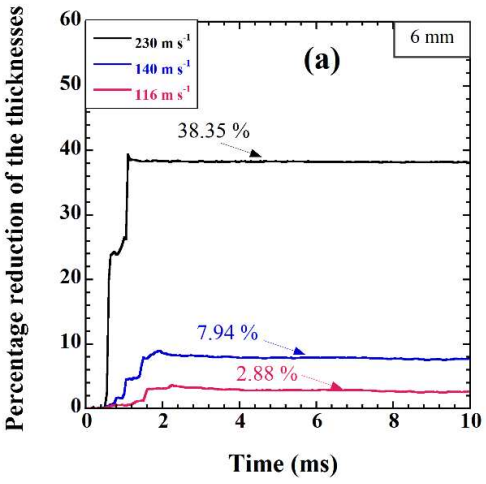

(cont. on next page)

Figure 5.26. The bird strike on PC canopy (a) the percentage reduction of the thicknesses- time histories of 6 mm PC and the deformation pictures of bird strike models (1-before 2-during 3-after impact) for 6 mm thickness at the velocities of (c) 100, (d) 140 and (e) 230 m s^{--1}

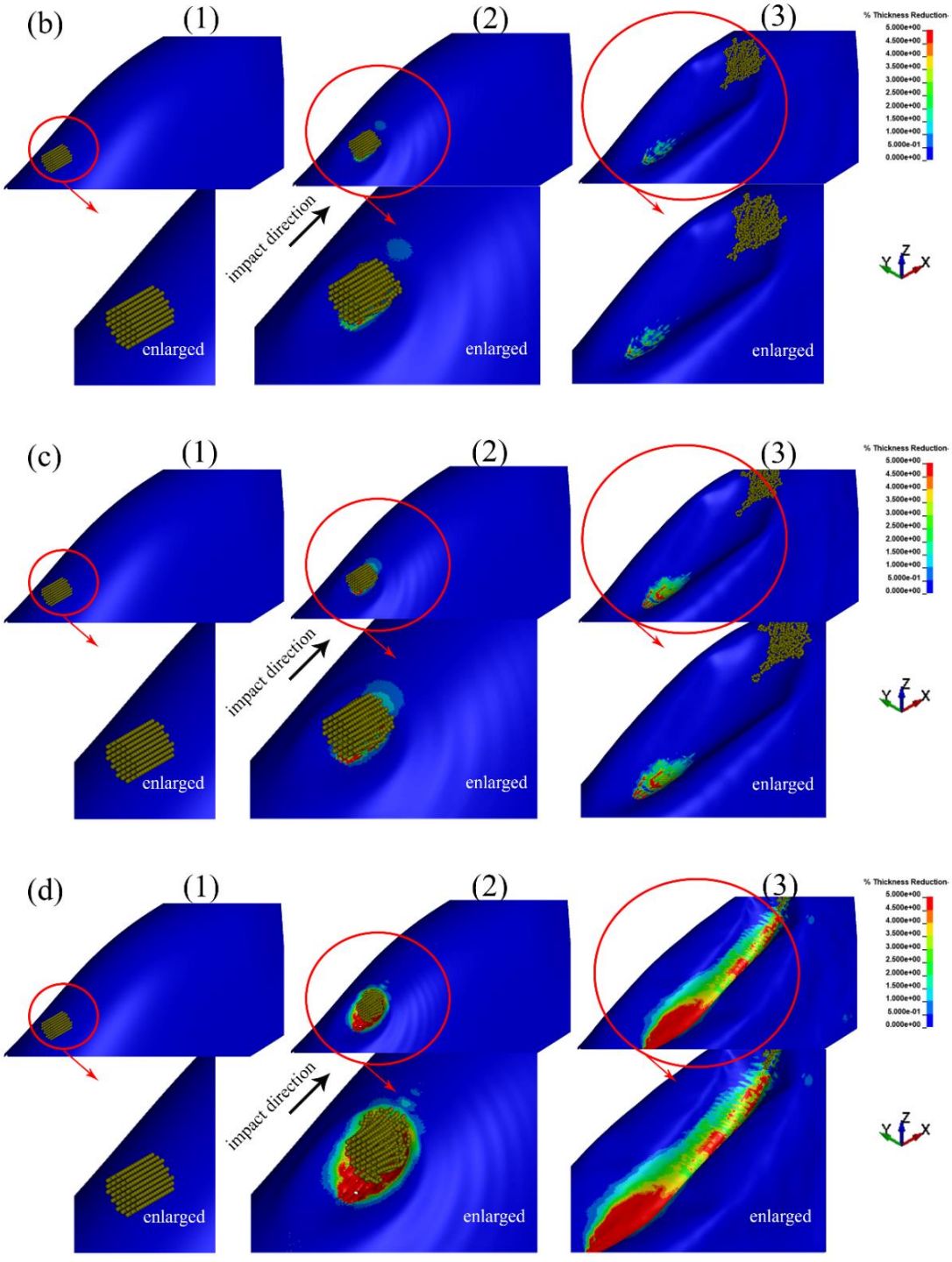

Figure 5.26 (cont.)

Most of operation-induced damages can be repaired by grinding which usually reduces the thickness by 0.3- 0.5 mm[101]. Therefore, catastrophic failure can be assumed as 5-8% thickness reduction for 6 mm-thick, 3-5% thickness reduction for 10 mm-thick canopies. The internal energy levels of 6 mm- thick canopies are 1.83, 3.18 and 22.71 kJ while the internal energy levels of 10 mm-thick canopy are 2.73, 4.61 and 23.26 kJ at the increasing velocities 116, 140 and 230 m s^{-1}, respectively. Abrate[72] listed the bird strike design criteria with respect to the bird's mass, velocity and kinetic energy level.

The bird mass, velocity and kinetic energy should be 1.81 kg, 152.4 m s^{-1} and 21.1 kJ, respectively. When compared to the results of the present study, bird mass is the same for all low, intermediate, and high impact velocities. The present study approximately covered the velocity of 152.4 m s^{-1} by expounding intermediate velocity impact (140 m s^{-1}) model results. The internal energy level of both thicknesses, 22.71 and 23.26 kJ exceed the critical level at the velocity of 230 m s^{-1},21.1 kJ, as depicted as in the Figures 5.28(a) and (b). Therefore, the most critical velocity level for both thicknesses is clarified as nearly 230 m s^{-1}.

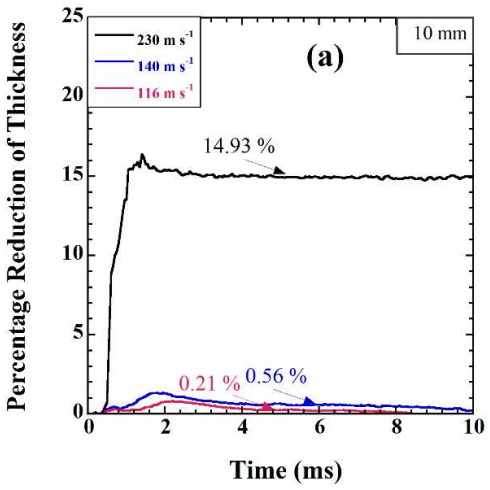

(cont. on next page)

Figure 5.27. The bird strike on PC canopy (a) the percentage reduction of the thicknesses-time histories of 10 mm PC and the deformation pictures of bird strike models (1-before 2-during 3-after impact) for 10 mm thickness at the velocities of (c) 100, (d) 140 and (e) 230 m s^{-1}

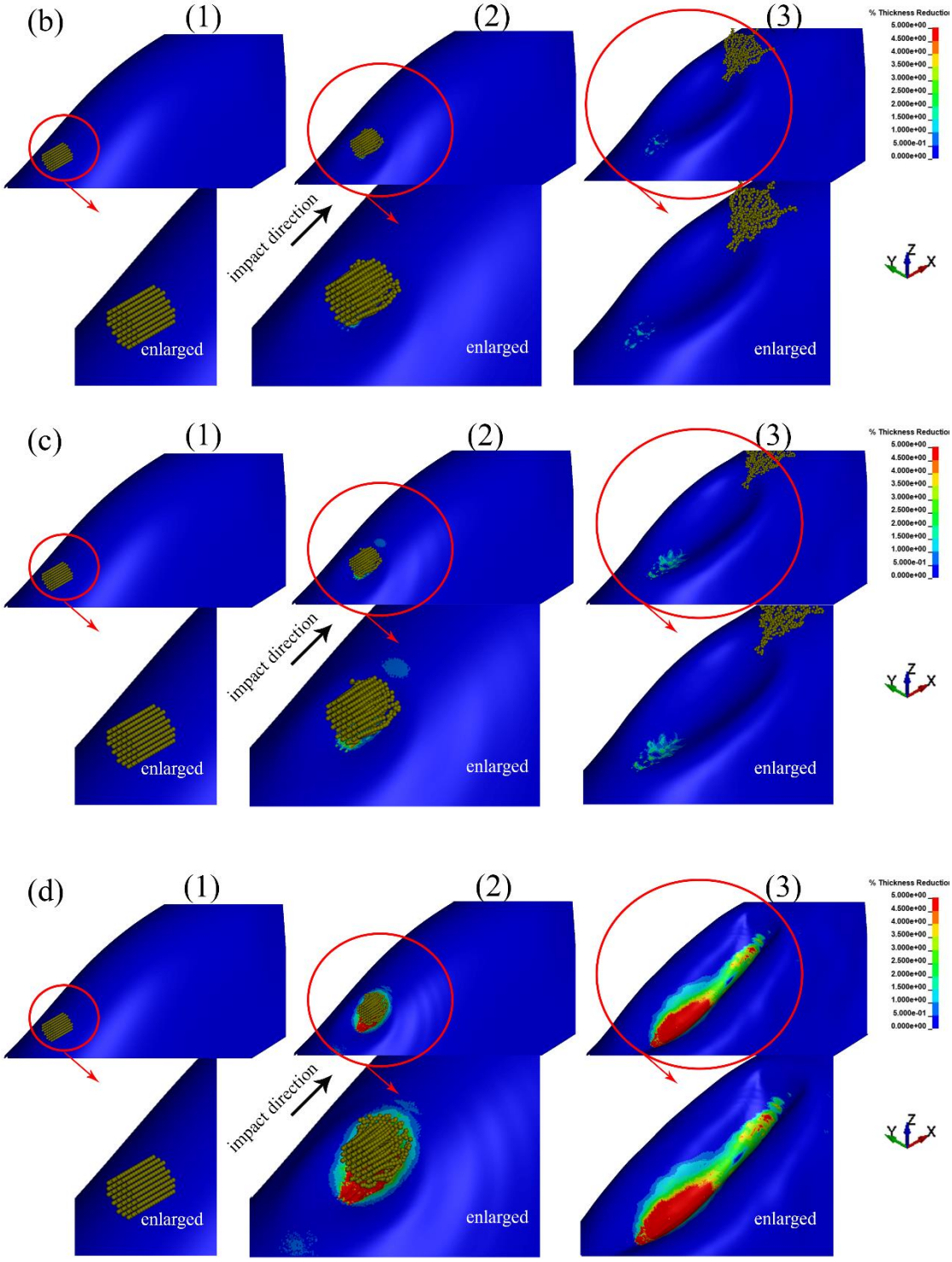

Figure 5.27. (cont.)

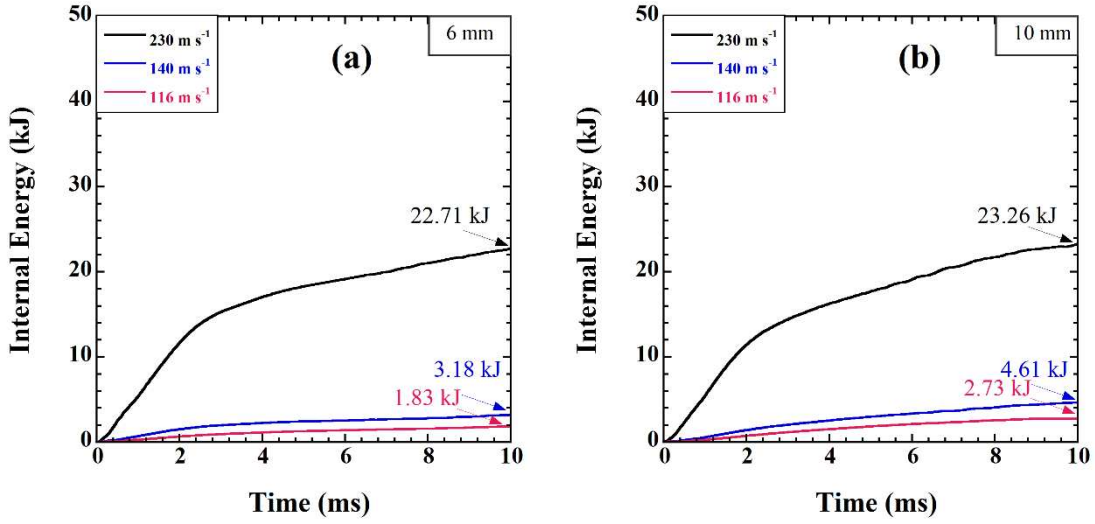

Figure 5.28. The internal energy-time histories of bird strike simulations for (a) 6 and (b) 10 mm- thick PC

CHAPTER 6

CONCLUSIONS

The JC flow stress and damage parameters of a PC were determined experimentally and numerically through quasi-static and high strain tension and compression, quasi-static notched tension, QSI, LVI and PI tests. A modeling approach involving tests and calibrations was implemented for a final aim of obtaining a flow stress equation and damage parameters applicable to the HSR impact events such as bird strike. Five different stress-strain rate relations were investigated in the numerical models. A ductile deformation and fracture behavior of the tested PC were demonstrated for both under tension and compression and the initial peak strength and tensile fracture strain increased at HSRs. The increased HSR fracture strain was ascribed to the adiabatic heating. The tested PC exhibited an asymmetry in tension and compression a notch insensitive fracture strain under increasing tensile stress triaxialities. The flow stress equation determined from the experimental average true stress and the effective stress equation obtained from the numerical tension test resulted in numerical force-displacement curves well-agreed with the experimental QSI force-displacement curves. The experimental and numerical damages of the QSI and LVI test plates were dome-cap formation and dishing, respectively. While the LVI test simulations using flow stress-strain rate relations exhibited force-displacement curves higher than those of the experiments. The detected almost no strain rate sensitivity in the LVI tests were partly ascribed to lower strain rate dependency of the flow stress at intermediate strain rates and relatively high strains. The numerical stress-strain rate relations investigated well-predicted the experimental damage types: dishing at 100 and 140 m s^{-1} and petalling fracture at 160 m s^{-1}, except the CS relation that predicted the fracture of the plate at 140 m s^{-1}. The projectile exit velocities of the used numerical stress-strain rate relations in the PI test at 160 m s^{-1} were shown to be very similar to those of the experiments, except the numerical petal thicknesses were slightly lower than those of the experiments. The absorbed energy at 160 m s^{-1} PI test was determined 1.6 times that of the QSI test, which proved and increased energy absorption capability of the tested PC at the investigated impact velocities. The verified parameters were used to simulate the bird strike to a

canopy with two thicknesses (6 and 10 mm) at low, intermediate and high impact velocities. The bird numerical model parameters were taken from the literature. Besides, these parameters were verified using the Wilbeck's (bird strike on the steel rigid plate) and Welsh and Centonze's (bird strike on the aluminum deformable plate) experiments. The pressure-time history of the bird strike model on the steel rigid plate well matched to the experimental when the Hugoniot- jump pressure was ignored. On the other side, the deflections of the bird strike model on the aluminum deformable plate resulted in higher deflections than that of the Welsh and Centonze experiments. Thereafter, the bird numerical model was implemented into bird strike model on the polycarbonate canopy. The canopy deformation increased with increasing the bird velocity and decreased with increasing the thicknesses of canopy. The percentage reduction of the thicknesses of the 6 and 10 mm- thick canopy was 2.88 and 0.21% at low, 7.94 and 0.56% at intermediate, and 38.35 and 14.93% at high velocities, respectively. The implementation of the bird strike on the canopy numerical model provided the potential damage formed on and the limits of the canopy subjected to bird strike.

REFERENCES

1. Dolbeer, R.; Wright, S.; Weller, J.; Anderson, A.; Beiger, M., *Wildlife strikes to civil aircraft in the United States, 1990-2014*. 2015.

2. Maragakis, I., Bird population trends and their impact on Aviation safety 1999-2008. *European Aviation Safety Agency* **2009**.

3. Mulliken, A. D.; Boyce, M. C., Mechanics of the rate-dependent elastic–plastic deformation of glassy polymers from low to high strain rates. *International Journal of Solids and Structures* **2006,** *43* (5), 1331-1356.

4. Buisson, G.; Ravi-Chandar, K., On the constitutive behaviour of polycarbonate under large deformation. *Polymer* **1990,** *31* (11), 2071-2076.

5. Motta, A.; La Mantia, F. P.; Ascione, L.; Mistretta, M. C., Theoretical study on the decomposition mechanism of bisphenol A polycarbonate induced by the combined effect of humidity and UV irradiation. *Journal of Molecular Graphics and Modelling* **2020,** *99*, 107622.

6. G'sell, C.; Jonas, J., Determination of the plastic behaviour of solid polymers at constant true strain rate. *Journal of materials science* **1979,** *14* (3), 583-591.

7. Boyce, M. C.; Arruda, E. M.; Jayachandran, R., The large strain compression, tension, and simple shear of polycarbonate. *Polymer Engineering & Science* **1994,** *34* (9), 716-725.

8. Boyce, M. C.; Arruda, E. M., An experimental and anaiytical investigation of the large strain compressive and tensile response of glassy polymers. *Polymer Engineering & Science* **1990,** *30* (20), 1288-1298.

9. Smit, R.; van Houten, J., Large Strain Behaviour of Polycarbonate. *EUT, Faculty of Mechanical Engineering Report No. WFW* **1994,** *94*.

10. Eyring, H., Viscosity, Plasticity, and Diffusion as Examples of Absolute Reaction Rates. *The Journal of Chemical Physics* **1936,** *4* (4), 283-291.

11. Ree, T.; Eyring, H., Theory of Non-Newtonian Flow. I. Solid Plastic System. *Journal of Applied Physics* **1955,** *26* (7), 793-800.

12. Bauwens-Crowet, C.; Bauwens, J. C.; Homès, G., Tensile yield-stress behavior of glassy polymers. *Journal of Polymer Science Part A-2: Polymer Physics* **1969,** *7* (4), 735-742.

13. G'Sell, C.; Gopez, A. J., Plastic banding in glassy polycarbonate under plane simple shear. *Journal of Materials Science* **1985,** *20* (10), 3462-3478.

14. Bauwens-Crowet, C.; Ots, J. M.; Bauwens, J. C., The strain-rate and temperature dependence of yield of polycarbonate in tension, tensile creep and impact tests. *Journal of Materials Science* **1974,** *9* (7), 1197-1201.

15. Arruda, E. M.; Boyce, M. C., Evolution of plastic anisotropy in amorphous polymers during finite straining. *International Journal of Plasticity* **1993,** *9* (6), 697-720.

16. Bjerke, T.; Li, Z. H.; Lambros, J., Role of plasticity in heat generation during high rate deformation and fracture of polycarbonate. *International Journal of Plasticity* **2002,** *18* (4), 549-567.

17. Rietsch, F.; Bouette, B., The compression yield behaviour of polycarbonate over a wide range of strain rates and temperatures. *European Polymer Journal* **1990,** *26* (10), 1071-1075.

18. Siviour, C. R.; Walley, S. M.; Proud, W. G.; Field, J. E., The high strain rate compressive behaviour of polycarbonate and polyvinylidene difluoride. *Polymer* **2005,** *46* (26), 12546-12555.

19. Dar, U. A.; Zhang, W. H.; Xu, Y. J.; Wang, J., Thermal and strain rate sensitive compressive behavior of polycarbonate polymer - experimental and constitutive analysis. *Journal of Polymer Research* **2014,** *21* (8).

20. Dar, U. A.; Zhang, W. H., Polymer based aerospace structures under high velocity impact applications; experimental, constitutive and finite element analysis. *J. Mech. Sci. Technol.* **2015,** *29* (10), 4259-4265.

21. Hu, W. J.; Huang, X. C.; Zhang, F. J.; Chen, Y. M., Compression Tests of Polycarbonate under Quasi-static and Dynamic Loading. In *Materials Engineering and Mechanical Automation*, Yang, G., Ed. 2014; Vol. 442, pp 125-128.

22. Zhang, W.; Gao, Y. B.; Ye, N.; Huang, W.; Li, D. C., Experimental Study on Dynamic Mechanical Behaviors of Polycarbonate. In *Shock Compression of Condensed Matter - 2015*, Chau, R.; Germann, T.; Oleynik, I.; Peiris, S.; Ravelo, R.; Sewell, T., Eds. 2017; Vol. 1793.

23. Zhu, S.; Tong, M.; Wang, Y. In *Experiment and Numerical Simulation of a Full-Scale Aircraft Windshield Subjected to Bird Impact*, 50th AIAA/ASME/ASCE/AHS/ASC Structures, Structural Dynamics, and Materials Conference, 2009.

24. Millett, J. C. F.; Bourne, N. K., Shock and release of polycarbonate under one-dimensional strain. *Journal of Materials Science* **2006,** *41* (6), 1683-1690.

25. Sarva, S.; Mulliken, A. D.; Boyce, M. C., Mechanics of Taylor impact testing of polycarbonate. *International Journal of Solids and Structures* **2007,** *44* (7-8), 2381-2400.

26. Trautmann, A.; Siviour, C. R.; Walley, S. M.; Field, J. E., Lubrication of polycarbonate at cryogenic temperatures in the split Hopkinson pressure bar. *International Journal of Impact Engineering* **2005,** *31* (5), 523-544.

27. Sarva, S. S.; Boyce, M. C., Mechanics of polycarbonate during high-rate tension. *Journal of Mechanics of Materials and Structures* **2007,** *2* (10), 1853-1880.

28. Cao, K.; Wang, Y.; Wang, Y., Effects of strain rate and temperature on the tension behavior of polycarbonate. *Materials & Design* **2012,** *38*, 53-58.

29. Cao, K.; Wang, Y.; Wang, Y., Experimental investigation and modeling of the tension behavior of polycarbonate with temperature effects from low to high strain rates. *International Journal of Solids and Structures* **2014,** *51* (13), 2539-2548.

30. Xu, Y. J.; Gao, T. L.; Wang, J.; Zhang, W. H., Experimentation and Modeling of the Tension Behavior of Polycarbonate at High Strain Rates. *Polymers* **2016,** *8* (3).

31. Tzibula, S.; Lovinger, Z.; Rittel, D., Dynamic tension of ductile polymers: Experimentation and modelling. *Mechanics of Materials* **2018,** *123*, 30-42.

32. Fleck, N. A.; Stronge, W. J.; Liu, J. H., HIGH STRAIN-RATE SHEAR RESPONSE OF POLYCARBONATE AND POLYMETHYL METHACRYLATE. *Proceedings of the Royal Society of London Series a-Mathematical and Physical Sciences* **1990,** *429* (1877), 459-+.

33. Wright, S. C.; Fleck, N. A.; Stronge, W. J., Ballistic impact of polycarbonate—An experimental investigation. *International Journal of Impact Engineering* **1993,** *13* (1), 1-20.

34. Rosenberg, Z.; Kositski, R., Deep indentation and terminal ballistics of polycarbonate. *International Journal of Impact Engineering* **2017,** *103*, 225-230.

35. Sadeghi Esfahlani, S., Ballistic performance of Polycarbonate and Polymethyl methacrylate under normal and inclined dynamic impacts. *Heliyon* **2021,** *7* (4), e06856.

36. Wang, J.; Xu, Y. J.; Gao, T. L.; Zhang, W. H.; Moumni, Z., A 3D thermomechanical constitutive model for polycarbonate and its application in ballistic simulation. *Polymer Engineering and Science* **2018,** *58* (12), 2237-2248.

37. Husain, A.; Ansari, R.; Khan, A. H., Experimental and Numerical Investigation of Perforation of Thin Polycarbonate Plate by Projectiles of Different Nose Shape. *Latin American Journal of Solids and Structures* **2017,** *14*, 357-372.

38. Robertson, R. E., Theory for the Plasticity of Glassy Polymers. *The Journal of Chemical Physics* **1966,** *44* (10), 3950-3956.

39. Haward, R. N.; Thackray, G.; Sugden, T. M., The use of a mathematical model to describe isothermal stress-strain curves in glassy thermoplastics. *Proceedings of the Royal Society of London. Series A. Mathematical and Physical Sciences* **1968,** *302* (1471), 453-472.

40. Argon, A. S., A theory for the low-temperature plastic deformation of glassy polymers. *The Philosophical Magazine: A Journal of Theoretical Experimental and Applied Physics* **1973,** *28* (4), 839-865.

41. Boyce, M. C.; Parks, D. M.; Argon, A. S., Large inelastic deformation of glassy polymers. part I: rate dependent constitutive model. *Mechanics of Materials* **1988,** *7* (1), 15-33.

42. Richeton, J.; Ahzi, S.; Daridon, L.; Rémond, Y., A formulation of the cooperative model for the yield stress of amorphous polymers for a wide range of strain rates and temperatures. *Polymer* **2005,** *46* (16), 6035-6043.

43. Fotheringham, D.; Cherry, B. W.; Bauwens-Crowet, C., Comment on "the compression yield behaviour of polymethyl methacrylate over a wide range of temperatures and strain-rates". *Journal of Materials Science* **1976,** *11* (7), 1368-1371.

44. Richeton, J.; Ahzi, S.; Vecchio, K. S.; Jiang, F. C.; Adharapurapu, R. R., Influence of temperature and strain rate on the mechanical behavior of three amorphous polymers: Characterization and modeling of the compressive yield stress. *International Journal of Solids and Structures* **2006,** *43* (7), 2318-2335.

45. Varghese, A. G.; Batra, R. C., Constitutive equations for thermomechanical deformations of glassy polymers. *International Journal of Solids and Structures* **2009,** *46* (22), 4079-4094.

46. Safari, K. H.; Zamani, J.; Ferreira, F. J.; Guedes, R. M., Constitutive modeling of polycarbonate during high strain rate deformation. *Polymer Engineering and Science* **2013,** *53* (4), 752-761.

47. Al-Juaid, A. A.; Othman, R., Modeling of the Strain Rate Dependency of Polycarbonate's Yield Stress: Evaluation of Four Constitutive Equations. *Journal of Engineering* **2016**.

48. Wang, J.; Xu, Y.; Zhang, W.; Moumni, Z., A damage-based elastic-viscoplastic constitutive model for amorphous glassy polycarbonate polymers. *Materials & Design* **2016,** *97*, 519-531.

49. Wang, F. S.; Yue, Z. F., Numerical simulation of damage and failure in aircraft windshield structure against bird strike. *Materials & Design* **2010,** *31* (2), 687-695.

50. Siddens, A. J.; Bayandor, J.; Abdi, F., Soft Impact Damage Prognosis of F-16 Canopy Using Progressive Failure Dynamic Analysis. *Journal of Aircraft* **2014,** *51* (6), 1959-1965.

51. Yu, P.; Yao, X. H.; Han, Q., The dynamic response and failure of Polycarbonate plate by soft body impact. *Polymer Engineering and Science* **2016,** *56* (10), 1160-1168.

52. Ramakrishnan, K. R. Low velocity impact behaviour of unreinforced bi-layer plastic laminates. UNSW Sydney, 2009.

53. Shah, Q. H.; Abakr, Y. A., Effect of distance from the support on the penetration mechanism of clamped circular polycarbonate armor plates. *International Journal of Impact Engineering* **2008,** *35* (11), 1244-1250.

54. Shah, Q. H., Impact resistance of a rectangular polycarbonate armor plate subjected to single and multiple impacts. *International Journal of Impact Engineering* **2009,** *36* (9), 1128-1135.

55. Meng, X.; Sun, Y.; Yu, J.; Tang, Z.; Liu, J.; Suo, T.; Li, Y., Dynamic response of the horizontal stabilizer during UAS airborne collision. *International Journal of Impact Engineering* **2019,** *126*, 50-61.

56. Antoine, G. O.; Batra, R. C., Low Velocity Impact of Flat and Doubly Curved Polycarbonate Panels. *Journal of Applied Mechanics* **2015,** *82* (4).

57. Antoine, G. O.; Batra, R. C., Effect of Curvature on Penetration Resistance of Polycarbonate Panels. *Journal of Applied Mechanics* **2016,** *83* (12).

58. Duan, Y.; Saigal, A.; Greif, R.; Zimmerman, M. A., A uniform phenomenological constitutive model for glassy and semicrystalline polymers. *Polymer Engineering & Science* **2001,** *41* (8), 1322-1328.

59. Johnson, G.; Cook, W. H. In *A CONSTITUTIVE MODEL AND DATA FOR METALS SUBJECTED TO LARGE STRAINS, HIGH STRAIN RATES AND HIGH TEMPERATURES*, 1983.

60. Matsuoka, S., *Relaxation phenomena in polymers*. Hanser Munich: 1992.

61. Brooks, N. W. J.; Duckett, R. A.; Ward, I. M., Modeling of double yield points in polyethylene: Temperature and strain-rate dependence. *Journal of Rheology* **1995,** *39* (2), 425-436.

62. Wang, J.; Xu, Y.; Zhang, W., Finite element simulation of PMMA aircraft windshield against bird strike by using a rate and temperature dependent nonlinear viscoelastic constitutive model. *Composite Structures* **2014,** *108*, 21-30.

63. Dorogoy, A.; Rittel, D., Effect of confinement on thick polycarbonate plates impacted by long and AP projectiles. *International Journal of Impact Engineering* **2015,** *76*, 38-48.

64. Wang, T. J.; Kishimoto, K.; Notomi, M., A micromechanics criterion for the ductile fracture of a polycarbonate. In *Fracture and Strength of Solids, Pts 1 and 2*, Hwang, W.; Han, K. S., Eds. Trans Tech Publications Ltd: Stafa-Zurich, 2000; Vol. 183-1, pp 121-126.

65. Castagnet, S.; Deburck, Y., Relative influence of microstructure and macroscopic triaxiality on cavitation damage in a semi-crystalline polymer. *Materials Science and Engineering a-Structural Materials Properties Microstructure and Processing* **2007,** *448* (1-2), 56-66.

66. Manaia, J. P.; Pires, F. A.; de Jesus, A. M. P.; Wu, S. H., Mechanical response of three semi crystalline polymers under different stress states: Experimental investigation and modelling. *Polymer Testing* **2020,** *81*.

67. Bridgman, P. W., *Studies in Large Plastic Flow and Fracture : With Special Emphasis on the Effects of Hydrostatic Pressure*. Harvard University Press: Cambridge, MA, USA,, 1964.

68. Dwivedi, A.; Bradley, J.; Casem, D. *Mechanical response of polycarbonate with strength model fits*; DYNAMIC SCIENCE INC ABERDEEN MD: 2012.

69. Xu, Y.; Lu, H.; Gao, T.; Zhang, W., Predicting the low-velocity impact behavior of polycarbonate: Influence of thermal history during injection molding. *International Journal of Impact Engineering* **2015,** *86*, 265-273.

70. Dar, U. A.; Awais, M.; Mian, H. H.; Sheikh, M. Z., The effect of representative bird model and its impact direction on crashworthiness of aircraft windshield and canopy structure. *Proceedings of the Institution of Mechanical Engineers Part G-Journal of Aerospace Engineering* **2019,** *233* (14), 5150-5163.

71. Kim, H.; Kedward, K. T., Modeling Hail Ice Impacts and Predicting Impact Damage Initiation in Composite Structures. *AIAA Journal* **2000,** *38* (7), 1278-1288.

72. Abrate, S., Soft impacts on aerospace structures. *Progress in Aerospace Sciences* **2016,** *81*, 1-17.

73. Wilbeck, J. S. *Impact behavior of low strength projectiles*; July 01, 1978, 1978.

74. Lavoie, M. A.; Gakwaya, A.; Ensan, M. N.; Zimcik, D. G.; Nandlall, D., Bird's substitute tests results and evaluation of available numerical methods. *International Journal of Impact Engineering* **2009,** *36* (10), 1276-1287.

75. Shupikov, A.; Ugrimov, S.; Smetankina, N.; Yareshchenko, V.; Onhirsky, G.; Ukolov, V.; Samoylenko, V.; Avramenko, V., Bird Dummy for Investigating the Bird-Strike Resistance of Aircraft Components. *Journal of Aircraft* **2013,** *Vol. 50*, pp. 817-826.

76. Ćwiklak, J.; Kobiałka, E.; Goś, A., Experimental and Numerical Investigations of Bird Models for Bird Strike Analysis. *Energies* **2022,** *15* (10), 3699.

77. Welsh, C. J.; Centonze, V. In *Aircraft Transparency Testing - Artificial Birds*, 1986.

78. Heimbs, S., Computational methods for bird strike simulations: A review. *Computers & Structures* **2011,** *89*, 2093-2112.

79. Airoldi, A.; Cacchione, B., Modelling of impact forces and pressures in Lagrangian bird strike analyses. *International Journal of Impact Engineering* **2006,** *32* (10), 1651-1677.

80. Liu, J.; Li, Y. L.; Xu, F., The Numerical Simulation of a Bird-Impact on an Aircraft Windshield by Using the SPH Method. *Advanced Materials Research* **2008,** *33-37*, 851-856.

81. Grimaldi, A.; Sollo, A.; Guida, M.; Marulo, F., Parametric study of a SPH high velocity impact analysis – A birdstrike windshield application. *Composite Structures* **2013,** *96*, 616-630.

82. Plassard, F.; Hereil, P.; Joseph, P.; Mespoulet, J., *Experimental and numerical study of a bird strike against a windshield*. 2015; Vol. 94, p 01051.

83. Johnson, G. R.; Cook, W. H., Fracture characteristics of three metals subjected to various strains, strain rates, temperatures and pressures. *Engineering fracture mechanics* **1985,** *21* (1), 31-48.

84. Huh, H.; Kang, W., Crash-worthiness assessment of thin-walled structures with the high-strength steel sheet. *International Journal of Vehicle Design* **2002,** *30*, 1-21.

85. Allen, D. J.; Rule, W. K.; Jones, S. E., Optimizing material strength constants numerically extracted from taylor impact data. *Experimental Mechanics* **1997,** *37* (3), 333-338.

86. Cowper, G. R.; Symonds, P. S. In *STRAIN-HARDENING AND STRAIN-RATE EFFECTS IN THE IMPACT LOADING OF CANTILEVER BEAMS*, 1957.

87. Hallquist, J. O., and LS-DYNA Keyword User's. Manual, *Livermore Software Technology Corporation R11: Livermore*. 2021.

88. International, A., ASTM D638-14 Standard Test Method for Tensile Properties of Plastics. ASTM International: 2014.

89. International, A., ASTM E8/E8M-13a: Standard Test Methods for Tension Testing of Metallic Materials. ASTM International: 2013.

90. Blaber, J.; Adair, B.; Antoniou, A., Ncorr: Open-Source 2D Digital Image Correlation Matlab Software. *Experimental Mechanics* **2015,** *55* (6), 1105-1122.

91. Çakırcalı, M.; Kılıçaslan, C.; Güden, M.; Kıranlı, E.; Shchukin, V. Y.; Petronko, V. V., Cross wedge rolling of a Ti6Al4V (ELI) alloy: the experimental studies and the finite element simulation of the deformation and failure. *The International Journal of Advanced Manufacturing Technology* **2013,** *65* (9), 1273-1287.

92. Güden, M.; Enser, S.; Bayhan, M.; Taşdemirci, A.; Yavaş, H., The strain rate sensitive flow stresses and constitutive equations of a selective-laser-melt and an annealed-rolled 316L stainless steel: A comparative study. *Materials Science and Engineering: A* **2022,** *838*, 142743.

93. International, A., ASTM D6264/D6264M-04 Test Method for Measuring the Damage Resistance of a Fiber-reinforced Polymer-matrix Composite to a Concentrated Quasi-static Indentation Force. ASTM International: 2004.

94. International, A., ASTM D7136/D7136M-12 Standard test method for measuring the damage resistance of a fiber-reinforced polymer matrix composite to a drop-weight impact event. ASTM International: 2012.

95. Zhang, W.; Xu, Y., 1 - Experimental Studies of Mechanical Properties of Polycarbonate. In *Mechanical Properties of Polycarbonate*, Zhang, W.; Xu, Y., Eds. Elsevier: 2019; pp 1-28.

96. Dorogoy, A.; Rittel, D.; Brill, A., Experimentation and modeling of inclined ballistic impact in thick polycarbonate plates. *International Journal of Impact Engineering* **2011,** *38* (10), 804-814.

97. Hellier, A.; Chaphalkar, P.; Prusty, G., *Fracture Toughness Measurement for Aluminium 6061-T6 using Notched Round Bars*. 2017.

98. Prakash, V.; Mehta, N., Uniaxial compression and combined compression-and-shear response of amorphous polycarbonate at high loading rates. *Polymer Engineering and Science* **2012,** *52* (6), 1217-1231.

99. Boyer, R. F., Dependence of mechanical properties on molecular motion in polymers. *Polymer Engineering & Science* **1968,** *8* (3), 161-185.

100. Hedayati, R.; Ziaei-Rad, S., New Bird Model for Simulation of Bird Strike on Various Layups Used in Transparent Components of Rotorcrafts. *Journal of Aerospace Engineering* **2014,** *27* (1), 76-85.

101. Leski, A.; Baraniecki, R.; Malachowski, J., Numerical simulation to study the influence of the thickness of canopy at a bird strike. In *DESIGN 2002: Proceedings of the 7th International Design Conference, Vols 1 and 2*, 2002; pp 667-672.

VITA

Education

- Ph.D., 2023, Mechanical Engineering, Izmir Institute of Technology
- M.Sc., 2017, Mechanical Engineering, Izmir Institute of Technology
- B.Sc., 2014, Mechanical Engineering, Izmir Institute of Technology

Publications

- Mauko, A.; Sarıkaya, M.; Güden, M.; Duarte, I.; Borovinšek, M.; Vesenjak, M.; Ren, Z., High strain-rate deformation analysis of open-cell aluminium foam. Journal of Materials Research and Technology 2023, 25, 1208-1221.doi: 10.1016/j.jmrt.2023.05.280

- Çelik, M.; Güden, M.; Sarıkaya, M.; Taşdemirci, A.; Genç, C.; Ersoy, K.; Serin, Ö., The impact response of a Nomex® honeycomb core/E-glass/epoxy composite sandwich structure to increasing velocities: Experimental and numerical analysis. Composite Structures 2023, 320, 117205.doi: 10.1016/j.compstruct.2023.117205

- Sarıkaya, M.; Güden, M.; Kambur, Ç.; Özbek, S. Ç.; Taşdemirci, A., Development of the Johnson-Cook flow stress and damage parameters for the impact response of polycarbonate: Experimental and numerical approach. International Journal of Impact Engineering 2023, 179, 104674.doi: 10.1016/j.ijimpeng.2023.104674

- Tuncer, C., Güden, M., Orhan, M., Sarıkaya, M. K., & Taşdemirci, A. (2023). Quasi-static and dynamic Brazilian testing and failure analysis of a deer antler in the transverse to the osteon growth direction. Journal of the Mechanical Behavior of Biomedical Materials, 138, 105648. doi:10.1016/j.jmbbm.2023.105648

- Shi, C., Guo, B., Sarıkaya, M., Çelik, M., Chen, P., Güden, M. (2021). Determination of the material model and damage parameters of a carbon fiber reinforced laminated epoxy composite for high strain rate planar compression. International Journal of Impact Engineering 149, 103771. doi:10.1016/j.ijimpeng.2020.103771

- Sarıkaya, M., Taşdemirci, A., & Güden, M. (2019). Impact loading and modelling a multilayer aluminium corrugated/fin core: The effect of the insertion of imperfect fin layers. Strain, 55(1), e12298. doi:10.1111/str.12298

- Sarıkaya, M., Taşdemirci, A., & Güden, M. (2018). Dynamic crushing behavior of a multilayer thin-walled aluminum corrugated core: The effect of velocity and imperfection. Thin-Walled Structures, 132, 332-349. doi:10.1016/j.tws.2018.06.029